FLORIDA INTERNATIONAL UNIVERSITY

Miami, Florida

ALLOSTERIC MECHANISM ON DREAM DIMERIZATION AND IMPACT ON ITS INTERACTIONS WITH DIVALENT METAL ZINC

A dissertation submitted in partial fulfillment of the
requirements for the degree of
DOCTOR OF PHILOSOPHY
in
CHEMISTRY
by
Maria D. Santiago Estevez

2022

To: Dean Michael R. Heithaus
College of Arts, Sciences and Education

This dissertation, written by Maria D. Santiago Estevez, and entitled Allosteric Mechanism on DREAM Dimerization and Impact on Its Interactions with Divalent Metal Zinc, having been approved in respect to style and intellectual content, is referred to you for judgment.

We have read this dissertation and recommend that it be approved.

Prem Chapagain

Fenfei Leng

Xiaotang Wang

Francisco Fernandez Lima

Jaroslava Miksovska, Major Professor

Date of Defense: June 29, 2022

The dissertation of Maria D. Santiago Estevez is approved.

Dean Michael R. Heithaus
College of Arts, Sciences and Education

Andrés G. Gil
Vice President for Research and Economic Development
and Dean of the University Graduate School

Florida International University, 2022

DEDICATION

To the memory of my grandparents Isabel Navarro , Marcelino Estevez, Lazara Valdes and Salustiano Santiago, who sacrificed so much and paved the way that led me to this moment.

To my parents Felicia Estevez and Joel Santiago who sacrificed their passion for medicine to give us a better future . To my beautiful mother who has given me all the love ,support and encouragement to keep going.

To the most amazing sisters Maria Jose Santiago and Maria Daniel Santiago, my greatest gift from God.

ACKNOWLEDGMENTS

I want to thank the Lord Jesus Christ for all His blessings ;He has led me to where I am today and only by His grace, I live every day. “It was not I , but the grace of God that is with me “ 1 Corinthians 15:10. He has placed the most amazing people in my life , I will always be grateful for their love, support and their contribution to my everyday improvement .

I would like to thank my advisor Dr. Jaroslava Miksovska, this work is only possible because of her kindness and commitment to her job , and her willingness to fight for students when no one else would . She took a chance by giving me an opportunity I did not deserve , she helped me and fought for me without knowing me and her resilience and determination is what gave me the possibility to start graduate school. I will always be grateful for everything she has done for me and what I have learned by her side. It has been a privilege to spend this time with such an exceptional human being who leads by example, and every present and future goal I am able to accomplish will be due to her.

I would also like to acknowledge my committee members Dr. Xiaotang Wang , Dr.Francisco Fernandez-Lima, Dr. Fenfei Leng and Dr. Prem Chapagain. Their kindness, patience and the time they dedicated providing their input has been essential for the completion of this work. I will always be grateful for their continuous help and support.

I am indebted with Ms. Maggie Autie , who has provided a tremendous amount of help and support in every step of this process ,her door has always been open for me and many others. She has been sent by God to not only help but also to encourage , to support and most importantly to provide hope in knowing a better future is ahead.

I am forever grateful to Dr. Sonja Montas –Hunter, Dr. Alla Mirzoyan and Ms. Christine Dome. Their kindness and willingness to help are unmatched, their support throughout the years has been uplifting; and their humbleness , work ethics and empathy towards others has given me hope and encouragement making me feel heard and appreciated.

To the people that uplifted me every day and provided a helping hand and a warm smile, I cannot thank them enough for being there. Klara Utria and Maria Isabel Frias from FIU staff , Angelita and Lucila from Bustelo.

I also want to thank my lab partners and forever friends; we have shared beautiful and difficult moments together and they will always have a place in my heart. Dr. Antonija Tangar, Dr. Ruipeng Lei, Dr. Samiol Azam, Dr. Setareh Sakhdari, Dr. Linjia Su, Rifat Farhana , Jonathan Cedeno and Shofiul Alam .I am also thankful to Andres Arango; to the amazing undergraduate students who helped me so much and shared their time and effort, I am thrilled to have worked with such beautiful young people . Brian Gomez , Gessica St. Louis, Tetyana Shvets , Adriana Riveron, Sasha Rodriguez, Enzo Leon, Daylen Camacho , Heidi Alonso , Maria Romero , Valentin Mujica , Antonio Gutierrez , Veronica Rodriguez , Manuel Picon , Isa Sabir, Bryan Jimenez and Christian Hernandez.

I want to thank my dear friends over the years that have become family and have given friendship a true meaning , they have made me a happier person and I am forever grateful for their support . Dr. Haydee Linares Rosales, Carolina Pastorelli , Joel Adams , Tumpa Dasgupta, Dr. Rajib Kumar , Israel Castillo, Dr. Zeynep Eren and Joana Almeida.

I will always be indebted to my mother Felicia Estevez; she is the reason I do everything in life . She has taught me to put God first , her acts of love and sacrifice for others , her humbleness and resilience and her forgiving nature are the most valuable lessons .The tremendous amount of support I have received from her, and her encouragement have been the main force for me to complete this work . I am thankful to my father Joel Santiago for the books he bought for me when I was a child and for his encouragement to get a higher education.

To my sisters Maria Jose Santiago and Maria Daniel Santiago who have been the source of my happiness since I can remember, they are my biggest blessing and the certainty I will never walk alone through life . I would have never been able to even start this work without their infinite help and support. To my aunts Lilia Estevez and Nanci Estevez for all their love and help during my entire life, they are a huge blessing.

I am forever grateful to the American people and the core values of the United States of America of life, liberty and the pursuit of happiness; for giving me all the opportunities I was denied in my native country.

Lastly, I am grateful to the Bridge to the Doctorate Fellowship who provided me with financial support to start graduate school and for the doors they opened for me. I am also extremely grateful to the McKnight Fellowship who not only provided financial support, but also made me maintain my faith in the possibility of institutions being run by good people that value others and consider their struggles, thank you Dr. Lawrence Morehouse, Mr. Charles Jackson and Ms Phillys Reddick for making me part of the McKnight family.

ABSTRACT OF THE DISSERTATION

ALLOSTERIC MECHANISM ON DREAM DIMERIZATION AND IMPACT ON ITS INTERACTIONS WITH DIVALENT METAL ZINC

by
Maria D. Santiago Estevez
Florida International University ,2022
Miami, Florida
Professor Jaroslava Miksovska, Major Professor

DREAM belongs to the NCS family, and it is involved in several physiological processes mediated by Ca^{2+} association, which produces changes in its oligomerization state. The mechanism of how Ca^{2+} binds to DREAM remains unknown. A kinetic study of the binding of Ca^{2+} to DREAM suggested that DREAM dimerization is a two-step process, the first step(τ_1= 8±0.1ms) is associated with the binding of Ca^{2+} to the monomer, while the second step (τ_2 = 3.6 ±0.4 s) corresponds to a conformation relaxation that leads to the dimerization. Furthermore, by analyzing the fast kinetic k_{obs}vs[L] , an inverse hyperbolic dependance was observed , which corresponds to the conformational selection mechanism providing crucial information on the binding of Ca^{2+} to DREAM.

Previous MD studies has shown that a network of hydrophobic residues in DREAM participate in the transmission of the interdomain allosteric signal. The Trp169 is part of this network, MD analysis were performed to determine its role in allosteric signal transmission. The mutation of Trp to Ala lead to a loss of structural rearrangement previously observed upon Ca^{2+} binding. For instance, in the case of DREAMW169A the stabilizing salt bridge K87-E165 was not present , the EF hands in the mutant did not

undergo the reorientation observed in DREAMWT and the dimer divided into two monomers in the presence of Ca^{2+}. These findings suggest the Trp169 is involved in the interdomain communication in DREAM, and it is crucial for the protein proper functioning.

Zn^{2+} is involved in several physiological processes and interacts with a wide variety of proteins , including other NCS proteins. DREAM also interacts with divalent metals with relatively high affinity . The presence of Zn^{2+} produces changes in DREM's tertiary structure , and it is able to bind to DREAM in the presence(K_d=10.76± 1.46 and μM) and absence of Ca^{2+} (K_d=6.9 ± 0.6 μM). For the MD studies in the presence and absence of Ca^{2+}, Zn^{2+} was found to bind to the protein involving amino acids located in EFH2. These findings suggest that Zn^{2+} may be involved in processes possibly involving DREAM and other NCS.

TABLE OF CONTENTS

CHAPTER PAGE

LIST OF TABLES

TABLE PAGE

LIST OF FIGURES

FIGURE PAGE

LIST OF ABREVIATIONS

ABBREVIATION	FULL NAME
1,8-ANS	1-anilinonaphthalene-8-sulfonic acid
aMD	accelerated Molecular Dynamics
Ca^{2+}	Calcium
CaM	calmodulin
CD	Circular dichroism
DREAM	Downstream regulatory element antagonist modulator
EDTA	2-({2-[Bis(carboxymethyl)amino]ethyl}(carboxymethyl)amino)acetic acid
EFX	EF-hand X
EGTA	ethyleneglycol-bis(2-aminoethylether)-N,N,N′,N′-tetraacetic
GaMD	Gaussian accelerated Molecular Dynamics
IPTG	Isopropyl β-D-1-thiogalactopyranoside
KChIP	Potassium channel interaction protein
Kd	Dissociation constant
MD	Molecular Dynamics
Mg^{2+}	Magnesium
NCS	Neuronal Calcium Sensor
RMSD	Root mean square deviation
RMSF	Root mean square fluctuations
TRIS	2-Amino-2-hydroxymethyl-propane-1,3-diol

λ_{max}	Emission maxima

1. INTRODUCTION

1.1 Storage and signaling of Ca^{2+} in the organism.

Calcium is one of the essential elements required by living organism. It is found in the mineralized tissue such as bone and teeth in form of calcium carbonate or calcium phosphate, respectively. On the cellular level, calcium ions (Ca^{2+}) together with magnesium ions (Mg^{2+}) also serve as metal activators in protein (Wang et al., 2019). Calcium is mainly an intracellular ion that is involved in various physiological processes in almost all eukaryotic organisms and its concentration is strictly regulated to carry out its numerous biological functions. In general, the resting concentration of Ca^{2+} in the cytoplasm is maintained two to three orders of magnitude lower than in the extracellular space and it is approximately 10^{-8} M (Permyakov, E. A. & Kretsinger, 2011; Wang et al., 2019). The Ca^{2+} homeostasis in the intracellular space is maintained by two main mechanisms: Ca^{2+} binding to Ca^{2+} handling proteins, often called calcium buffers, and a reticular network consisting of several components including the endoplasmic reticulum (sarcoplasmic reticulum in muscles), the golgi apparatus, and components of the endocytic pathway (Wang et al., 2019)

The most important component of the reticular network and the largest reservoir of intracellular Ca^{2+} is found in the endoplasmic reticulum (ER). In the ER, Ca^{2+} is released through the activation of the inositol 1,4,5-trisphosphate receptor and ryanodine receptor 3, the latter occurring in a Ca^{2+} induced- Ca^{2+} release mechanism (Lock et al., 2019), Ca^{2+} can also be released by the action of other second messengers such as cyclic adenosine monophosphate and nicotinic acid adenine dinucleotide phosphate (Groenendyk et al., 2021)

The level of intracellular Ca^{2+}can be lowered via two mechanisms: either returning it to the ER, which occurs through the Ca^{2+} pump SERCA in the ER membrane or by excretion through Na^+/ Ca^{2+}pumps to the extracellular compartment (Groenendyk et al., 2021) There are several proteins that are involved in the handling and buffering of Ca^{2+}. Calreticulin, an ER luminal chaperone, which is important in maintaining 50% of the total calcium in the ER, while the chaperone BiP/GRP78 binds 25% of the total calcium stores (Wang et al., 2019) Other proteins involved in this process include the disulfide isomerase (PIDs) family and the glucose related protein (GRP94) (Wang et al., 2019) In the sarcoplasmic reticulum, the protein calsequestrin is also important in calcium binding and contains 2 isoforms: CASQ1 in skeletal muscle and CASQ2 in cardiac muscle (Wang et al., 2019)

In excitable cells, such as neurons, Ca^{2+} concentration is regulated by voltage gated Ca^{2+} channels which are closed during the resting state but open upon neuronal depolarization (Ramirez et al., 2017) . The influx of Ca^{2+} into the presynaptic terminal allows for the fusion of synaptic vessels into the membrane and the release of neurotransmitters into the synaptic cleft, thereby playing a critical role in the transduction of neuronal impulses. (Ramirez et al., 2017)

1.2 Biological processes that involve Ca^{2+}

Since the function and conformational state of many proteins can be altered by Ca^{2+}binding, this ion is extremely important in various physiological processes. Previous studies have recognized the importance of calcium in processes associated with gene transcription, cell signaling,inmune response ,fertilization , control of cell cycle , muscle contraction and motility (Sukumaran et al., 2021).

In the neuronal tissue, Ca^{2+} is essential for normal brain function and participate in neurotransmitter release, synaptic plasticity, and axonal regeneration (Padamsey et al., 2019). Furthermore, neuronal calcium sensor proteins have been implicated in several neuropathologies such as schizophrenia, Alzheimer disease, X-linked mental retardation, and fragile X syndrome, underlying the importance of neuronal Ca^{2+} homeostasis (Bandura & Feng, 2019)

1.3 Calcium Binding Proteins and motifs

Calcium binding proteins are divided in two main groups Ca^{2+} buffers and Ca^{2+}sensors . The Ca^{2+} buffers such as parvalbumin do not undergoe large structural changes upon Ca^{2+} binding (Figure 1.1) and their function is to keep the concentration of Ca^{2+} within the cell under resting conditions .

On the other hand, the group comprising Ca^{2+} sensor proteins undergoes conformational changes upon Ca^{2+} binding that regulate their affinity to other effector proteins. For instance, in the case of calmodulin, the binding of Ca^{2+} rearranges the alfa helices in individual EF-hands from the close to open configuration. This initial reorientation of EF-hands leads to a larger structural change, exposure of the central linker and hydrophobic sidechains of methionine, resulting in increased affinity for effector proteins such as myosin kinase and protein kinase II (Lewit-Bentley & Réty, 2000) (Figure 1.2).

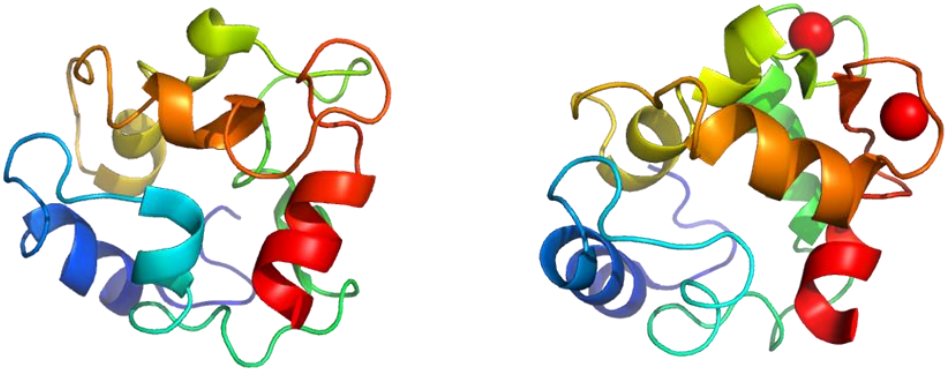

Figure 1.1: Structure of apoparvalbumin, PDB ID 2KYC (left panel) and Ca^{2+} bound parvalbumin, PDB ID 2KYF (right panel) showing low structural rearrangement upon Ca^{2+} binding.

Intracellular Ca^{2+} ions associate to various soluble proteins or membrane channels. There are three motifs to which Ca^{2+} associates to CBPs: EF-hands, C2-domain and βγ-crystallin motifs. (Srivastava et al., 2014)

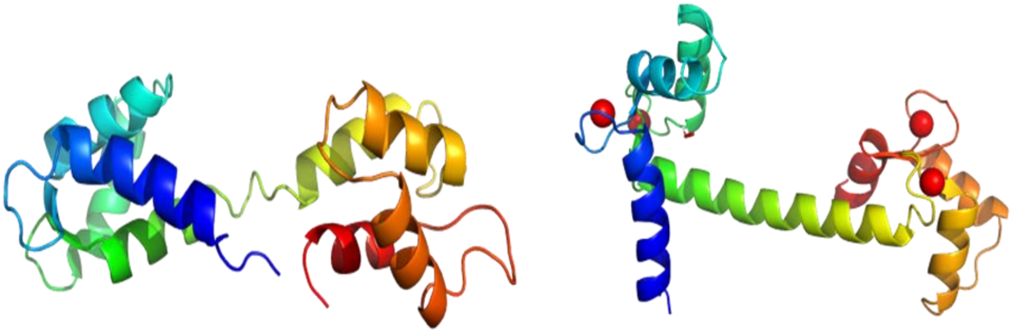

Figure 1.2: Structure of apo calmodulin, PDB ID 1CFD(left panel) and Ca^{2+} bound calmodulin, PDB ID 1CLL (right panel) showing the Ca^{2+} induced conformational changes.

Most calcium-binding proteins (CBPs) contain EF-hands. This term was coined more than 50 years ago by Kretsinger and Nockolds as they attempted to describe the conformational shape of the CBP parvalbumin (Lewit-Bentley & Réty, 2000). The EF-hand Ca^{2+} binding motif was named after the E and F alpha-helices of the parvalbumin structure that adopt a structural form resembling the thumb and index finger of a hand. The EF-hand of most CBPs contains a helix-loop-helix structural motif shown in Figure 1.3 (Gifford et al., 2007). Depending on the amino acid sequence, some EF-hands can bind Mg^{2+} or Ca^{2+} whereas other EF-hands are Ca^{2+} selective. Mg^{2+} tends to adopt octahedral coordination geometry whereas Ca^{2+} ions prefer pentagonal bipyramidal geometry as visualized in Figure 1.3. (Tang & Yang,)

The canonical Ca^{2+} binding loop is composed of 9 residues and provides five ligands for Ca^{2+} coordination and two other ligands are provided by the side chain of a glutamic acid residue that serves as a bidental ligand (Figure 1.3.) (Gifford et al., 2007).

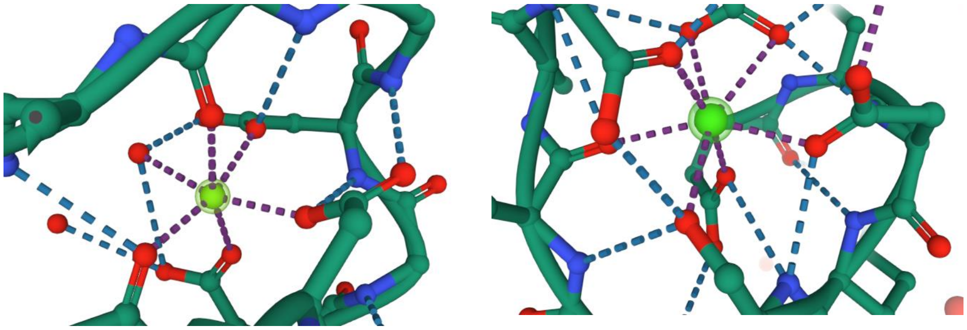

Figure 1.3: EF-hand 2 of parvalbumin bound to Mg^{2+} (shown as a green sphere) in an octahedral configuration interacting with six oxygen atoms (left panel). EF-hand 1 of parvalbumin bound to Ca^{2+} (shown in green) in a pentagonal bipyramidal geometry. Note the bidental coordination of Ca^{2+} by Glu sidechain (right panel). PDB entry 4PAL.

Furthermore, in some EF hands a water molecule forms a hydrogen bond with one of the side chains in the loop and completes the Ca^{2+} coordination sphere. It is worth mentioning that most of the amino acids in the loop are negatively charged such as aspartic and glutamic acids which is consistent with the preference of calcium and other alkaline earth metals for amino acids with carboxylic acid side chains as shown on Table 1.1 (Gifford et al., 2007) (Figure 1.4).

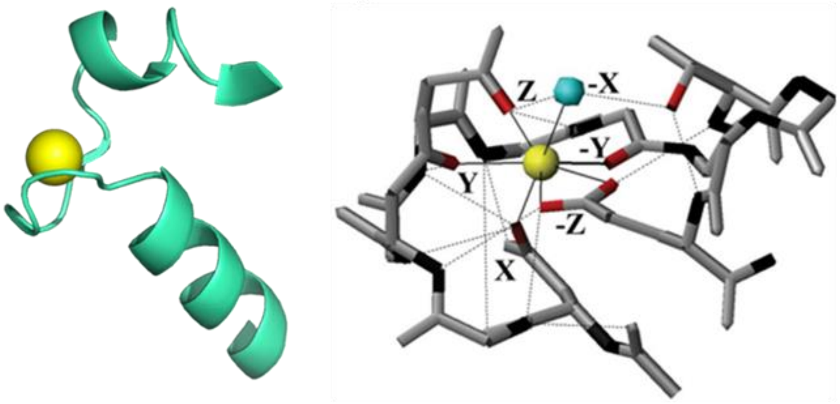

Figure 1.4: Helix-loop-helix structural motif found in Ca^{2+} binding site in parvalbumin (PDB ID 1B8R) (left panel). Ca^{2+} coordination in EF -hand showing the canonical pentagonal bipyramidal geometry (continuous thin lines) and the hydrogen bonding pattern (dashed lines). The side-chain oxygen atoms are shown in red, the Ca^{2+} ion in yellow and the coordinating water molecule in blue. Adapted from Gifford et al. (Gifford et al., 2007). (Right panel)

The binding of Ca^{2+} to EF hands results in a conformational change which, in most CBPs, exposes a hydrophobic surface which allows the protein to bind to a target sequence as seen in Figure 1.2 for calmodulin. On the other hand, in some other CBPs, the Ca^{2+} association to EF hands triggers the formation of non-covalent dimers which then enclose

Table 1.1: Sequence of amino acid residues in canonical calcium binding loop. Adapted from (Gifford et al., 2007)

EF-loop position	1	2	3	4	5	6	7	8	9	10	11	12
coordinating ligand	X		Y		Z		-Y		-X			-Z
Most common	Asp 100 %	Lys 29 %	Asp 76 %	Gly 56 %	Asp 76 %	Gly 96 %	Thr 23 %	Ile 68 %	Asp 32 %	Phe 23 %	Glu 29 %	Glu 92 %
Frequently observed		Ala Gln Thr Val Ile Ser Glu Arg	Asn	Lys Arg Asn	Asn		Phe Lys Gln Tyr Glu Arg	Val Leu	Ser Thr Glu Asn Gly Gln	Tyr Ala Thr Leu Glu Lys	Asp Lys Ala Pro Asn	Asp

the target peptide , such as the case of S100 human psoriasin , shown in Figure 1.5 (Lewit-Bentley & Réty, 2000).

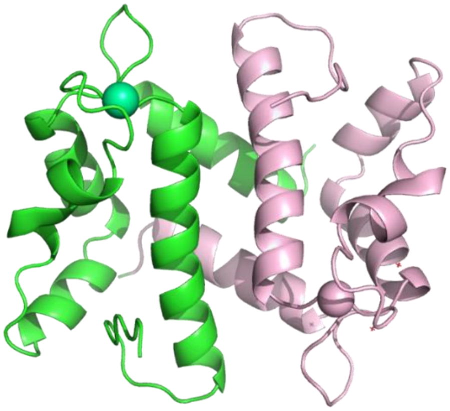

Figure 1.5: Structure of a dimeric form human psoriasin (S100A7), PDB ID 1PSR.

The C-2 domain Ca^{2+} binding motifs are present in β conformational Ca^{2+} sensors. They are organized in a β-sandwich arrangement (Figure 1.6), can coordinate up to 7 ligands following an equatorial geometry and have a μM affinity for Ca^{2+} (Srivastava et al., 2014). The βγ-crystallin motif still remains unclear whether it falls among the category of Ca^{2+} sensors, however, it can bind to Ca^{2+} with a μM–mM affinity. Its coordination number can vary from 5-8 and follows a planar geometry (Figure 1.6). (Srivastava et al., 2014)

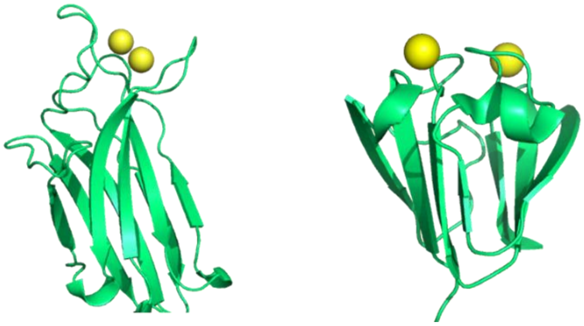

Figure 1.6: Structure of C2 domain motif from phosphoinositide-specific phospholipase c-delta1 from rat (PDB ID 1DJI) (left panel). Structure of a beta gamma-crystallin motif from an Archaea PDB ID 3HZ2 (right panel)

1.4 Neuronal calcium sensors family

Neuronal calcium sensors (NCS) are neuronal proteins that, as their name suggests, function as calcium sensors, being able to bind Ca^{2+} with a micromolar to sub micromolar affinity (D. Burgoyne, 2004) . All members of NCS proteins carry four EF-hands with EF hand 1 and EF- hand 2 being located in the N- terminal domain and EF-hand 3 and EF-hand 4 in the C- terminal domain. In all NCS members, the EF-hand 1 is non-functional as it contains a cysteine and proline residue in the Ca^{2+} binding loop which prevents Ca^{2+} binding. Some NCS members bind three calcium ions such as neuronal calcium sensor 1 whereas recoverin and potassium channel interacting proteins bind only two Ca^{2+} ions. (D. Burgoyne, 2004)

The NCS family is composed of five different classes: Class A (NCS1), Class B (VILIPS, neurocalcin, and hypocalcin), Class C: recoverin, Class D: GCAPs, and Class E: KChIP (D. Burgoyne, 2004) . In general, the N- terminal domain of this family shows a low sequence similarity while the C- terminal domain sequence is homologous among the members of this family as shown on Figure 1.7 . (Permiakov & Kretsinger, 2011).

Class A contains neuronal calcium sensor 1 (NCS1) and its *Drosophila* counterpart frequenine (Figure 1.8) which has been described in several organisms ranging from yeast to humans (Burgoyne, R. D. & Weiss, 2001; D. Burgoyne, 2004). It was first discovered in the study of Drosophila mutant in which an overexpression of frequenin resulted in an increase in neurotransmitter release and it has been associated with increased learning and memory in *C. elegans* (D. Burgoyne, 2004) .

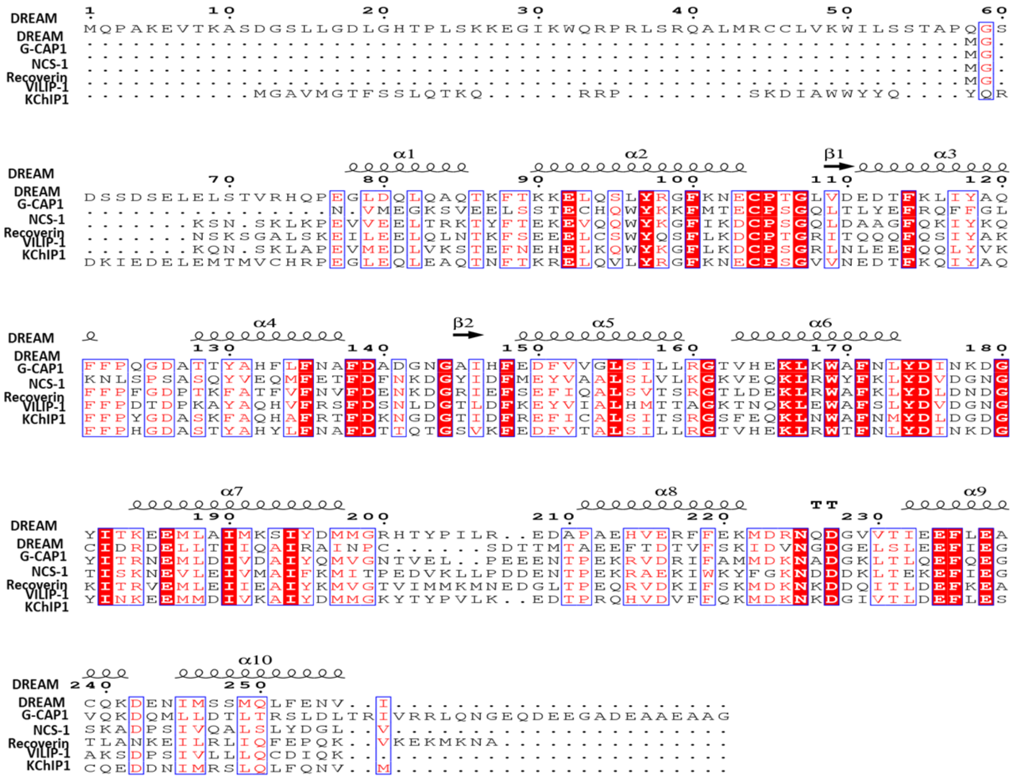

Figure 1.7: Sequence alignment of sequence of members from each class of the NCS family. Identical residues are highlighted in bold red and similar residues are shown in a red font.

NCS1 is able to bind up to three Ca^{2+}ions. As some other members of NCS family, NCS1 associates with lipid bilayers through a myristoyl group in its N terminal (Ames & Lim, 2012; Braunewell & Gundelfinger, 1999; Dason et al., 2012)

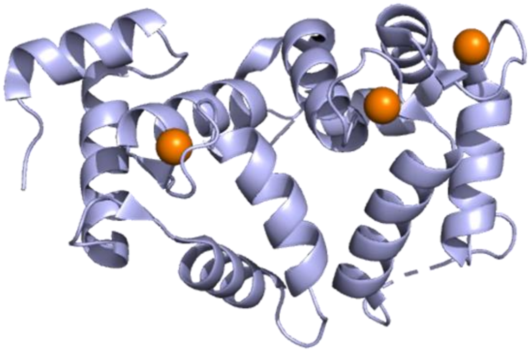

Figure 1.8: Structure for Ca^{2+} bound NCS1 (PDB ID 4GUK) showing the Ca^{2+} ions bound to EF hand 1-3 as orange spheres.

Class B is composed of three visinin-like proteins (VILIP 1-3), neurocalcin, and hipocalcin (Figure 1.9) . All three members of the class B are highly similar with a sequence homology ranging from 66 % to 94 % (D. Burgoyne, 2004) They have been involved in the desensitization of signal cascades in retinal photoreceptors (Braunewell & Gundelfinger, 1999).

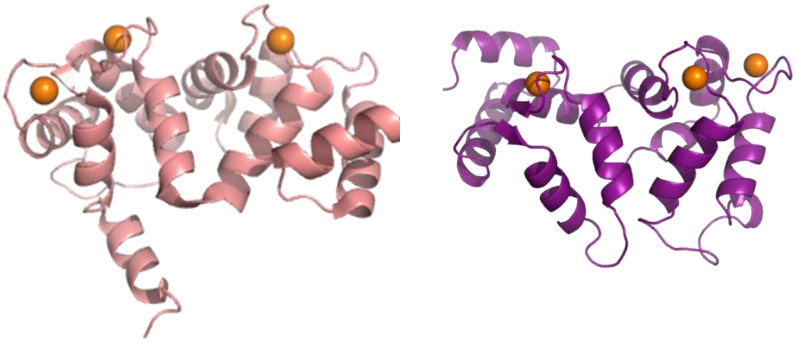

Figure 1.9: Structures of Ca^{2+} bound hippocalcin PDB ID 5G58 (left panel) and neurocalcin PDB ID 1BJF(right panel), showing the Ca^{2+} ions as orange spheres.

Class C is composed of only one protein, recoverin (Figure 1.10), which is expressed in photoreceptors cells of the retina and prevents the downregulation of rhodopsin (D. Burgoyne, 2004). This protein undergoes post-translational myristylation in the N-terminal. Ca^{2+} association to EF-hand 2 and EF-hand 3 leads to an exposure of the myristic group, so call myristic switch, facilitating membrane association.

Figure 1.10: Structure of Ca^{2+} bound myristoylated recoverin showing the Ca^{2+} ions as orange spheres.(PDB ID 1JSA).

Class D involves the guanylate cyclase activating protein 1-3 (GCAP) (guanylate cyclase activating proteins) which are also found exclusively in the retina and regulate the activity of guanylyl cyclase (D. Burgoyne, 2004). The structure of Ca^{2+} bound GCAP is shown in Figure 1.11

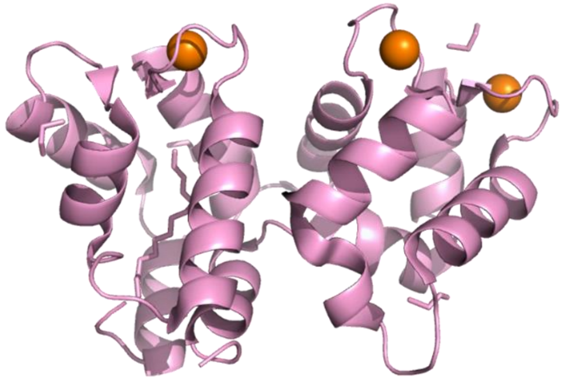

Figure 1.11: Structures of Ca^{2+} bound myristoylated guanylate cyclase activating protein-1 PDB ID 2I2R, showing the Ca^{2+} ions as orange spheres.

The last class of NCS proteins, class E, contains the Kv channel interacting proteins (Figure 1.12) , which as their name indicates, are able to interact with K^+ channels allow the flow of K^+ to restore membrane potential. There are 4 different types of KChIPs (1-4) as well as additional splice variants expressed in the neurons of the central nervous system with KChIP 2 being expressed in cardiac myocyte (D. Burgoyne, 2004) . The crystal structure of KChIP1 in complex with thecytosolic part of the Kv4.3 channels was determined by Yan et al. (Yan et al., 2007), the KCHIP 3 monomers associate to the T1 domain following a cross octameric shape as shoen on Figure 1.12 . In addition, has been suggested that KChIP 2 is able to interact with presenilin and also participates in the Ca^{2+}induced Ca^{2+}release from ER mediated by ryanodine receptors (Bähring, 2018)). KChIP 3 (also known as Downstream Regulatory Element Antagonist Modulator (DREAM) or calsenilin has been shown to be involved in the regulation of prodynorphin genes related to pain by binding to the DRE sequence in DNA in Ca^{2+} dependent manner and in the modulation of the kinetics of the Kv channels. (Burgoyne, Robert D. & Haynes, 2012; D. Burgoyne, 2004)

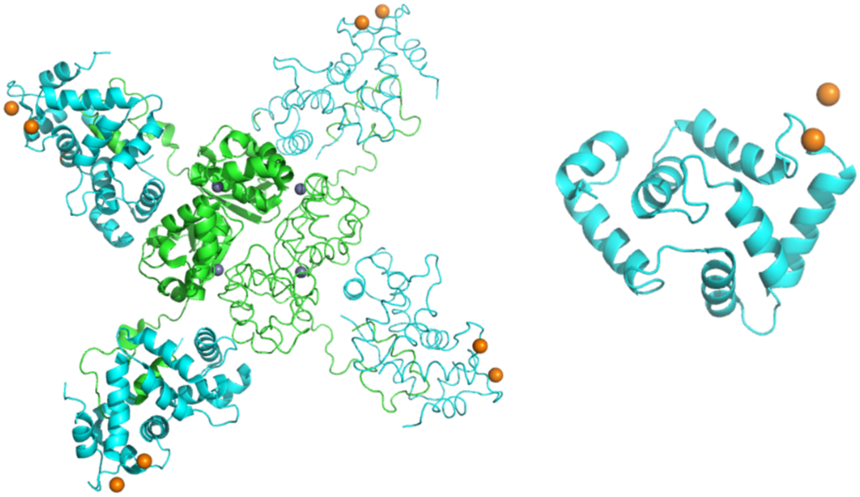

Figure 1.12: Structure of the complex between KChIP1:Kv4.3 T1 domain demonstrating an octameric cross-shaped complex of four KChIP1 in cyan and four T1 domain monomers shown in green (lPDB ID 2nz0)(left panel). Ca^{2+} bound KChIP1 monomer PDB ID 2nz0 (right panel)

1.1.5.Downstream Regulatory Element Antagonist (DREAM)

DREAM is a calcium binding protein which belongs to Class E of the neuronal calcium sensors. DREAM is also known as calsenilin or Potassium channel interacting protein 3 (KChIP3) and it was discovered in the early 2000s during three independent studies. As DREAM, it was involved in the transcription repression of prodynorphin and c-fos genes ; as KChIP3, interacting with the T1 domain of the Kv4.3 channels; and as calsenilin it interacted with presenilin 1 and 2 being involved with Alzheimer's disease (Philippov & Koch, 2007). It is present to a greater extent in the hippocampus, and it has been found to be present in several other tissues such as the thyroids and reproductive organs (Figure 1.13) (Fagerberg et al., 2014). KChIP3 is composed of three splice variants: KCHIP3.1 which has been taken as the canonical sequence and is expressed at higher levels in the brain and other organs in human and mouse tissues; and KChIP3.2 and KCHIP3.x , which are expressed at lower levels but are also present in both human and mouse tissues (Pruunsild & Timmusk, 2005) . These splice varianst have a high C terminal sequence similarity however they present differences in areas comprising around 30 residues in the the N terminal fragment (Figure 1.14) (Pruunsild & Timmusk, 2005).

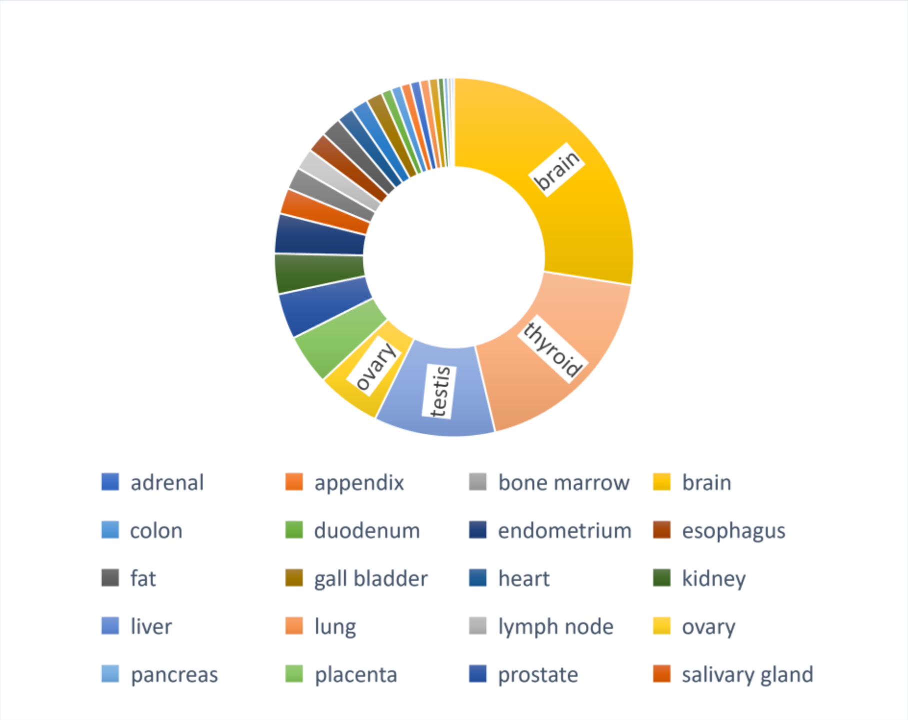

Figure 1.13: DREAM expression in different adult human tissues. Adapted from Fagerberg et al. Tissue samples taken from 95 human individuals representing 27 different tissues. (Fagerberg et al., 2014).

DREAM is a an approximately 29 kDa protein (Carrión et al., 1999) , it is composed of 256 amino acids, and contains 10 α helices and 4 EF hands summarized in Table 1.2 . DREAM structure was determined through NMR studies, the structure was determined using a truncated version of the protein including residues 75 to 256 (Figure 1.15), (Lusin et al., 2008).

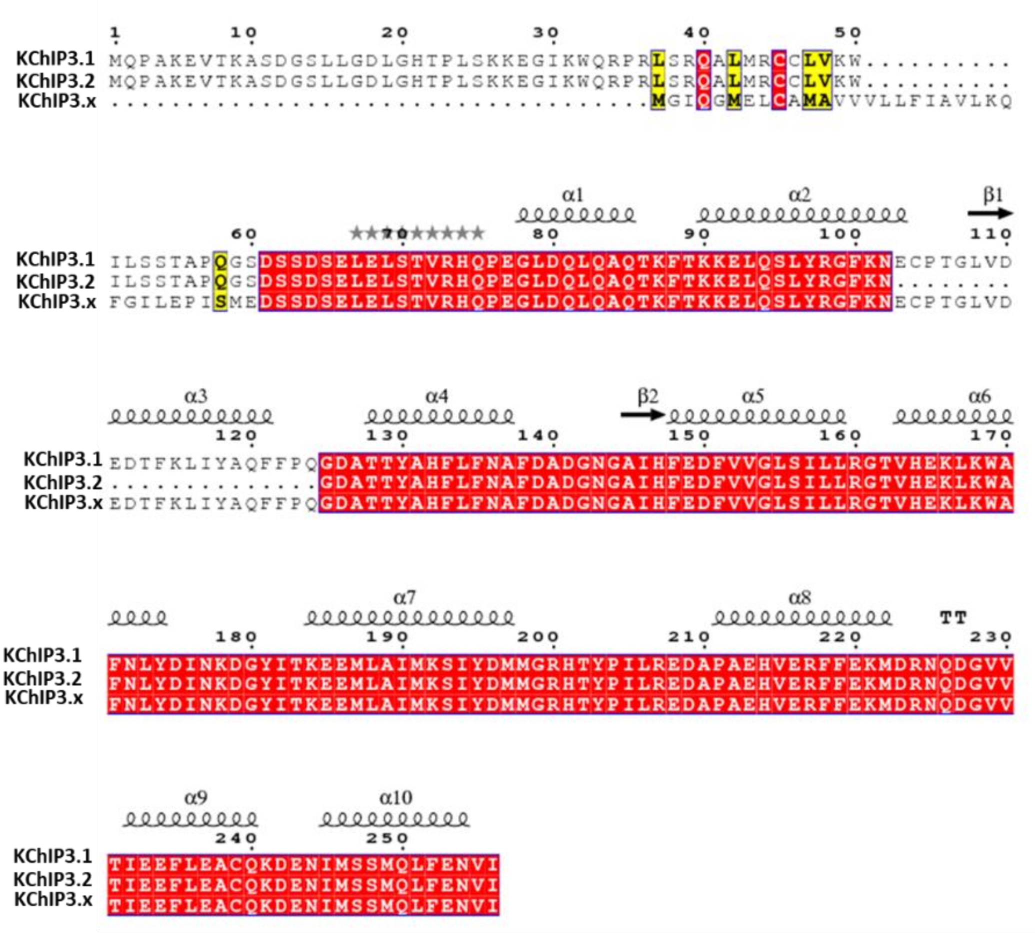

Figure 1.14: Sequence alingment of the three KChIP3 isoforms showing high C-terminal sequence similarity, identical resudes are highlithed in bold red.

As previously stated, EF hand 1 is not functional since it contains a proline residue at position 105 in the Ca^{2+}binding loop, EF hand 2 binds preferribly to Mg^{2+}, due to the presence of an Asp residue at position 150, with a K_d of 13 µM. On the C- terminal , it has been determined through ITC studies that EF hand 3 and 4 bind cooperatively to Ca^{2+} with a K_d of 1 µM (Masanori Osawa et al., 2001) . In addition to binding to Mg^{2+} and Ca^{2+}, DREAM also interacts with other non-physiological metals such DREAM has also been determined to bind to other metals such as Pb^{2+}, Cd^{2+} and Li^{+}, with relatively high affinity (Azam et al., 2019; Azam & Miksovska, 2019a; Azam et al., 2020a).

Table 1.2: Corresponding amino acid residues to EF hands and α Helices in DREAM. **(Lusin et al., 2008)**

Domain	**EF Hand**	**α Helix**	**Residue ID**
N- terminal Domain		**α 1**	**75-85**
	EFH 1	**α 2**	**90-103**
		α 3	**111-120**
	EFH 2	**α 4**	**128-138**
		α 5	**148-159**
C- terminal Domain	**EFH 3**	**α 6**	**163-174**
		α 7	**184-198**
	EFH 4	**α 8**	**211-222**
		α 9	**232-240**
		α 10	**243-254**

Furthermore, it can bind to hydrophobic molecules like arachidonic acid, potassium channel activator NS5806 , insulinotropic agent repaglinide and 1,8 ANS molecules (Gonzalez & Miksovska, 2014; Gonzalez et al., 2014; Naranjo et al., 2018)

Previous studies have suggested that, upon Ca^{2+}binding, DREAM undergoes an oligomerization change (Masanori Osawa et al., 2005; Yu et al., 2007). When Ca^{2+} is not present, DREAM is found in an equilibrium state between monomer-tetramer, whereas

Ca^{2+}binding to the C terminals leads to the formation of a stable dimer (Carrión et al., 1999; Gonzalez & Miksovska, 2014; Lusin et al., 2008).

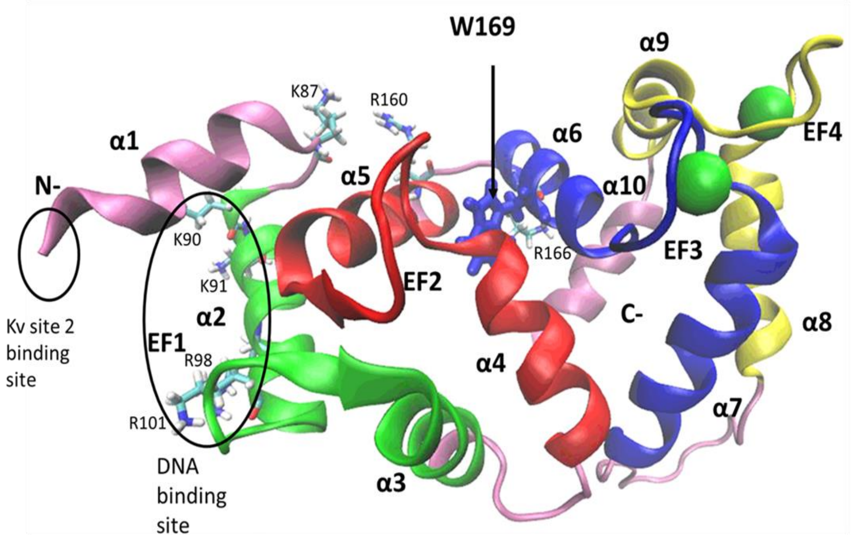

Figure 1.15: Structure of Ca^{2+}DREAMWT (PDB entry 2JUL) showing EF hands 1-4 in green, red, blue and are also shown. Ca^{2+} ions shown as yellow, respectively; proposed binding site for DNA and site 2 of the Kv channel green spheres and residues W169 is represented in licorice.

The dimer in DREAM is proposed to be stabilized by the residues Leu motif comprising amino acids at positions 155,158,159, and 251 (Lusin et al., 2008) (Figure 1.16) . In addition previous studies by Gonzalez et al. identify a structure stabilizing salt bridge including amino acids Glu 103 and Arg 200 and Arg 207. (Gonzalez, 2014)

Functionally, DREAM has been involved in the regulation of prodynorphin genes related to pain sensing, in the repression of c-fos,c-junk , and the apoptotic hrk gene in hematopoetic progenitor cells (Carrión et al., 1999; Cheng & Penninger, 2004; D. Burgoyne, 2004) Interestingly, DREAM has also been implicated in the regulation of circadian rhythms by the pineal gland and in the regulation of thyroglobulin expression (D. Burgoyne, 2004)

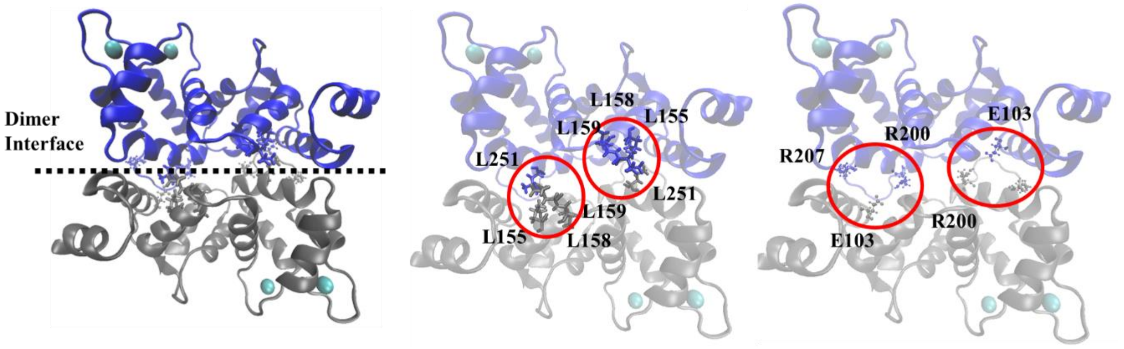

Figure 1.16: Proposed structure of the dimer by Lusin et al ,dimer interface with a head to tail orientation (left panel) , with Leu residues interactions circled and shown is sticks represenation (middle panel), additional satibilizing salt bridges circled and shown in CPK representation (right panel) , and Ca^{2+} ions shown as cyan spheres.

In the brain, DREAM has been associated with several neurological diseases including Alzheimer's disease, Huntington and Parkinson disease (López-Hurtado et al., 2018). Previous studies have also shown that DREAM interacts with the presenilin unit of the γ-secretase complex , enhancing the cleavage of amyloid precursor protein (APP) into aβ42 plaques , which are used as a post mortem diagnostic feature in Alzheimer's disease (Lilliehook et al., 1998)

In addition, DREAM has also been shown to inhibit the activity of the cAMP Response Element Binding Protein (CREB) and thereby regulating learning and memory . Studies conducted by Ooi *et.,al* suggested that , in the absence of Ca^{2+}, DREAM binds to the DRE sequence and represses the expression of genes regulated by the CREB/CREM complex (Ooi & Wood, 2008)

The interaction of DREAM with its intracellular partners is largely mediated by its confirmation state interacting with potassium channels as a monomer, with presenilin and calmodulin as a dimer, and with DNA as a monomer or tetramer (Carrión et al., 1999; Ping Liang et al., 2009; Yu et al., 2007). Nevertheless, despite the plethora of physiologic processes in which DREAM seems to play a crucial role, the precise mechanism by which Ca^{2+} modulates DREAM interaction with DNA and other ligands remains unknown.

2. MATERIALS AND METHODS

2.1 Chemicals and reagents

The reagents and solvents require in the protein preparation and purification were analytical grade and purchased from Sigma-Aldrich or Fischer Scientific. The $CaCl_2$, $MgCl_2$, $ZnCl_2$,EDTA and EGTA, were analytical grade and purchased from Sigma-Aldrich or Fischer Scientific. All buffers were prepared with ultrapure water (18.2 MΩ). The fluorescent probe 1,8-ANS, was purchased from Invitrogen., the 1,8-ANS stock was prepared in ultrapure water (18.2 MΩ) and stored at -20°C and the concentration was determined spectrophometrically using the extinctions coefficients in Table 2.1.. The fluorescently labeled peptides Site 1 and Site 2 were purchased from Thinkpeptides, the stocks were prepared in 20 mM Tris buffer pH 7.4 and the concentration was determined spectrophotometrically using the extinction coefficients listed in Table 2.1.

2.2 Protein purification and isolation.

The recombinant mouse DREAMWT (65-256) , which is a truncated version of the full length protein DREAM (1-256) ; and DREAM-NCS1 protein with a 6x His tag at the N-terminus were expressed in E. coli (DE 21) (Invitrogen). The E.coli cells were grown in Terrific Broth (TB) media at 37ºC and at a speed of 250 rpm for 12 h. Isopropyl β-D-1-thiogalactopyranoside (IPTG) was added when optical density at 600 nm (OD) reached 0.75 and cells were grown for additional 12 h at room temperature . Cells were obtained using an ST 16R centrifuge, Thermal Scientific at a temperature of 4 °C and 5000 rpm for 20 min. The cells obtained were treated with lysis buffer pH =8.0 . The lysis buffer is prepared with 20 mM Tris-HCl, pH 8.0, 300 mM NaCl, 1 mM β-mercaptoethanol, 20% glycerol, 1mM phenylmethyl sulfonyl fluoride (PMSF), 0.2% Tween 20, 20 µg/mL DNase

I, 5 µg/mL lysozyme, and 5 mM $MgCl_2$ and the pH was adjusted to 8.0 . Cells were broken through sonication using a sonic dismembrator , model 100, Fisher Scientific at 20V, for intervals of 30 seconds with 30 seconds of resting on ice between each interval for a total amount of 1hour the initial day the cells were put on lysis buffer , and the process was repeated after the cells were left overnight in the lysis buffer. Disrupted cells were centrifuged for 6 hours at 5000 rpm and supernatant was collected. Supernatant was then passed through a Ni-NTA affinity column (Quiagen) equilibrated with buffer A containing 20 mM Tris-HCl, pH 7.4 , 300 mM NaCl, and 100 mM CaCl . The column was washed with an increasing concentration of imidazole in buffer A (10 mM , 20 mM and 40 mM) until the OD of the eluate at 280 was less than 0.002. After the 40 mM Imidazole wash the protein was eluted with buffer A containing 250 mM imidazole. Protein was then dialyzed against a 20 mM Tris buffer pH 7.4 to remove residual imidazole and passed through an anion exchanged di-ethyl-amino-ethyl (DEAE) column, which was consecutively washed with 20 mM Tris buffer pH 7.4 containing an increasing NaCl concentration (20 mM ,40 mM , and 80 mM NaCl). The protein was eluted with 200 mM NaCl in 20 mM Tris buffer pH 7.4 and dialyzed against 20 mM TRIS pH 7.4 overnight. The concentration of the protein was determined spectrophotometrically using theextinction coefficients listed in Table 2.1 and the Ca2+ binding properties were characterized using emission spectroscopy and circular dichroism spectroscopy as described below.

2.3 UV-VIS absorption spectroscopy

Amino acid residues such as Trp, Phe and Tyr, which contain conjugated electrons in their structureprovide the ability to absorb light in the UV range from 250 nm to 300 nm for proteins and peptides. These π electron in the conjugated systems allow for the absorption of energy upon excitation and π ->π* electronic transitions are observed as shown in the Jablonski diagram (Figure 2.1)

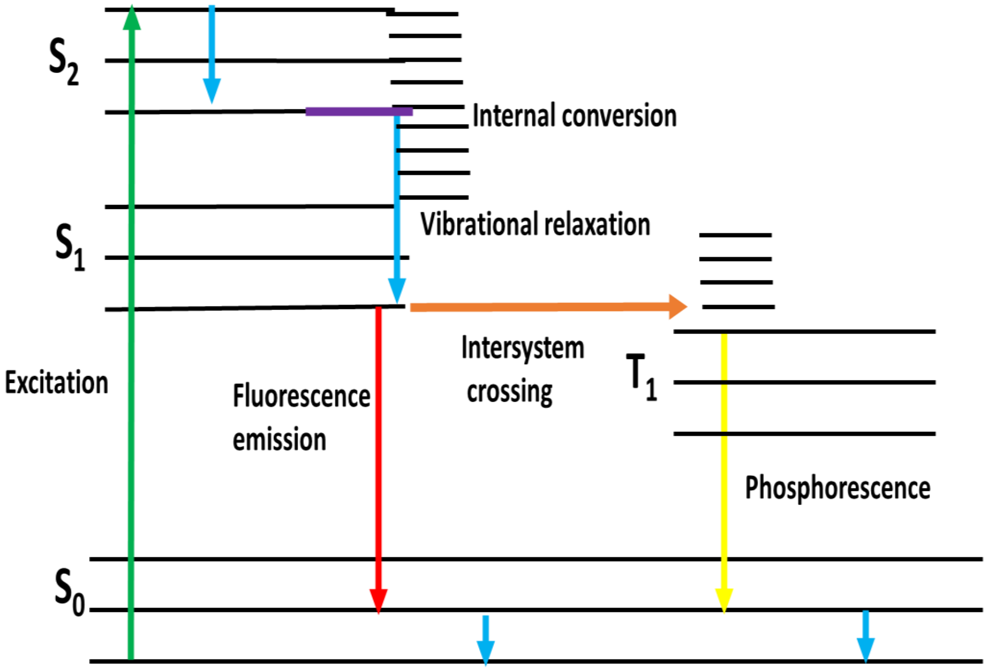

Figure 2.1: Perrin-Jablonski diagram representation . Transition between the different electronic states are indicated by colored arrows. Absorption is represented by the green arrow , emission is represented by the red arrow and phosphorescence is represented by the yellow arrow. Non-radiative processes are represented by arrows , internal conversion is represented purple , intersystem crossing is represented orange and vibrational relaxation is represented in blue.

The absorbance (A) is determined as a ratio of the intensity of light before (Io) and after (I) it passes through an optical cell according to (Equation 2.1).

$$A = \log\frac{I_o}{I} \qquad (2.1)$$

the concentration of the protein sample can be determined using Beers Lambert Law (Equation 2.2) based on the absorbance value

$$A = \varepsilon bc \tag{2.2}$$

where ε is the extinction coefficient in cm^{-1}M^{-1}, b is the pathway in cm and c is the concentration in mol L^{-1}. The values of extinction coefficients used in this study are summarized in Table 2.1.

2.4 Steady state emission process

The emission spectrum represents the measure of the light intensity that emitted by a sample as a function of wavelength, after the sample has been excited at a specific wavelength (Jameson, 2014; Lakowicz, 2006; Stryer, 1965)The Trp is widely used as an intrinsic probe in proteins due to its sensibility to the environment . Therefore, its emission properties can be used to monitor protein tertiary structure changes (Jameson, 2014)

Table 2.1: Extinction coefficient values used in this study

	λ max (nm)	Extinction coefficient (cm^{-1}M^{-1})	Source
DREAM WT	280	19 000	(Gonzalez, 2014)
DREAM-NCS 1	280	19 000	(Gonzalez, 2014)
1,8-ANS	350	5000	(Stryer, 1965)
Kv 4.3 Site 1	493	80 000	((Gonzalez, 2014)
Kv 4.3 Site 2	493	75 000	(Azam & Miksovska, 2019)

DREAM protein possess a single Trp residue at position 169 , which is conveniently located in a hydrophobic cavity among the N and C terminal of the protein (Lusin et al., 2008) . This residue was used as a probe to monitor the changes in the protein tertiary structure upon Ca^{2+} association to the protein. The Trp emission spectra were recorded using PC1 fluorimeter. The samples were excited with a 280 nm output from the Xe lamp and emission was collected in 90-degree orientation from 300 nm to 470 nm. The samples for emission measurements contained 15 -µM protein in 20 mM Tris buffer pH 7.4. The sample was placed in a 0.1x1.0 cm or 0.2 x 1.0 cm quartz cuvette. The apo, Mg^{2+}, Ca^{2+} and Ca^{2+} Mg^{2+}bound protein was prepared by adding 5 mM EDTA,5 mM EGTA, 1 mM $MgCl_2$ and/or 1 mM $CaCl_2$ to each sample.

2.5 Fluorescence lifetime

The fluorescence lifetime of fluorophore (τ) is the measure of how much time the molecule spends in the excited state which indicates the time between absorption and emission (Jameson, 2014), Fluorescence lifetime is expressed by expressed by Equation 2.3, where τ is the lifetime in ns , k_{rad} is the rate constant for radiative processes and k_{nonrad} is the rate constant for non-radiative processes.

$$\tau = \frac{1}{krad+knonrad} \tag{2.3}$$

The lifetime values of intrinsic or extrinsic fluorescence probes in protein provides information on structural and dynamic properties of the protein and are needed to determined other parameters such as anisotropy decay (Jameson, 2014). The fluorescence lifetime can be measured either in the time domain or in the frequency domain (Jameson, 2014).For the measurements in the time domain approach the sample is excites with a short laser pulse and the change in intensity is measured as a function of time (Jameson, 2014), while in the frequency domain approach, the sample is excited using a continuous light source modulated at different high frequencies from 2 MHz to 200 MHz in a sinusoidal manner, due to the excitation of the sample, the emitted light shown a frequency phase shift and amplitude modulation with respect to the excitation source modulated emission light (Jameson, 2014; Lakowicz, 2006). The lifetime values are determined by analyzing the experimental data and using several mathematical models such as sum of multiple exponential decay, Gaussian distribution, Lorentz distribution etc.(Jameson, 2014) . The lifetime data presented in this study were measured in the frequency domain using Chrono FM fluorometer (ISS, Chapagain Illinois)

The samples for Trp fluorescence lifetime measurements contained 20 μM protein in 20 mM Tris buffer pH 7.4. The apo, Mg^{2+}, Ca^{2+} and $Mg^{2+}Ca^{2+}$ bound proteins were prepared by adding 5 mM EDTA, 5 mM EGTA, 1 mM $MgCl_2$ and/or 1 mM $CaCl_2$ into proteins samples. 2.5-diphenyl-oxazole (PPO) with the lifetime of 1.4 ns was used as a reference compound. The sample was excited with 280 nm laser diode and the emission intensity was collected using a 305 nm long pass filter (Andover). The plots of phase modulation and phase shift as a function of modulation frequency were fitted using a three exponential decays model. The quality of the fit was judged by a χ^2 value and residual.

The samples for measuring emission lifetime of DREAM in the presence of 1,8-ANS contained 20 μM protein in 20 mM Tris buffer pH 7.4 and 20 μM 1,8-ANS. The apo, Mg^{2+}, Ca^{2+} and $Mg^{2+}Ca^{2+}$ bound proteins were prepared by adding 5 mM EDTA, 5 mM EGTA, 1 mM $MgCl_2$ and/or 1 mM $CaCl_2$ into proteins samples. The samples were placed in a 0.1x1.0 cm or 0.2 x 1.0 cm quartz cuvette and the output of 305 nm diode was used for the excitation. The emission intensity was collected using a 400 nm long pass filter (Andover Corp). The plots of phase modulation and phase shift as a function of modulation frequency were fitted using a three exponential decays model. The quality of the fit was judged by a χ^2 value and residual.

2.6 Anisotropy measurements

The anisotropy measurements are used to determine rotational mobility of a fluorophore by monitoring the ratio of the emitted light using different orientation of one polarizer placed in the excitation path and another polarizer placed in the emission path , anisotropy is calculated using the Equation 2.4 . (Jameson, 2014), where A represents anisotropy and I_{II} and $I_{\perp}$ represent the parallel and perpendicular orientation of the polarizers.

$$A = \frac{I_{II} - I_{\perp}}{I_{II} + 2I_{\perp}} \qquad (2.4)$$

The excitation light passes through a polarizer placed in the excitation path and only fluorophore molecules that have a transition dipole moment aligned with the electric field of the excitation light are excited. The polarization of the emitted light corresponds to the orientation of the transient dipole moment of the excited molecule at the time when light is emitted (Lakowicz, 2006). The emitted light is depolarized for the case of small molecules that freely rotate in the solution, whereas light emitted by bigger molecules or molecules trapped in a membrane or a solid like environment emit light polarized in the orientation analogous to the polarization of the excitation light. (Jameson, 2014) The second polarizer placed in the path of the emitted light is in a parallel or perpendicular orientation with respect to the polarizer placed in the excitation path and the emission intensity is collected as shown in Figure 2.2. Since anisotropy values are proportional to the size of the fluorescent molecule, anisotropy is a useful approach to characterize the binding of small fluorescent molecules to proteins. The binding isotherm for fluorophore association to the protein can be constructed by measuring anisotropy as a function of increasing concentration of the protein, and the equilibrium association or dissociation constants can be determined by analyzing the experimental data using the appropriate model.

Here we used the anisotropy approach to measure the dissociation constant for binding of fluorescent labeled peptides that mimic DREAM binding sites in the T1 domain of potassium voltage channels, so called site 1 and site 2. The site 1 corresponds to the residues 2 to 22 of the T1 domain (FITC-AAGVAAWLPFARAAAIGWMPV)) and the site 2 corresponds to the residues 70 to 90 of the T1 domain (FITC-LLGSTEKEFFFNEDTKEYFFD). The peptides were labeled by a fluorescent probe fluorescein isothiocyanate (FITC) (Scheme 2.1) covalently attached the peptide N-terminal.

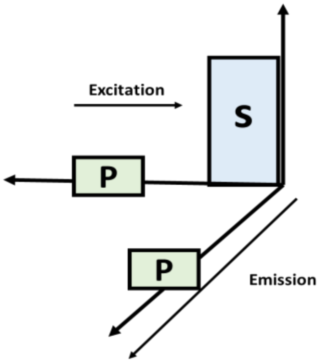

Figure 2.2: Position of the polarizers for the steady-state anisotropy measurements. The direction of the propagation of the excitation light and collected emitted light are sow as thin black arrows, the orientation of the polarizer placed in the excitation and emission path are shown in green squares .Adapted from Jameson 2004 (Jameson, 2014).

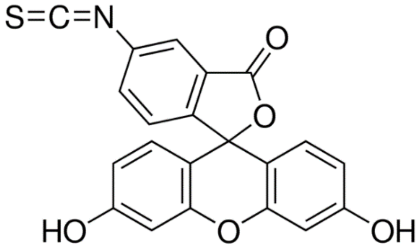

Scheme 2.1 Structure of FITC

Peptides were solubilized in 20 mM Tris buffer pH 7.8 and anisotropy was measured using 390 nm excitation light. The emission was collected through a long pass 500 nm long pass filter placed in the emission light pathway. Subsequently small aliquots of DREAM WT or DREAM-NCS1 protein were added, and anisotropy values were recorded. Each value of anisotropy corresponds to an average value determined for 10 measurements. The values of the anisotropy change were plotted as a function of protein concentration and the titration curves were analyzed using quadratic equation (Equation 2.5) and assuming a single binding site for each peptide.

$$\Delta A = \frac{\left(K_d + [P_t] + [L_t]\right) - \sqrt{(K_d + [P_t] + [L_t])^2 - 4[P_t][L_t]}}{2c} \qquad (2.5)$$

where ΔA is the change in anisotropy, K_d is the equilibrium dissociation constant, P_t is the total concentration of protein in the sample, L_t is the total ligand concentration of 0.5 µM, and c is the proportionality constant.

2.7 Circular Dichroism

Circular dichroism (CD) is a widely used technique to study protein secondary structure as well as protein stability (Greenfield, 2007). In CD measurements, difference in the absorbance of the right and left circularly polarized light in the far ultraviolet (UV) and near UV spectrum is determined as chiral chromophore have a different extinction coefficient for the left and right circularly polarized light. (Greenfield, 2007). The CD spectra of protein in the far UV (190 nm to 250 nm) provides information of the secondary structure of proteins major secondary structure elements, α-helices, β-sheets, and random coil, have a distinct CD spectrum as shown in Fig. 2.3.

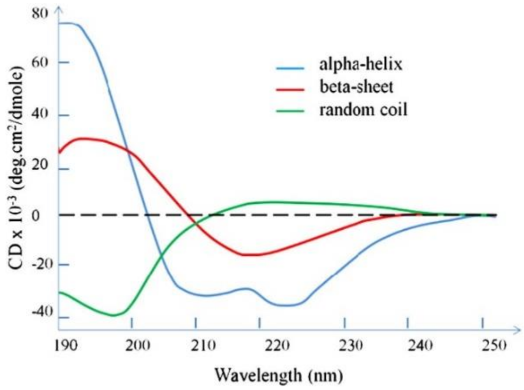

Figure 2.3: Typical CD spectra, showing the three major secondary structures of proteins, α- helix, β-sheet, and random coil with distinctive peak at specific wavelengths. Adapted from Wei et al. (Wei et al., 2014)

The α helical structures show a strong positive peak at 192 nm and two negative peaks at 208 and 222 nm. The β sheets show a negative peak at 218 nm and a positive peak at 196 nm , whereas random coils show only a very week CD signal (Greenfield, 2007). The monitoring of CD spectra in the near UV region are less common, however these data can provide information about structural changes in the environment of aromatic residues Phe, Tyr and Trp.

The samples for CD measurement contained 20 µM protein in 20 mM Tris buffer pH 7.4 placed in a 0.1 mm x1 cm quartz cuvette. The apo, Mg^{2+}, Ca^{2+} and $Mg^{2+}Ca^{2+}$ bound DREAM was prepared by adding 5 mM EDTA,5 mM EGTA, 1 mM $MgCl_2$ and/or 1 mM $CaCl_2$ to the protein samples. The data were collected from 190 to 260 nm using a J-810 Jasco CD spectrometer.

2.8 Materials and Methods for Chapter 4

The kinetics measurements were obtained by measuring the Trp fluorescence emission signal using the Kin Tek Corporation Stopped-flow (Model SF-300X) instrument excitation wavelength at 295nm , emission long pass filter 305nm.

The Ca^{2+} association experiments were done using from 10 to 50 µM DREAMWT in 20 mM Tris buffer pH 7.4 and 100 µM EDTA in one syringe and on the second syringe Ca^{2+} (concentration from 0.001 mM to 2 mM) in 20 mM Tris buffer pH 7.4. The same conditions were recreated for the measurements performed for the DREAMNCS1 mutant. The Ca^{2+} dissociation measurements were done using 40 µM DREAMWT and 1 mM Ca^{2+} in 20 mM Tris buffer pH 7.4 in one syringe and EDTA in 2o mM Tris buffer pH 7.4 EDTA, for several concentrations of EDTA (0.5-3.0mM) The same conditions were recreated for the measurement performed for the DREAMNCS1 mutant. For the measurements performed in the presence of NaCl both syringes were kept with the same concentration of Na Cl (0.1- 3.0 M)

Traces were fitted using the one exponential equation decay equation in the Origin 2018 Software (Origin Lab. Corp)

$$y = A1^{-x/t1} + y0 \qquad (2.6)$$

Fluorescence decay data were obtained using a ChronosFD spectrofluorometer (ISS) in the frequency domain mode. Fluorescence decay lifetime of the Trp was measured by exciting the sample with a 280 modulated laser diode. Fluorescence was collected through a 305 nm long pass filter. POPOP (1,4-bis(5-phenyloxazol-2- yl)benzene) in ethanol (τ = 1.35 ns) was used as lifetime references . Modulation-phase data were fitted, and the rotational correlation values were obtained using a two-decay discrete model available in the ISS software with fixed values for the Trp lifetime measured specifically for the sample.

The MD simulation were carried out using the previously obtained structure of the DREAM dimer WT (Gonzalez,2014) and mutating the amino acids Leu158 to Ser , Leu 159 to Thr and the loop at position 200 comprising amino acids RHTYPILR was replaced by the loop in NCS1 containing residues NTVELPEE The configuration files were obtained from the CHARM-GUI solutions builder tool (Jo et al., 2008)and carried out using the NAMD 2.14 software (Phillips et al., 2020). The CHARMM36 Particle Mesh Ewald (PME) algorithm was used to calculate long-range interactions with a 12 Å cutoff. The structure was inserted into a 12 Å distance from the edge of a TIP3 box and the system was minimized for 2000 steps using Langevin dynamics at 1 atm and 310 K. The analysis of the trajectory was performed using the VMD 1.9.3 software analysis tools (Humphrey et al., 1996) (Glykos, 2006; Humphrey et al., 1996). The dynamical network analysis was carried out using the VMD plug-in NetworkSetup and visualized using Network View (Glykos, 2006; Humphrey et al., 1996)

2.9 Materials and Methods for Chapter 5

The DREAM protein with two Ca^{2+} bound to EF-hand 3 and EF-hand 4 was obtained from the PDB Data bank PDB ID: 2JUL (Lusin, Vanarotti, Li, Valiveti, & Ames, 2008) .

This structure corresponds to a truncated version of the protein, residues 75-256, as the position of residues in the N- termini of the protein were not resolved by NMR likely due to the high flexibility of the N- termini. The initial structure of apoDREAM was prepared by removing two calcium ions from the original NMR structure, following 100 ns of aMD simulation by Gonzalez *et al* (Gonzalez, 2014). The DREAM mutant structure with amino Trp169 replaced by Ala was generated through the CHARM-GUI solution builder tool (Brooks et al., 2009; Jo, Kim, Iyer, & Im, 2008).

The protein was inserted into a rectangular water box using a TIP3 water box, with a 10 Å edge distance from the protein. The system was ionized with 0.15M KCl using Monte Carlo ion placing method. All atom molecular dynamic simulations Classical molecular dynamics (cMD) and Gaussian accelerated molecular dynamics (GaMD) (Miao et al., 2015a; Miao et al., 2015b) were carried out using the NAMD 2.14 software (Phillips et al., 2020) and the CHARMM36 Particle Mesh Ewald (PME) algorithm was used to calculate long range electrostatic interactions with a 12 Å cutoff. The system was minimized for 2000 steps using Langevin dynamics at 1 atm and 310 K.

The initial structure of DREAMW169A dimer was obtained by aligning the structures of Ca^{2+} bound DREAMW19A monomers to the model structure of DREAMWT dimer obtained from 100 ns MD simulation (Gonzalez, 2014).The simulation of the structure of DREAMW169A mutant was then carried out using the NAMD 2.14 software (Phillips et al., 2020) and the CHARMM36 Particle Mesh Ewald (PME) algorithm was used to calculate long-range interactions with a 12 Å cutoff. The dimer was inserted into a 12 Å distance from the edge of a TIP3 box and the system was minimized for 2000 steps using Langevin dynamics at 1 atm and 310 K.

The classical molecular dynamics (cMD) and Gaussian accelerated molecular dynamics (GaMD)simulations were analyzed using the VMD 1.9.3 software analysis tools (Humphrey, Dalke, & Schulten, 1996). The root mean square deviations (RMSD) were calculated for the alpha carbons in the protein throughout the simulation time using the RMSD tool in VMD, the RMSD provides information on the deviation in A form the initial structure , taking the structure at frame 0 as a reference .

The root mean squared fluctuations (RMSF) were calculated using the last frames of the simulation where the protein structure was equilibrated , these frames are determines using the RMSD values, the RMSF is calculated for each residue, and it provides information on the average fluctuation of the Cα using the average structure as a reference .

The salt bridges were identified using the Salt Bridges VMD plug-in and analyzed based on their position in the protein structure and distance between the residues to be less than 5 Å to determine their relevance. The dynamical network analysis was carried out using the VMD plug-in NetworkSetup and visualized using Network View (Glykos, 2006; Humphrey et al., 1996). In this approach, each alpha carbon is represented as a node, and the contacts were identified using restriction of not including neighboring alpha carbons. The communities were determined using the gncommunities plug-in based on the contact file (Glykos, 2006; Humphrey et al., 1996)

2.9.1 Gaussian accelerated Molecular dynamics

The gaussian accelerated molecular dynamics approach provides the structure with an energy boost that follows a Gaussian distribution. This approach is equivalent to running simulations on a longer time scale since it adds a harmonic boost potential smoothening the system potential energy surface and is able to identify distinct low energy states in the structure. (Miao et al., 2015)

The incorporation of the Gaussian is performed by adding the lines in Figure 2.4 to the configuration files of the simulation

```
#GAMD

accelMD         on
accelMDdual     on
accelMDdihe     on
accelMDG        on
accelMDGiE      1
#accelMDGirest   0
accelMDGcMDPrepSteps 200000
accelMDGcMDSteps  1000000
accelMDGEquiPrepSteps 200000
accelMDGEquiSteps 20000000
accelMDOutFreq  5000
accelMDGsigma0P 6.0
##accelMDGRestart on
```

Figure 2.4: Code used to incorporate the Gaussian accelerated MD approach to the simulation.

2.10 Materials and Methods for Chapter 6

Zinc Chloride > 97% purity was purchased from Sigma Aldrich. A 50mM stock solution of Zn_2Cl was prepared by dissolving Zn_2Cl in 20 mM Tris buffer (pH 7.4) and stored at 4 ºC. All measurements were carried out at room temperature. Reagents $CaCl_2$, $MgCl_2$, EDTA and EGTA and the reagents used for protein expression and purification were purchased from Sigma-Aldrich or Fischer Scientific. The hydrophobic fluorescent probe 1,8-ANS, was purchased from Invitrogen. 1,8-ANS, stock was prepared in ultrapure water (18.2 MΩ) and stored at -20°C and the concentration was determined spectrophotometrically using 5000 $cm^{-1}M^{-1}$ (350 nm) . (Cary50,Varian) Trp emission spectra were recorded using a Cary Eclipse Fluorescence Spectrophotometer from Agilent Technologies (280 nm excitation light) , 10 µM DREAM in 20 mM Tris buffer was placed in a 0.1x1 cm quartz cuvette. The apo, Mg^{2+}, Ca^{2+} and $Mg^{2+}Ca^{2+}$ bound protein was prepared by adding 5 mM EDTA,5 mM EGTA, 1 mM $MgCl_2$ and/or 1 mM $CaCl_2$ to the protein samples.

The DREAM and the DREAM-1,8ANS complex affinity for Zn^{2+} was determined in titration studies. 10 µM DREAM and 20 µM DREAM-1,8 ANS samples in metal free or metal bound form were titrated with Zn_2Cl and the emission spectra were recorded upon each addition. The fluorescent intensity at 330 nm (DREAM) and 475nm (DREAM-1,8ANS) were recorded and plotted as a function of Zn^{2+} concentration. The intensity was corrected for dilution effect and titration curves were analyzed using Hills equation.

$$F = B_{max} \frac{[Zn2Cl]^n}{[Zn2Cl]^n + K_d} \qquad (2.7)$$

Trp and 1,8 ANS fluorescence lifetime were determined in the frequency domain using Chrono FD fluorometer (ISS, Chapagain Illinois), and were excited at 280 nm and 305nm laser diode, respectively. The emission intensity was collected using a 320-400 nm band pass filter for Trp and 400-600 nm band pass filter for 1,8 ANS (Andover). The plots of phase modulation and phase shift as a function of modulation frequency were fitted using a three exponential decays model. The quality of the fit was judged by a χ^2 value and residual.

The samples for CD measurement for DREAM WT and DREAM-C contained 20 µM protein in 20 mM Tris buffer pH 7.4 placed in a 0.1 mm x1 cm quartz cuvette. The apo, Mg^{2+}, Ca^{2+} and $Mg^{2+}Ca^{2+}$ bound DREAM was prepared by adding 5 mM EDTA,5 mM EGTA, 1 mM $MgCl_2$ and/or 1 mM $CaCl_2$ to the protein samples and 100 µM Zn_2Cl was added to each sample . The data were collected from 190 to 300 nm using a J-810 Jasco CD spectrometer.

The Zn^{2+}binding sites predictions were obtained using the Metal ION binding site web tool MIB (Lin et al., 2016)The structure from the PDB data bank for DREAM PDB ID 2JUL was used to perform the analysis.

The MD simulation were carried out using the NMR DREAM structure PDB ID 2JUL and the Zn^{2+} atom coordinates from VMD. For the simulation in the absence of Ca^{2+} . The Ca^{2+} ions were removed from the Ca^{2+} binding site and replaced by two Zn^{2+} atoms using the

VMD program. For the simulation in the presence of Ca^{2+} , the Ca^{2+} remained in their binding site and 20 Zn^{2+} atoms were randomly placed using the VMD program . For both simulation the configuration files were obtained from the CHARM-GUI solutions builder tool and carried out using the NAMD 2.14 software (Phillips et al., 2020) . The CHARMM36 Particle Mesh Ewald (PME) algorithm was used to calculate long-range interactions with a 12 Å cutoff. The structure was inserted into a 12 Å distance from the edge of a TIP3 box and the system was minimized for 2000 steps using Langevin dynamics at 1 atm and 310 K.

The classical molecular dynamics (cMD) simulations were analyzed using the VMD 1.9.3 software analysis tools (Humphrey et al., 1996; Phillips et al., 2005; Phillips et al., 2020). The root mean square deviations (RMSD) were calculated for the alpha carbons in the protein throughout the simulation time using the RMSD tool in VMD. The root mean squared fluctuations (RMSF) were calculated using the last frames of the simulation where the protein structure was equilibrated.

3. OBJECTIVES

Neuronal calcium sensors represent a family of EF-hands proteins that regulate numerous neuronal processes in response to intracellular changes in Ca^{2+} concentration. Although members of this protein family share considerable sequence and structural similarities, they exhibit distinct metal binding properties as well as a wide range of interactions with diverse intracellular partners. The importance of this family of Ca^{2+} sensors is underline by the fact that they have been implicated in numerous neuronal diseases that reminds untreatable or the treatment options remind very limited. For example, DREAM was implicated in Alzheimer's disease, Huntington's disease, and neuronal calcium sensor 1 was implicated in Parkinson's disease. Here we have characterized structural and functional properties of DREAM with the main focus on understanding the mechanism of Ca^{2+} binding, proteins dimerization, allosteric network identification and the possible role of DREAM in Zn^{2+} neurotoxicity. The objectives of individual chapters are detailed bellow.

3.1 Objectives for Chapter 3.

The Ca^{2+} binding to the apo protein leads to a conformational transition that promotes protein dimerization as well as impact interactions of DREAM with several intracellular partners such DNA and $K_{v4.3}$ channels. The objective of this chapter is to characterize the mechanism Ca^{2+} association to apoDREAM and protein dimerization. By combining state of art kinetic studies with in-silico experiments we were able to show for the first time, that Ca^{2+} association to DREAM can be described using conformational selection model. More important, we show that Ca^{2+} association can be described as a two-step process with the first step corresponding to Ca^{2+} binding to a protein monomer and the second step representing dimerization of Ca^{2+} bound DREAM. As majority of the NCS members undergoes dimerization upon Ca^{2+} binding, these results help us to understand the Ca^{2+} triggered dimerization of DREAM but also other member of NCS family.

3.2 Objectives for Chapter 5

DREAM is involved in processes such as memory ,learning , pain sensitivity, kinetics of potassium channels, calcium homeostasis, gene expression and enzymatic activity of presenilin. The multifunctionality of this protein is due to its ability to interact with several intracellular partners such as presenilin , calmodulin , DNA and Kv channels . These interactions depend on the oligomerization state changes in DREAM which have been shown to be allosterically modulated upon Ca^{2+} binding. The mechanism of Ca^{2+} regulation of DREAM interactions is yet to be determined, however, previous molecular dynamics data proposed that a network of hydrophobic residues connecting the N and C terminal is crucial for the interdomain communication since it shows a reorientation upon Ca^{2+} binding , acting as molecular switch between the apo and the Ca^{2+} bound state. The Trp169 residue is key in this interdomain communication and its position in the core hydrophobic cavity is crucial to identifying the protein conformational changes. The objective of this chapter is to investigate the role of Trp169 in the transmission of the allosteric signal between the N- and C- terminal domain. These studies will provide information on the role of hydrophobic amino acid residues in allostery and are likely to be applied to other Neuronal Calcium sensors.

3.3 Objective for Chapter 6

Zn^{2+} is a crucial divalent metal that is necessary for the development and functioning of life . It interacts with a high number of proteins, and it has a role in numerous physiological processes such as growth , immune system development and homeostasis of other metal ions . Neurologically , it is involved in neural growth and development suggesting a similar role as the one seeing in Ca^{2+} for DREAM. Previous studies have shown that Zn^{2+} is able to bind to other neuronal calcium sensors such recoverin and NCS1 with relatively high affinity. On the other hand, DREAM interacts with Ca^{2+} and Mg^{2+} and it is able to bind to other metals such as Li^{+}, Pb^{2+} and Cd^{2+} with a relatively high affinity as well . Therefore , considering the high sequence and structure similarity among members of the NCS family and the role of Zn^{2+} in physiological processes and its presence in the organism , the objective of this chapter is to investigate the interactions of Zn^{2+} with DREAM and its impact in protein stability and interaction with other partners using fluorescence and CD studies and molecular dynamics approaches.

4. DREAM CHANGES IN OLIGOMERIZATION: KINETIC STUDY

4.1 Introduction

All life forms require a variety of biochemical reactions to carry out biological functions that are required for survival and reproduction (Milo & Phillips, 2015) These processes occur on specific time scales which can range from nano to microseconds (i.e., protein folding) to weeks (red blood cells production in the bone marrow). In addition, majority of biochemical processes involve an interaction between a ligand and a target molecule, thus, elucidation of the ligand-target molecule binding mechanism is crucial for understanding the mechanism of biological processes at a molecular level (Galletto et al., 2005).

Kinetic analysis is essential to establishing the mechanism of a reaction and is considered a powerful tool in the study of biological processes. For instance, the combination of rapid kinetic analysis and structural biology was used to determine the allostery role of trypsin-like proteases serine peptidases S1 family in basic metabolic processes such as digestion, apoptosis, and fertilization (Page & Di Cera, 2008) . Furthermore, characterization of kinetics of CBP calmodulin interactions with adenylyl cyclase 1 and 8 using stop flow approach has provided insight in differentiating mechanism of binding and regulation of CBP calmodulin and adenylyl cyclase 1 and 8 and their role in Ca^{2+} signaling and integrating cAMP in various physiological processes (Masada et al., 2012).

Binding of a ligand to a target molecule can be described as a one-step reaction as shown in Scheme 1, where k_{on} and k_{off} are the rate constants for ligand binding and complex dissociation, respectively (Pozzi et al., 2012). The interaction strength can be characterized by the association constant K_a (Equation 4.1) and/or the dissociation constant K_d (Equation

4.2). Although the one step model describes well the interactions between small molecules, it does not provide

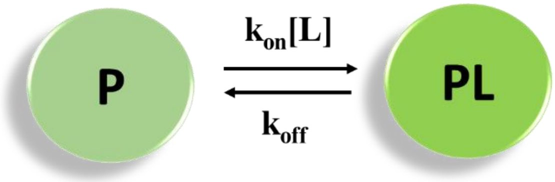

Scheme 1: Simplest representation of a ligand binding to a target molecule adapted from Vogt et. al (Vogt & Di Cera, 2012)

information about the mechanism of small molecules such as substrate or signaling molecules to protein or formation of protein complexes. Hence, several theories and models have emerged with the goal of better understanding the ligand-protein binding mechanism.

$$K_a = \frac{k_{on}}{k_{off}} \tag{4.1}$$

$$K_d = \frac{k_{off}}{k_{on}} \tag{4.2}$$

There are two main mechanism that are applied to describe complex between proteins and its ligands: conformational selection and induced fit (Cui & Karplus, 2008; Pozzi et al., 2012). Conformational selection, which corresponds to the Monod–Wyman–Changeux allosteric model, describes a process in which the target molecule is under a pre-existing equilibrium among two distinct conformations : P and P*, and the ligand binds favorably to only one of them: P, as represented on Scheme 2 (Changeux & Edelstein, 2011; Cui &

Karplus, 2008). The rate constants k_r and k_{-r} correspond to the transition among the two states present in the population of target molecules.

The induced fit mechanism corresponds to the alternative Koshland–Nemethy–Filmer allosteric model (Changeux & Edelstein, 2011). According to this mechanism, upon recognition of a ligand, the target molecule undergoes a conformational change to a loose complex (P*L) that is then optimized into final complex structure (PL).

Scheme 2: Mechanisms of ligand recognition: Conformational selection, adapted from Vogt et. al (Vogt & Di Cera, 2012)

The binding involves several steps which include the formation of a complex that represents the active form of the target molecule (P*L) as shown on Scheme 3. The rate constants k_r and k_{-r} correspond to the transition among the P*L and PL states (Vogt & Di Cera, 2012).

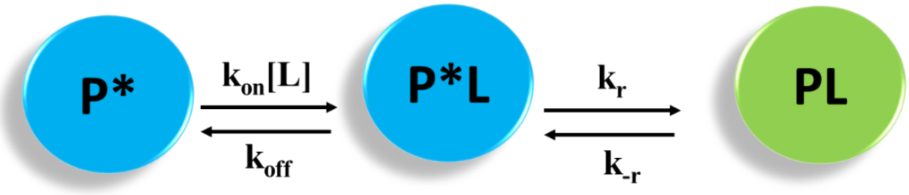

Scheme 3: Mechanisms of ligand recognition: Induced fit, adapted from Vogt et. al (Vogt & Di Cera, 2012)

In both, the conformational selection, and the induced fit models, it is assumed that the steps corresponding to binding and dissociation occur at a faster rate when compared to the conformational changes.(Changeux & Edelstein, 2011; Vogt & Di Cera, 2012). Under this assumption, the dependance of k_{obs} as a function of ligand concentration can be used to determined which mechanism is present in the process being studied (Changeux & Edelstein, 2011; Vogt & Di Cera, 2012). For the conformational selection model, a hyperbolic decrease of the k_{obs} as a function of increasing ligand concentration is obtained, according to equation 4.3, the K_d value is located at the midpoint between the asymptotic values of $k_{-r} + k_r$ for $[L] = 0$ and k_r for $[L] = \infty$. The observed plot represents a decrease in the target molecule P and P* states while the PL complex is formed (Vogt & Di Cera, 2012). This plot represents “unequivocal evidence” (Vogt & Di Cera, 2012) of the existence of a pre-equilibrium among two different conformations of the target molecule.

$$k_{obs} = k_r + k_{-r}\frac{1}{1+K_a[L]} = k_r + k_{-r}\frac{K_d}{K_d+[L]} \qquad (4.3)$$

On the other hand, in case of the induced fit model, a hyperbolic increase in the k_{obs} as a function of increasing ligand concentration is observed and such curves are analyzed using equation 4.4. The K_d value is also found at the midpoint for the asymptotic values of k_{-r} for $[L] = 0$ and $k_{-r} + k_r$ for $[L] = \infty$ (Vogt & Di Cera, 2012)The observed plot represents the increase in the P* state that leads to the P*L and PL formation steps. Nevertheless, the obtained plot does not constitute evidence of the presence of the mechanisms and further studies are required (Vogt & Di Cera, 2012).

$$k_{obs} = k_{-r} + k_r \frac{K_a[L]}{1+K_a[L]} = k_{-r} + k_r \frac{[L]}{K_d+[L]} \tag{4.4}$$

As kinetic analysis provides a sensitive tool to study the mechanism of protein ligand recognition and binding (Galletto et al., 2005) we have employed this approach together with *in silico* approach to characterize the Ca^{2+} association to DREAM, Downstream Regulatory Element Antagonism Modulator, and subsequent DREAM oligomerization process.

DREAM is a member of neuronal calcium sensor family that carries two functional EF hands, EF-hand 3 and EF-hand 4. DREAM has been shown to undergo an oligomerization transition upon Ca^{2+} binding to the C terminal domain (Craig et al., 2002; Masanori Osawa et al., 2005) (An et al., 2000; Carrión et al., 1999): in the absence of Ca^{2+}, DREAM is found in a monomer-tetramer equilibrium, whereas in the presence of Ca^{2+}, a stable dimer is formed (An et al., 2000; Carrión et al., 1999). Previous studies have shown that apo DREAM binds to DNA as a tetramer, whereas it interacts with potassium channels as a monomer suggesting that the DREAM oligomerization state is involved in the effector proteins recognition and binding. The apoDREAM structure or the structure of Ca^{2+} bound DREAM dimer has not been determined. Ames group (Lusin et al., 2008) have published NMR structure of the truncated form of DREAM (residues 76-256) with Ca^{2+} bound to EF-hand 3 and EF-hand 4. Based on the DREAM NMR structure and MD simulations data, it was proposed that the DREAM's monomers are oriented in the dimer structure in the head to tail orientation and the dimer is stabilized by hydrophobic interactions between Leu155, Leu159 and Leu251 from each monomer (Lusin et al., 2008) . In addition, previous MD data and time resolved anisotropy data from our group suggested that salt bridges between C-terminal Arg200 and Arg207 and N- terminal Glu 103 also contributes to the stabilization of the dimer as shown in Figure 4.1 (Gonzalez, 2014) and unpublished results.

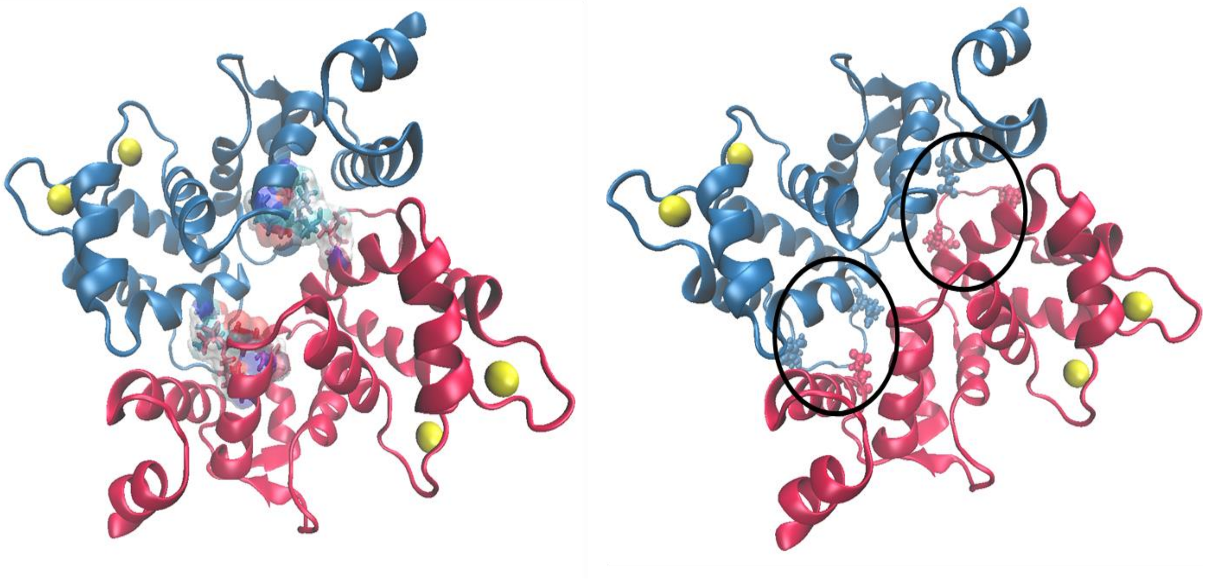

Figure 4.1: Model structure of DREAM dimer based on the NMR structure of DREM monomer (PDB entry *2JUL*). The structure shown in left demonstrates hydrophobic interactions between Leu 155, 159 and 251. The stabilizing salt bridges between Arg 200, Arg 207 and Glu 103 (in circle) are shown in right.

However, the precise mechanism of Ca^{2+} recognition and subsequent proteins dimerization has not been determined. We hypothesize that Ca^{2+} binds to the apoDREAM monomer forming a Ca^{2+} bound monomer which subsequently undergoes a dimerization as shown on Scheme 4.

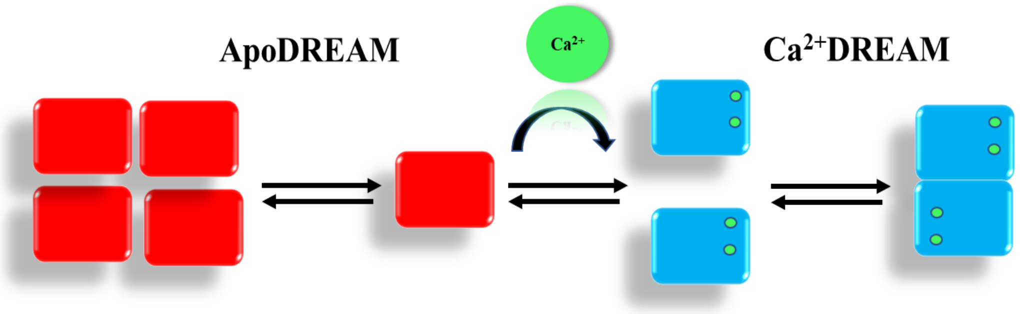

Scheme 4: Proposed mechanism for Ca^{2+} binding to apoDREAM and subsequent dimerization.

In this chapter, we combine the kinetics study with molecular dynamic characterization and site directed mutagenesis approach to determine the molecular mechanism of Ca^{2+} recognition and subsequent DREAM dimerization. To determine the role of charged residues in stabilization of DREAM structure we have prepared a mutated version of the protein DREAM-NCS1 where the residues involved in dimer stabilization were replaced. Namely, Leu158 and Leu159 were replaced by Thr and Ser, respectively. In addition, the loop containing the salt bridges starting at position 200 containing residues RHTYDILR were replaced by residues NTVELPEE that are found in the analogous loop in other neuronal calcium sensor, NCS1. The sequence overlay of mouse DREAM and DREAM-NCS1 construct is shown on Figure 4.2.

MELELSTVRHQPEGLDQLQAQTKFTKKELQSLYRGFKNECPTGLVDEDTFKLIYSQFFPQGDATTYAH
MELELSTVRHQPEGLDQLQAQTKFTKKELQSLYRGFKNECPTGLVDEDTFKLIYSQFFPQGDATTYAH

FLFNAFDADGNGAIHFEDFVVGLSILLRGTVHEKLKWA FNLYDINKDGCITKEEMLAIMKSIYDMMG
FLFNAFDADGNGAIHFEDFVVGLSITSRGTVHEKLKWA FNLYDINKDGCITKEEMLAIMKSIYDMMG

RHTYPILREDAPLEHVERFFQKMDRNQDGVVTIDEFLETCQ KDENIMNSMQLFENVIYLEHHHHHH
NTVELPEEEDAPLEHVERFFQKMDRNQDGVVTIDEFLETCQ KDENIMNSMQLFENVIYLEHHHHHH

Figure 4.2: **S**equence of mouse DREAM WT (red) with a start methionine residue (green) and a C-terminus His-tag (blue) connected by tripeptide linker (green). The DREAM-NCS (black) has identical sequence to the DREAM WT except residues L158, Leu159 replaced by Thr and Ser and the loop between EF-hand 3 and 4 (shown in yellow) replaced by the amino acid sequence found in human NCS-1 (underlined red).

4.2 RESULTS

4.2.1 Kinetic study of Ca^{2+} interactions with DREAMWT and DREAM-NCS1

Ca^{2+} association to DREAMWT and DREAM-NCS1 was studied using stopped flow fluorescence measurements by mixing apoDREAM or apoDREAM-NCS1 samples with Ca^{2+} in the absence or presence of Mg^{2+} and probing the change in the emission of a single Trp169 residue using 280 nm excitation wavelength. The kinetics of Ca2+ binding to NCS1 were investigated as a function of Ca^{2+} concentration or as a function of DREAM-NCS1 concentration. The typical traces for Ca^{2+} association to apoDREAM and NCS1- DREAM are shown in Figure 4.3 and 4.5 for 1mM Ca^{2+} concentration. In case of DREAMWT, two kinetics processes were resolved; a fast increase in the fluorescence emission that occurs on 100 ms timescale that is followed by a small increase in the emission that is observed on 10 s timescale. The fast increase in the Trp emission is somewhat surprising as the steady state emission spectra of apoDREAM and Ca^{2+} bound DREAM clearly show more efficient Trp quenching in the Ca^{2+} bound proteins (Figure 4.2.). The kinetic data were analyzed using a single or double exponential decay model. The analysis of the initial kinetic steps provides the time constant, $\tau_1 = 8 \pm 0.1$ ms, which can be attributed to the association of Ca^{2+} to the monomeric form of the protein. The studies performed for the mutated protein DREAM-NCS1 showed a similar fast increase in Trp emission for Ca^{2+} binding to DREAM-NCS1 with a $\tau_1 = 13.25 \pm 0.5$ ms as shown in Figure 4.3.

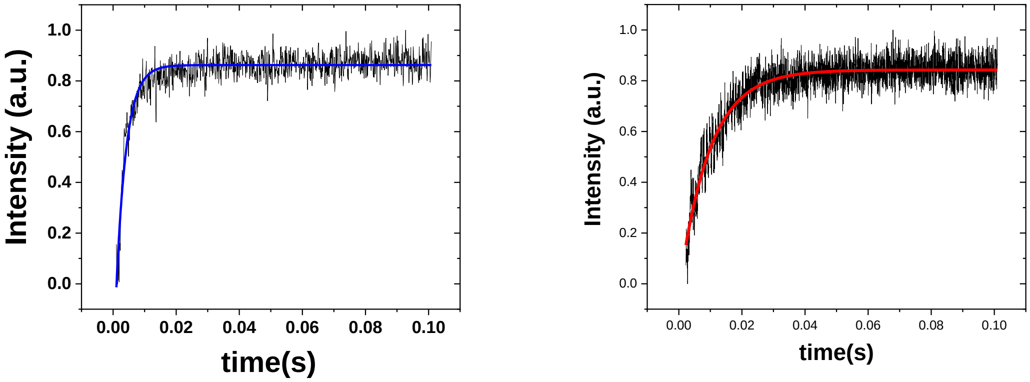

Figure 4.3: Rapid kinetics stopped flow fluorescence emission traces for DREAMWT (left panel) and DREAM-NCS1 (right panel) upon mixing with 1 mM Ca^{2+}.

The fast kinetics for Ca^{2+} association were characterized as a function of Ca^{2+} concentration and the plot of observed rate constant as a function of Ca^{2+} concentration is shown in Figure 4.4. k_{1obs} exhibits an inverse hyperbolic dependence on Ca^{2+} concentration. This type of plot indicates that Ca^{2+} association to DREAM can be described using the conformational selection model as described above and depicted in Scheme 2. According to this model, DREAM exists in two conformations which are in dynamic equilibrium: a Ca^{2+} binding conformation, P, and a non-binding conformation, P*. The equilibrium between P and P* conformation is characterized by the rate constants k_r and k_{-r} and the equilibrium constant, K_{eq} (Equation 4.5)

$$K_{eq} = \frac{k_r}{k_{-r}} \quad (4.5)$$

The experimental data were fitted using Equation 4.3. As the equilibrium dissociation constant for Ca^{2+} binding to DREAMWT was determined previously to be 1.0 µM (Masanori Osawa et al., 2005), this value was fixed during the data analysis. The obtained values of k_r for DREAMWT and DREAMNCS1 are 112 s^{-1} and 67 s^{-1}, respectively, showing a relatively more favored rate of formation of the ligand binding state P in e case of the WT construct when compared to the DREAM-NCS1 construct. The rate constants for the transition from P conformation to P* conformation are identical for both forms of the protein, k_{-r} = 230.3 ± s^{-1} for the DREAMWT and 239.07± 30 s^{-1} for the DREAM-NCS1. The rate constants determined for Ca^{2+} interactions with DREAMWT and DREAM-NCS1 are summarized in Table 4.1, the kon were determined using Equation 2.2 . These results indicate only a small impact of the introduced mutations on the equilibrium between Ca^{2+} binding and non-binding DREAM conformation and Ca^{2+} association to DREAM monomer.

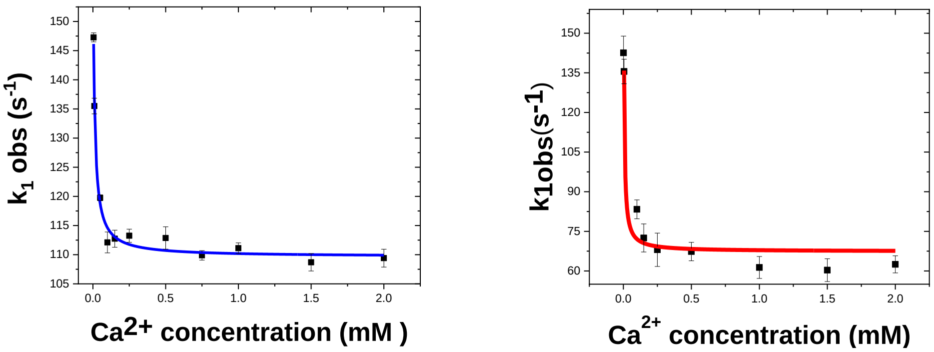

Figure 4.4: k_{obs} values obtained from rapid kinetics measurements of Ca^{2+} binding to DREAMWT (left panel) and DREAM-NCS1(right panel), determined from stopped flow measurements at increasing Ca^{2+} concentration

After the initial increase in the Trp emission, a second step was observed, that was accompanied by a decrease in the Trp emission intensity in case of DREAM WT. The analysis of the slow kinetic step using a single exponential decay model provided a time constant of $\tau_2 = 3.6 \pm 0.4$ s for DREAMWT. Unlike the kinetic traces for DREAMWT, a decrease in emission was not observed in the case of DREAM-NCS1 variant on the comparable time scale. Instead, an increase in the Trp 169 emission of a relatively small amplitude was observed as seen on Figure 4.5. This observation is in agreement with the Trp fluorescence steady state emission data that show a more efficient Trp 169 emission quenching in Ca^{2+}DREAM WT compared to the apoprotein, whereas the emission intensity of Trp residue in Ca^{2+}DREAM-NCS1 is enhanced compared to the apo form.

Table 4.1: The kinetics parameter for the first kinetic step of Ca^{2+} binding to DREAMWT and DREAM-NCS1

	Ligand	**k_{on} (M^{-1} s^{-1})**	**k_{off} (s^{-1})**	**k_r (s^{-1})**	**k_{-r} (s^{-1})**	**K_d (M)**
DREAM WT	Ca^{2+}	$1.12x10^8$± $2.9x10^3$	112±8	111.2± 0.8	230.3± 14	$1x10^{-6}$
DREAM-NCS1	Ca^{2+}	$9.02x10^7$± $1.2x10^5$	180±50	67.39± 3.5	239.7± 30	$2x10^{-6}$

The observed rate constant for the second step of Ca^{2+} binding to DREAMWT and DREAM-NCS1 was also probed as a function of increasing Ca^{2+} and protein concentration. The rate constant for the second kinetic step does not exhibit any dependence on Ca^{2+} or protein concentration, measured at 1 mm Ca^{2+} concentration, as shown in Figure 4.6.

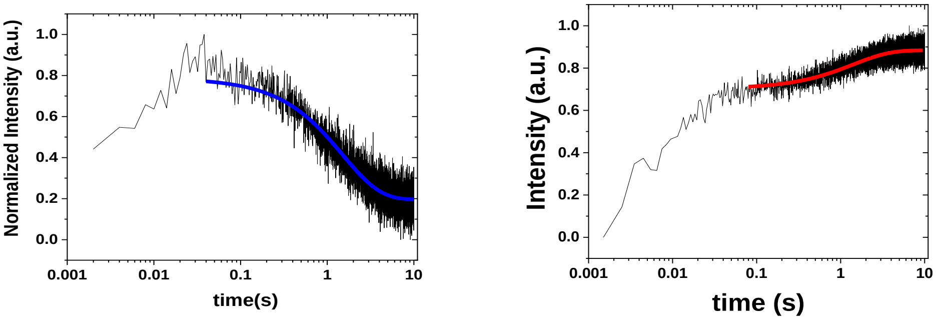

Figure 4.5: Slow kinetics stopped flow fluorescence emission traces for DREAMWT (left panel and DREAM -NCS1 (right panel) upon mixing with 1 mM Ca^{2+}.

The kinetics for Ca^{2+} dissociation from DREAMWT and DREAM-NCS1 were determined by mixing Ca^{2+} DREAM WT or Ca^{2+}DREAM-NCS1 with increasing concentration of EDTA (1.0 mM, 1.5 mM, and 2.0 mM EDTA) . In case of Ca^{2+}DREAMWT, the removal of Ca^{2+} leads to the decrease in the Trp emission, in agreement with the steady-state emission data. The traces were analyzed using a single exponential decay model and the koff values are listed in Table 4.1 for the fast step corresponding to Ca^{2+} association with the protein . The dissociation was measured using 1mM Ca^{2+}-40 µM DREAMWT and 1mM Ca^{2+}-DREAMNCS1 samples interacting with different EDTA concentrations (1.0 mM, 1.5 mM and 2.0 mM EDTA). Both, DREAMWT and DREAMNCS1 exhibited an increase in emission.

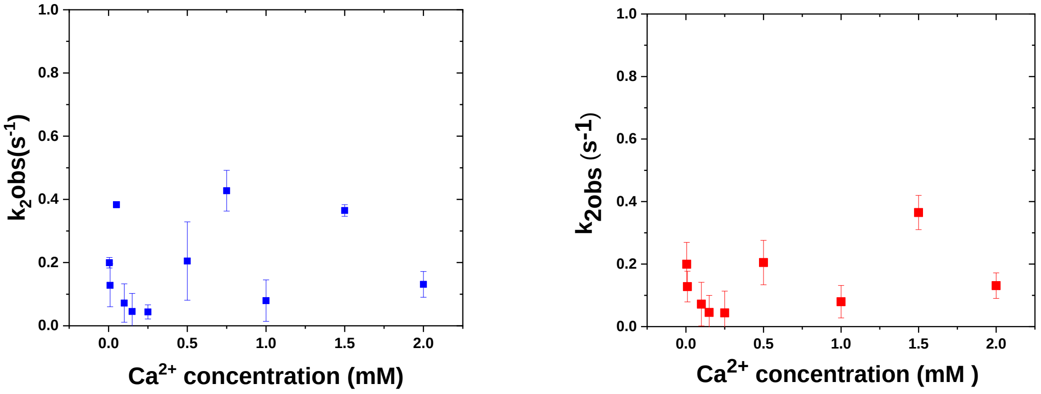

Figure 4.6: k_{obs} values for the slow kinetic step associated with Ca^{2+} binding to DREAMWT (left panel) and DREAM-NCS1(right panel) as a function of increasing Ca^{2+} concentration (DREAMWT shown in blue and DREAM-NCS1 shown in red)

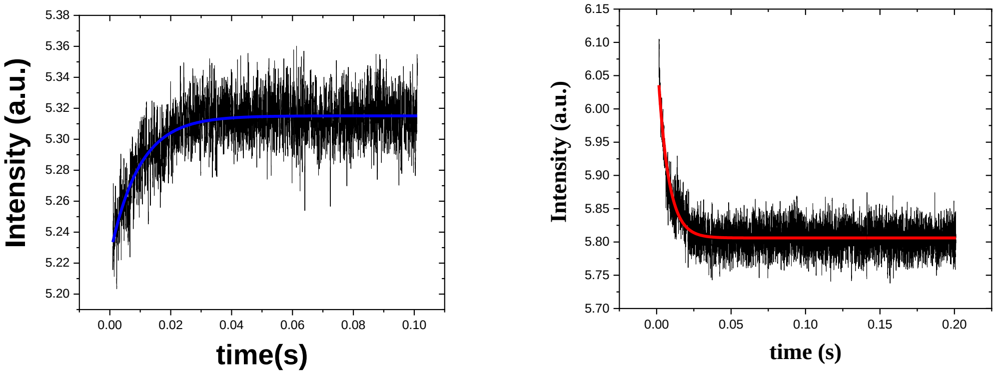

Figure 4.7: Rapid kinetics stopped flow fluorescence emission traces for Ca^{2+} dissociation from DREAMWT (left panel) and DREAM-NCS1 (right panel) in the presence of 1 mM EDTA.

4.2.2 Ca^{2+} association to DREAMWT in the presence of NaCl

Based on the model structure of Ca^{2+} DREAM dimer, the dimer structure is stabilized by salt bridges between individual monomers. To determine impact of the salt bridges on the Ca^{2+} binding kinetics we have monitored the kinetic traces for Ca^{2+} binding to DREAMWT and DREAM-NCS1 in the presence of increasing concentration of NaCl (from 0.1 M to 3.0 M NaCl) The kinetic study of Ca^{2+} association to DREAMWT was performed in the presence of NaCl ranging (only 0.1 M and 3.0 M shown for clarity). The fast kinetic step associated with Ca^{2+} association to DREAM WT in the presence of NaCl exhibited an increase in the amplitude, however, the k_{1obs} values decreased in the presence of the salt. Interestingly, the increase in the NaCl concentration significantly impacts the slow phase for Ca^{2+} association, i.e., at 3.0 M NaCl, the slow phase has not been observed.

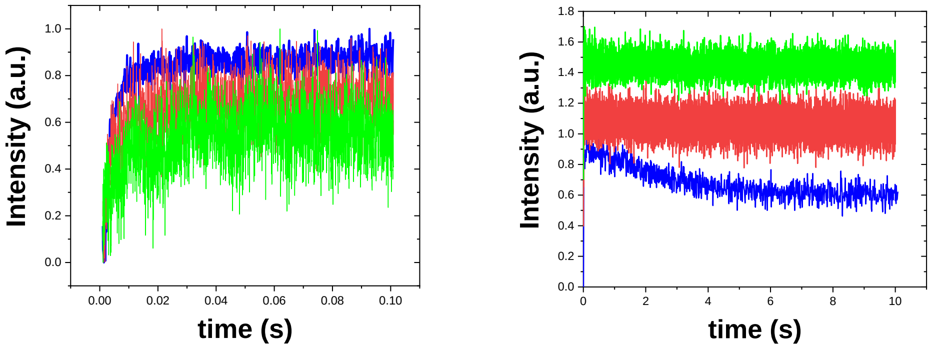

Figure 4.8: Fast (left panel) and slow (right panel) kinetics for stopped flow fluorescence emission traces for 40 µM DREAMWT upon mixing with 1 mM Ca^{2+} in the absence of NaCl (blue) and in the presence of 0.1 M NaCl (red) NaCl and 3 M NaCl (green).

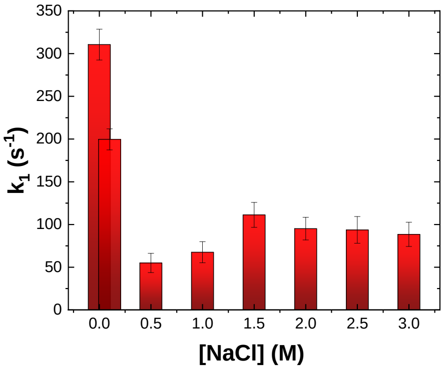

Figure 4.9: k_{1obs} values for the fast kinetics step of 1 mM Ca^{2+} association to 30 µM DREAMWT in the presence of increasing NaCl concentration.

4.2.3 Probing the oligomerization state of DREAM WT ad DREAM-NCS1 using time resolved anisotropy

The time resolved anisotropy measurements represent a convenient approach how to characterize the oligomerization state of proteins in solution by probing the rotational correlation time in time resolved anisotropy measurements. According to the Stokes–Einstein equation 4.6 (Gonzalez & Miksovska, 2014), the rotational correlation time of a fluorophore, Φ, is proportional to its hydrodynamic molecular volume, V, as shown in Equation 4.6.

$$\Phi = \frac{\eta V}{RT} \qquad (4.6)$$

where η represents the viscosity of water with a value of 1.02 mPa s, R is the perfect gas constant, and T is the temperature 293 K (Korson et al., 1969) (Gonzalez & Miksovska, 2014; Lakowicz, 2006).

The estimated rotational correlation times for DREAM WT and DREAM NCS1 monomer were previously calculated by Gonzalez et al. (Gonzalez & Miksovska, 2014), to be 12 ns, assuming the protein to have a spherical shape and using the molecular weight of the truncated DREAM and DREAM NCS1 of 23 kDa. The tetramer and dimer are expected to have a rotational time of 48 ns and 24 ns, respectively. The frequency domain anisotropy decay of Trp 169 in DREAMWT and DREAM-NCS1 was measured in the presence and absence of Ca^{2+} and the corresponding plots are shown in Figure 4.10, this measurement were measure using 30µM DREAMWT and 1mM of Ca^{2+} and 5 mM of EDTA for the $Ca^{2+}$and apo forms, respectively. The same conditions were used for the mutant. The analysis of the experimental date using a sum of two exponential decay model provided two rotational correlation times, Φ_1 and Φ_2 and these values are listed in Table 4.2. Φ_1 can be attributed to the rotation of Trp 169 sidechain around a single bond between C_α and C_β or C_β and C_γ as these values to values for Trp sidechain mobility in troponin C and its mutants (Φ = 0.33 ns to 1.46 ns) (She et al., 1997). Interestingly, the association of Ca^{2+} has only minimum impact on the Trp 169 sidechain mobility. The slower rotational correlation time, Φ_2, can be attributed to the tumbling motion of the protein and thus is proportional to the hydrodynamic molar volume of DREAM. The experimentally determined Φ_2 value of 21.9± 3 ns for the Ca^{2+} bound DREAMWT is similar to the rotational correlation time calculated for DREAM dimer, whereas the experimentally determined Φ_2 value of 10.5± 0.9 ns for the apoDREAMWT is consistent with the monomeric form of the protein. Additionally , the time resolved anisotropy measurements for Ca^{2+} bound DREAMWT in the presence of 3 M NaCl were performed, in order to determine the impact of the formation of salt bridges, a rotational time of 11.40±1.0 ns for Φ_2 was obtained . This value is consistent with the theoretically calculated value for the monomeric form of the protein , suggesting the presence of NaCl disrupted the salt bridges formation and hence the stability of the formation of the dimer.

These data confirm that the formation of the dimer upon Ca^{2+}binding to DREAMWT and the presence of the monomer in the Ca^{2+} free DREAMWT. The Φ_1 value determined for Ca^{2+}DREAM-NCS1 is similar to that measured for Ca^{2+}DREAMWT suggesting similar mobility

of Trp169 sidechain in both protein construct. The rotational correlation time of 14.9± 1 ns for Ca^{2+}DREAM-NCS1 indicates that this construct reminds in the monomeric form in the presence of Ca^{2+}. The S/N ratio for apoDREAM-NCS1 construct is higher and thus the data seems to be inconclusive, as the Φ_1 value of 18 ± 2 ns seems to be too large for apoDREAM-NCS1 monomer and small for DREAM-NCS1 dimer. It is also possible that the spherical model is not appropriate for this construct.

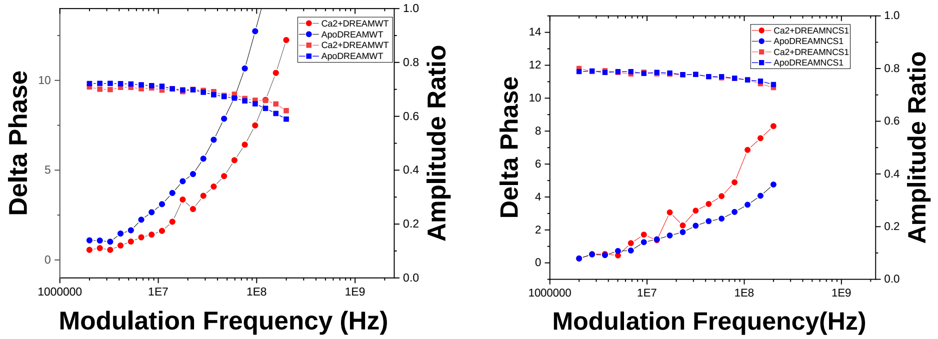

Figure 4.10: Frequency-domain tryptophan anisotropy decay traces for DREAMWT (left panel) and DREAMNCS1 (right panel) in the presence(red) and absence(blue) of Ca^{2+}

Table 4.2: Time-resolved anisotropy decay values for DREAMWT and in the presence and absence of Ca^{2+}

	Φ_1 (ns)	Φ_2 (ns)	r_1 (ns)	r_2 (ns)	<τ> (ns)	χ^2
Ca^{2+}DREAMWT	0.11± 0.06	21.9± 3.0	0.55± 0.20	0.110± 0.003	3.78	0.287
ApoDREAMWT	0.16± 0.02	10.5± 0.9	0.96± 0.07	0.106± 0.004	3.46	2.85
Ca^{2+}DREAMNCS1	0.12± 0.04	14.9± 1.0	0.38± 0.10	0.086± 0.002	4.28	1.39
ApoDREAMNCS1	0.06± 0.01	18.0± 2.0	0.34±0.20	0.089± 0.002	4.24	0.75
Ca^{2+}DREAMWT NaCl	0.19± 0.02	11.40±1.0	0.97±0.05	0.14±0.06	3.41	0.7

4.2.4 DREAMNCS-1 dimer MD simulation

In order to gain additional information structural properties of the DREAM-NCS1 variant, we have modeled the structure of Ca^{2+}DREAM-NCS1 dimer using a 350 ns cMD The Ca^{2+}DREAM-NCS1 dimer was models based on Ca^{2+}DREAM WT dimer (Gonzalez 2014) by mutating Leu residues, Leu 158 and Leu 159 into Ser and Thr and replacing the loop connecting EF-hand 3 and EF-hand 4 (Arg 200 to Arg 208) by the residues found in the neuronal calcium sensor 1. The dimer's structure was equilibrated and simulated for 350 ns. During the simulation, the individual DREAM-NCS1 monomers started to separate from each other at approximately 75 ns of simulation time and the separation process continued until the end of the simulation. At 350 ns of simulation time, both monomers were completely detached as demonstrated in Figure 4.11. These results are in agreement with the time resolved anisotropy data demonstrating that the removal of hydrophobic contacts between Leu residues and disruption of salt bridges prevents the formation of the DREAM dimeric form.

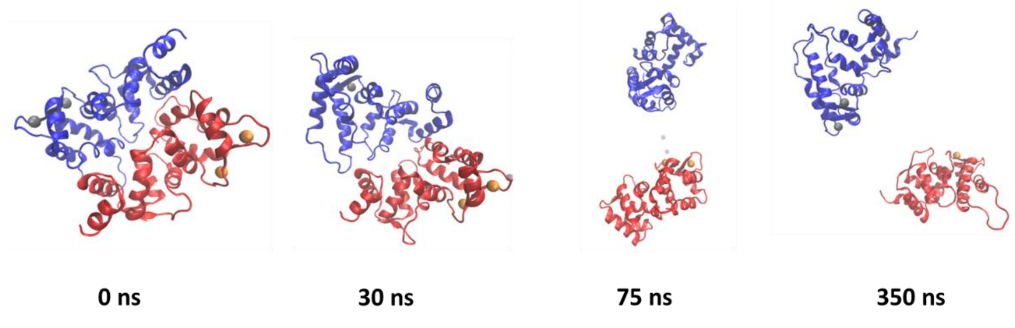
0 ns
30 ns
75 ns
350 ns

Figure 4.11: DREAM-NCS1 dimer structure at 0, 30 , 75 and 350 ns simulation time. Each subunit is colored in red and blue, Ca^{2+} ions represented as black and orange spheres.

To provide insight into the impact of the mutations in DREAM-NCS1 protein, the cMD structure of DREAN-NCS1 monomer obtained at 350 ns of simulation time was aligned with the structure of Ca^{2+}DREAMWT obtained by after 100 ns of MD simulation. Interestingly, both constructs exhibit a high similarity in the overall fold with an RMSD of 2.73 Å.

In order to determine the impact of mutations on the conformation of individual EF hands, an alignment of the individual EF hands in DREAM WT and DREAM-NCS1 was performed using the first 12 amino acids of the entering α helix of each hand (Figure 4.12). The overlay shows almost identical arrangement of α- helices in EF-hand 3 and EF-hand 4 that is consistent with the similar K$_d$ value for Ca^{2+} binding to DREAM WT and DREAM-NCS1. Interestingly, the largest structural deviation was determined for the orientation of α- helices in EF-hand 1.

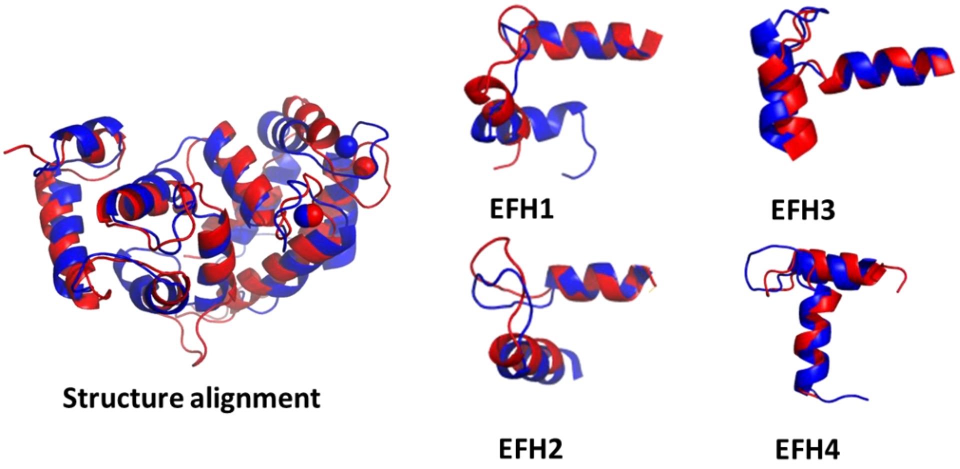

Figure 4.12: Left: Structure alignment of the monomer structure of DREAM-NCS1 in the presence of Ca^{2+} (in red) and Ca^{2+}DREAMWT (in blue). Right Individual EF hands alignment using the first 12 amino acids of the entering α helix. EF hands of DREAM-NCS1 are shown in red and EF-hands from DREAMWT are shown in blue.

4.2.4.1 Dynamic cross correlation analysis of DREAM-NCS1 structure

Although a knowledge of a rigid structure provides a valuable insight into protein's properties, the functional properties are often determined by the structural dynamics. In general, some parts of the protein structure are relatively rigid whereas other parts are more dynamics, and their dynamic motion can be correlated or uncorrelated with other parts of the protein structure. The dynamic properties of protein structure can be visualized by constructing dynamic cross correlation maps as shown in Figure 4.13 for DREAM-WT monomer, DREAM-WT dimer and DREAM-NCS1 monomer. The residues with correlated or anti-correlated motions can participate in so-called dynamic cross-correlation network, which can be used for transmission of information that is involved in the cooperative ligand binding and/or allosteric control. The dynamic cross correlation analysis of DREAMWT monomer demonstrate the absence of the highly correlated motion of residues in either N- or C- terminal domain. On the other hand, intermonomer interactions in the DREAM dimer structure leads to a highly correlated motion of the residues in the N- terminal domain that is somewhat decreased in the C- terminal domain. I speculate that such a high correlation in the structural dynamics may be involved in the allosteric signaling between N- and C- terminal domain in the DREAM-WT. The structure of DREAM-NCS1 dimer obtained after 350 ns of the simulation time, demonstrate, that separation of individual monomer of DREAM-NCS1 is associated with a loss of the dynamic correlation between the residues in the C- terminal domain and partially in the C-tegminal domain. Extension of the computation time may be necessary to achieve a decrease in the correlated motion that was observed in DREAM WT monomer and DREAM-NCS1 monomer.

Overall, the MD analysis showed a significant destabilization of Ca^{2+} bound DREAM-NCS1 dimer into individual monomers but it did not exhibit major structural difference for the monomer when compared to the DREAMWT monomers, suggesting interplay between the protein dynamics and stability of the dimeric structure.

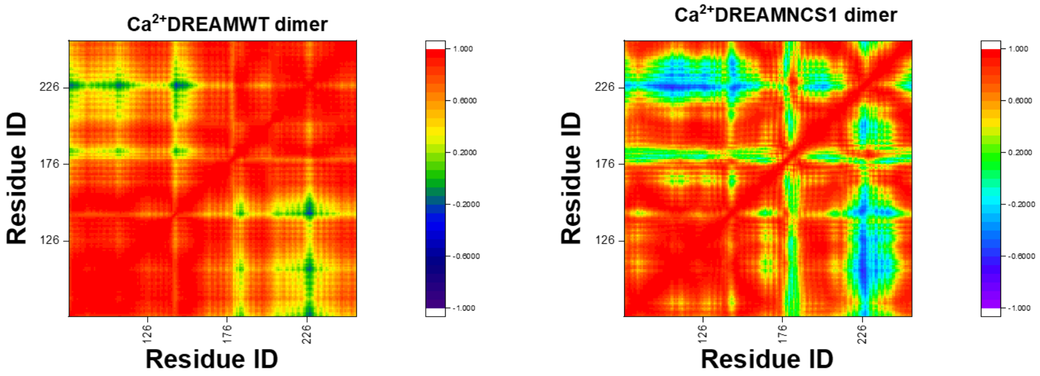

Figure 4.13: Dynamic cross correlation analysis for the monomers corresponding to DREAMWT dimer (left) and DREAMNCS1 dimer (right) in the presence of Ca^{2+}.

4.3 Discussion

The kinetics studies of Ca^{2+} association to DREAM WT suggest that the binding of Ca^{2+} to the protein can be described as a two-step process. The first step is characterized with the increase in the Trp emission and occurs on the millisecond time scale in both, DREAMWT and the DREAM-NCS1, with τ values of 8 ± ms and 13 ± ms, respectively and we attribute this process with Ca2+ association to EF -hands. In both constructs, the k_{1obs} decreases with the increase in the Ca^{2+} concentration, suggesting that Ca^{2+} binding process to apoDREAM and apoDREAM-NCS1 can be described by a conformational selection mechanism. Based on the values of the rate constant, the equilibrium constant for conversion of P* conformation to P conformation was calculated to be 0.49 and 0.28 for DREAMWT and DREAM-NCS1, indicating that at equilibrium, a major fraction of DREAMWT and DREAM-NCS1, 67% and 78%, respectively, is in the non-binding, P*, conformation. To our knowledge, this is the first time when the mechanism of Ca^{2+} binding to DREAM or any neuronal calcium sensor protein has been described and associated kinetic parameters determined experimentally. The rate constants for Ca^{2+} release from Ca^{2+}DREAM and Ca^{2+}DREAM-NCS1 are similar, 112 s^{-1} and 180 s^{-1} and are comparable with the k_{off} values determined for Ca^{2+} dissociation from other Ca^{2+} sensor, calmodulin, $k_{off} = 10.7\ s^{-1}$, suggesting that the affinity for Ca^{2+} is controlled by modulating the k_{on} values (Sibarov & Antonov, 2018)

Interestingly, in case of DREAM-WT, the initial increase in the Trp emission is followed by the decrease in the emission that occurs with the time constant of 3.6 s. The rate of this phase is independent of Ca^{2+} concentration and likely represents either formational of the DREAMWT dimer or a conformational relaxation that precedes the dimer formation. Indeed, this phase disappear in the presence of the high concentration of NaCl, suggesting that dimer formation or the conformational relaxation involves formational of the salt bridges, being consistent with the formation of the dimer protein. The plot of the k_{2obs} as a function of the DREAMWT concentration does not demonstrate a strong dependence on the protein concentration or the k_{2obs} values seems to decrease at increasing protein concentration. However, the range of DREAMWT concentration is relatively narrow to demonstrate a trend. It is also possible, that increase in apo DREAM concentration promotes formation of apoDREAM tetramer, results in the lower concertation of apoDREAM monomer. The attribution of the slow kinetic phase to the formation of dimer or conformational relaxation that is necessary for dimer formation is supported by the kinetic and time resolved anisotropy data on DREAM-NCS1 construct that does not form a dimeric structure in the solution as shown in time resolved anisotropy study. The slow kinetic phase has significantly lower amplitude and more importantly is associated with the Trp emission increase, pointing towards distinct structural changes in this protein that do not lead to the formation of the dimer. In addition, the absence of dimeric structure for Ca^{2+}DREAM-NICS1 construct confirm that hydrophobic interactions between Leu residues Leu residues 155,158, 159 and 251 as well as the salt bridges formation between residues Arg 200, Arg 207 and Glu 103 are necessary for the stability of DREAM dimer. Overall, determining the presence of the conformational selection mechanism is a crucial step to gaining more insight on how Ca^{2+} regulates the processes in which DREAM and other CBP are involved.

5. ROLE OF TRP169 IN THE ALLOSTERIC REGULATION OF NEURONAL CALCIUM SENSOR DREAM

5.1 Introduction

Allosteric processes occur when the binding of a ligand to a site of a protein produces a change at one remote site affecting the protein's function (Greener & Sternberg, 2018). The initial change at the allosteric site could occur through covalent binding, non-covalent biding of a ligand or through light absorption (Greener & Sternberg, 2018). Several effects are regulated by allosteric sites such as changes in catalytic activity, ligand affinity, and oligomerization state (Greener & Sternberg, 2018). The mechanism of allosteric control has been intensively studied since the mid 1960's and the concepts and views on allostery have evolved with the increasing use of computational methods which have provided a more detailed information of the allosteric changes at a molecular level (Cui & Karplus, 2008). It is currently believed that the changes from the allosteric site to the active site are transmitted by small conformational changes through networks of residues in the protein· (Cui & Karplus, 2008; del Sol et al., 2009) which have been found to be conserved throughout evolution (Clarke et al., 2016). Hence, the study of allosteric sites, allosteric modulators, and networks of residues involved in transmitting the changes across the protein is crucial to understanding allosteric mechanisms.

Previous studies of the allosteric communication between Ca^{2+} binding sites and target interfaces for NCS1, recoverin, and GCAP1 has been performed by Marino et al. using molecular dynamics simulations. In addition, protein structural network studies (PSN) have revealed hydrophobic interdomain interactions between the Ca^{2+} binding sites and the target recognition areas. For instance, key conserved amino acids such as residue Tyr86, which is involved in the hydrophobic packing in the N- terminal of recoverin, was determined to be involved in interdomain communication with EFH3 (Marino & Dell'Orco, 2019) . Furthermore, through multiple sequence alignment GCAP 1, NCS1 and recoverin were found to have four identical hubs, including the first and the last amino acids of the Ca^{2+-}binding loops of EFH 2 and EFH 3, involved in signal transmission from the N- to C- terminal (Marino & Dell'Orco, 2019).

Brüschweiler *et.al* also observed hydrophobic amino acid networks in calcium binding proteins (CBP). The KIX domain of the transcriptional CREB binding protein was determined to be crucial in the allosteric communication mediating the interactions among transcription factors through a dynamic repacking of the hydrophobic core of the protein (Brüschweiler et al., 2013)

Previous studies have shown that Ca^{2+} binding to the C- terminal domain of DREAM modulates the affinity of the N- terminal domain for intracellular partners such as site 2 of the T1 domain of K_v channel and DNA (Figure 5.1) (Findeisen et al., 2006; Masanori Osawa et al., 2005) . In addition, changes in the N-terminal domain were observed upon Ca^{2+} binding to the C-terminal domain through HDX-MS studies (Zhang et al., 2017)

DREAM affinity for various intracellular targets is regulated by association of divalent metals such as Ca^{2+} and Mg^{2+} to the EF-hands (Choi et al., 2003; Masanori Osawa et al., 2005) , changes in DREAM oligomerization state (Masanori Osawa et al., 2001), and posttranslational modifications in the N- terminal extension (Choi et al., 2003). The mechanism of how Ca^{2+} regulates DREAM interactions with intracellular targets, as well as the communication between Ca^{2+} binding EF-hands in the C-terminal domain and sites for Kv$_4$ potassium channel and DRE sequence in the N-terminal domain remains unknown.

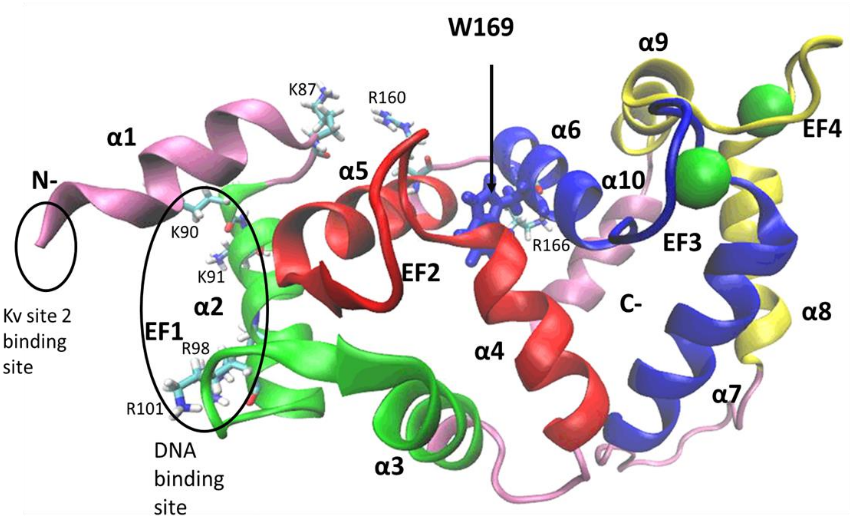

Figure 5.1: Structure of Ca^{2+}DREAMWT (PDB entry 2JUL) showing EF hands 1-4 in green, red, blue and yellow respectively; and proposed binding site for DNA and site 2 of the K$_v$ channel. Ca^{2+} ions shown as green spheres.

Based on the similarity among calcium binding proteins, the high sequence similarity among the subfamily of NCS (Figure 5.2) , and the fact that the binding of calcium triggers conformational changes required for target recognition, it is proposed that the amino acids involved in the interdomain hydrophobic network have a crucial role in transmitting the allosteric signal between N- and C terminal.

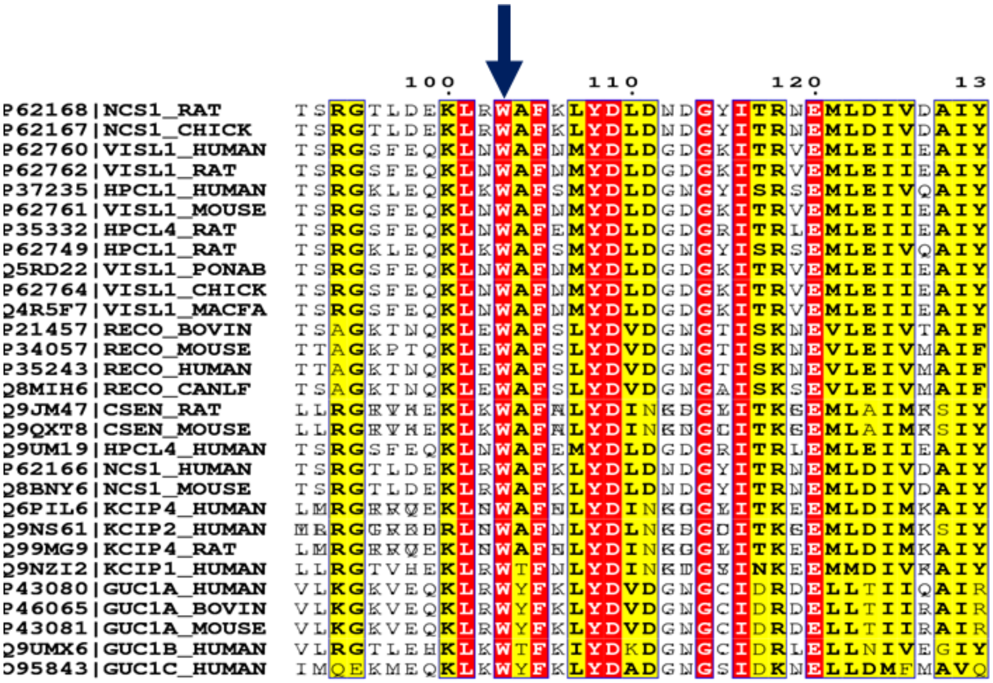

Figure 5.3: Sequence alignment of over 25 members of the different five subgroups in the NCS family, showing the Trp residue conservation throughout the protein family.

A network of hydrophobic amino acids connecting the N- and C- terminals has been identified using MD simulations of the Ca^{2+}DREAM and apoDREAM structures (Gonzalez, 2014). This network involves residues: W169, F171, Y174, F218, F219, and F235; and it has been proposed to participate in the inter-domain allosteric communication (Gonzalez, 2014) since the orientation of the F235 sidechain is sensitive to the presence of Ca^{2+} in EF-hand 3 and 4, suggesting that hydrophobic residues may serve as a molecular switch between the apo and the Ca^{2+} bound state (Figure5.3).

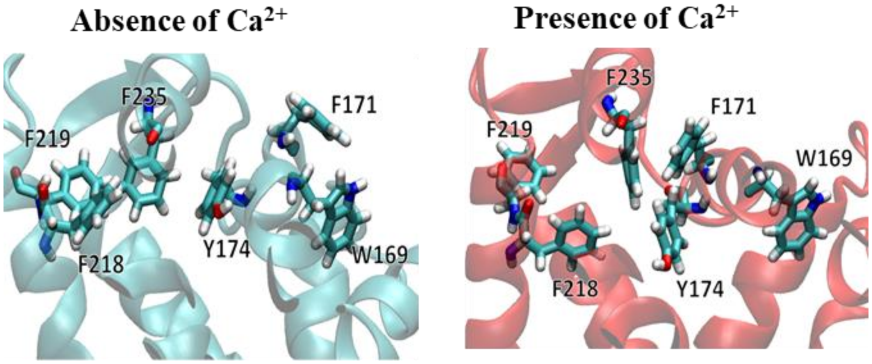
Absence of Ca^{2+}

Presence of Ca^{2+}

Figure 5.3: The network of hydrophobic residues in the C- terminal that couples EFH 3 and 4 with the Trp 169 in the N- terminal.(Gonzalez, 2014) .

Among the hydrophobic residues listed in the sequence alignment in Fig 5.2, the Trp residue is highly conserved among members of the NCS family. Its sidechain is located in the interface between the N- and C- terminal domain and thus it is strategically positioned to enable inter-domain interactions.

In this study, we have mutated residue Trp169 to Ala using the previously determined DREAM structure (PDB entry *2JUL*) in order to elucidate the role of this amino acid in the hydrophobic network and the transmission of the allostery for the monomeric and dimeric forms of the protein. Classical molecular dynamics and accelerated Gaussian molecular dynamics were performed for the mutant in the presence and absence of Ca^{2+} to assess the impact of this residue on protein structure and dynamics.

5.2.Results

5.2.1.Identification of the Trp169 in allosteric pathways

The allosteric pathways identification programs Protein Allosteric and Regulatory Sites (PARS) and Residue Interaction Network Generator (RING) have been used to identify allosteric pathways in the Ca^{2+}bound DREAM structure. Using previous molecular dynamics data for Ca^{2+}DREAMWT, 15 frames were randomly selected throughout the simulation and the pdb files were input in the PARS server to identify allosteric networks of amino acids. The PARS software analyzes the protein structure and predicts allosteric and regulatory sites based on structural conservation of individual residues and their potential to affect the flexibility of the protein. After analysis, the PARS software provides a ranked list of cavities, as well as the residues found in each cavity. When analyzing the number of cavities obtained per structure and the frequency at which a specific amino acid appears, Trp169 was identified as the amino acid present with the highest frequency in all analyzed frames (Fig 5.4). Thus, Trp169, was identified as having the highest probability to be involved in the allosteric pathway.

Furthermore, the Trp169 residue was also identified by the RING web tool as being part of the interdomain communication network through π-π stacking interactions with residues F138 and F171 in Ca^{2+}DREAMWT (PDB entry 2JUL) (Figure 5.5). Unlike PARS, RING protein network analysis tool identifies non-covalent interactions at the atomic level in a protein structure.

With the goal of investigating the role of Trp residue in the hydrophobic network of amino acids involved in interdomain communication in DREAM, molecular dynamics simulations have been carried out. The available DREAM NMR structure in the PDB bank (PDB ID 2JUL) has been used incorporating the mutation of the Trp169 residue to Ala (DREAMW169A) in the presence and absence of Ca^{2+}.

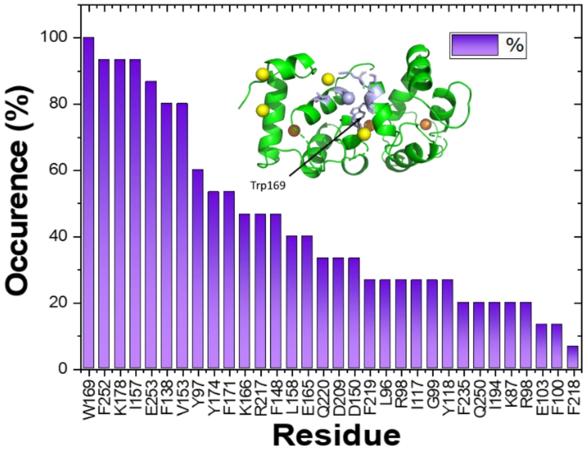

Figure 5.4: Percent occurrence for allosteric residues identified by the PARS software using 15 independent randomly selected frames from 100 ns aMD simulation of DREAMWT in the presence of Ca^{2+}.

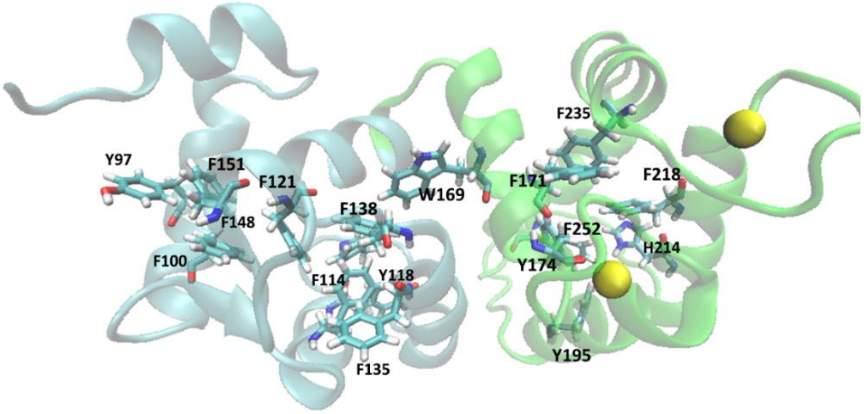

Figure 5.5:Trp 169 residue in DREAMWT PDB ID 2JUL (left) as a part of the π-π stacking interaction among the hydrophobic networks connecting N- and C- terminals.

5.2.2 Classical Molecular dynamics (cMD) studies

Classical MD (cMD) simulations of 600 ns and 500 ns cMD were performed on the DREAMW169A structure in the presence of Ca^{2+} and absence of Ca^{2+}. The RMSD plot shows that the Ca^{2+} bound structure reached equilibrium at around 50 ns, whereas the apo structure exhibited more differences when compared to the initial structure and started to stabilize around 150 ns (Fig 5.6). The DREAMW169 structures taken from the final frames of the simulation were aligned with the previously obtained structures (Gonzalez ,2014) in the presence and absence of Ca^{2+}(Figure 5.6). For the Ca^{2+}bound structure, alpha helices located in EFH 3 and 4 showed a relatively small shift whereas the EFH1 exhibited the greatest structural difference when compared to the WT with an RMSD of 3.35 Å. For the structures obtained in the absence of Ca^{2+} , an RMSD of 3.2 Å was obtained, the EFH 3 and 4 showed relatively small shifts when comparing the mutants to the WT, while the EFH 1 and 2 showed the greatest shift of the helixes but not as significative as the differences observed in the presence of Ca^{2+}, suggesting the role of W169 in the interdomain communication upon Ca^{2+} binding.

5.2.3 Gaussian accelerated molecular dynamic (GaMD) studies

Additional simulations were performed using the Gaussian accelerated molecular dynamics (GaMD) approach for DREAMW169A (PDB ID 2JUL) in the presence of Ca^{2+}, apoDREAMW169A using a previoously obtained 100 ns aMD apoDREAMWT structure(Gonzalez,2014) , and the DREAMW169A (PDB ID 2JUL) with the Ca^{2+}ions removed from the structure. This approach provides an energy boost to the structures following a Gaussian distribution, and it allows to observed structural changes equivalent to the ones observed at a microsecond scale. All three simulations resulted in stable structures as evidenced by the RMSD plots (Fig 5.7).

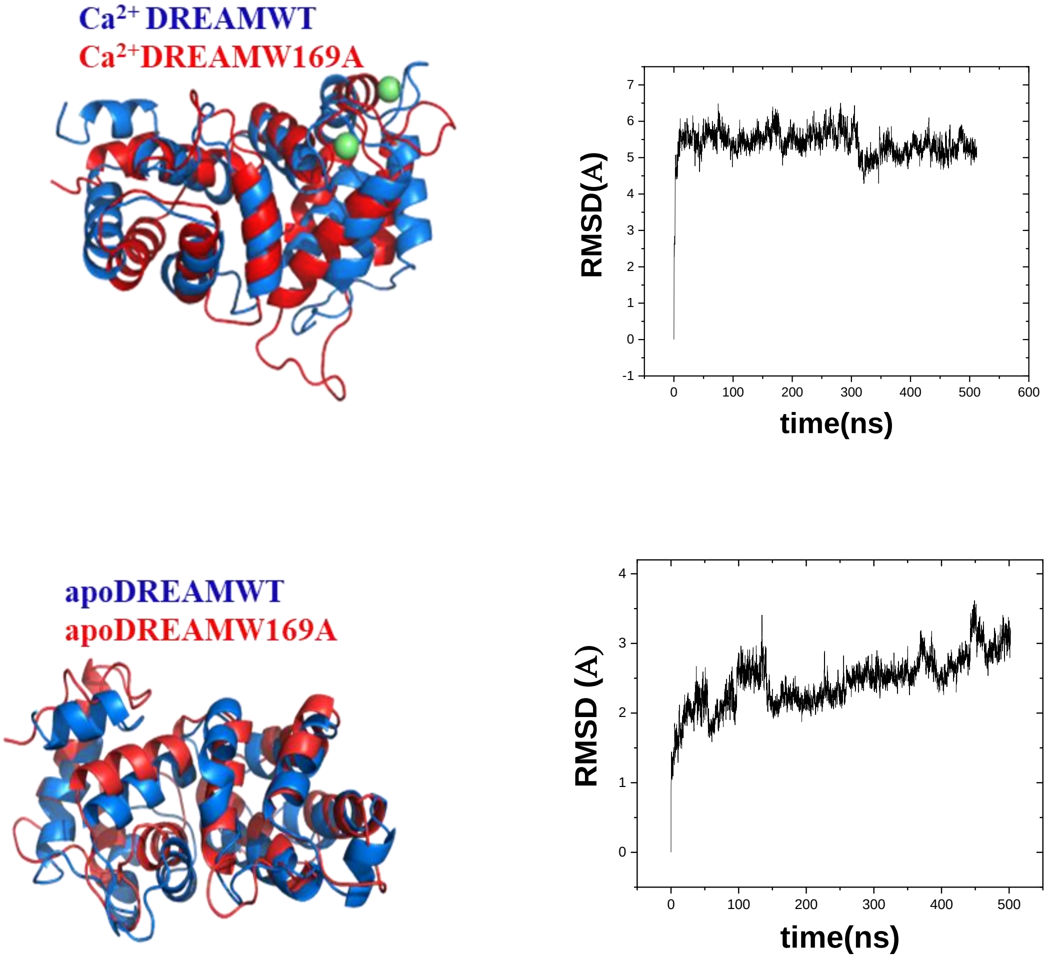

Figure 5.6: Structural alignment of DREAMW169(red) and DREAMWT (blue) in the presence (top left panel) and absence of Ca^{2+} (bottom left panel). Root mean square deviation for Ca^{2+}DREAMW169A cMD (top right) and apoDREAMW169cMD (bottom right) as a function of simulation time.

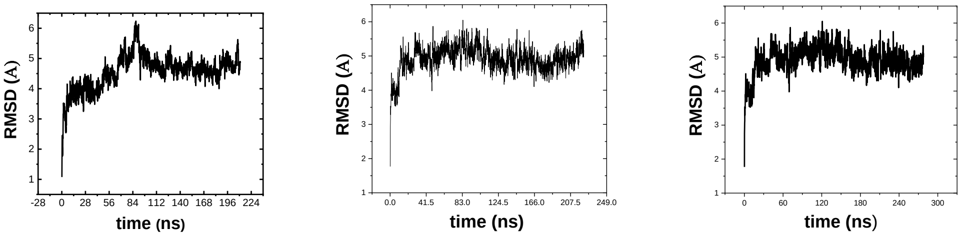

Figure 5.7: GaMD RMSD graphs for DREAMW169A in the presence of Ca^{2+}(left),apoDREAMW169 (center), and the DREAMW169A with the Ca^{2+} ions removed from the structure (right) .

5.2.4 Root mean square fluctuations values

In addition, Cα root mean square fluctuations (RMSF) were calculated. The plot of the RMSF for each residue obtained from the DREAMW169A simulations show less dynamic structures in general when compared to the RMSF values obtained from the DREAMWT simulations (Figure 5.8). In the presence of Ca^{2+}, the main difference is observed for the loop connecting EFH 1 and 2, which shows lower RMSF values with a 2 Å^2 difference for the W169A mutants when compared to the ones obtained for Ca^{2+}DREAWT structure. This difference in fluctuation of the loop connecting EFH 1 and 2 suggest that the absence of the indole sidechain in the position 169 affects the flexibility of the N- terminus for the DREAMW169A structure. The RMSF values for the simulations performed in the absence of Ca^{2+} showed to a smaller extent a similar pattern of lower flexibility for the area corresponding to the loop connecting EFH 1 and 2 when compared to DREAMWT.

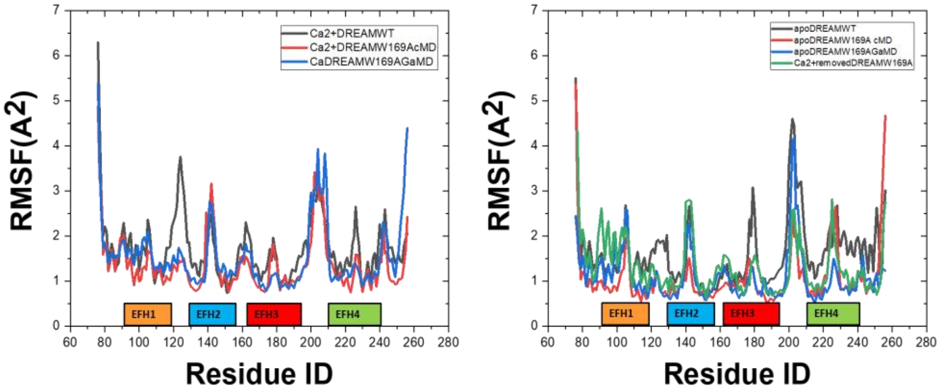

Figure 5.8: Root mean square fluctuations obtained from the simulations performed for DREAMWT and DREAMW169A in the presence (left panel) and absence of Ca^{2+} (right panel)

5.2.5 Reorientation of helices in EF hands

The EF hands for the structures obtained from the DREAMW169A simulations in the presence and absence of Ca^{2+} were individually aligned using the first 12 amino acids in order to observe the effect of the mutation in each EFH reorientation . Based on the DREAMWT simulations (Gonzalez, 2014), a reorientation of the EFH1 occurs upon Ca^{2+} binding in EFH3 and EFH4 seen in Fig 5.9 (left panel). Interestingly, EFH1 shows the most pronounced change in the alpha helical angle even though the binding of Ca^{2+} is produced in EF 3 and 4, indicating the role of Ca^{2+}as an allosteric modulator of the N- terminal domain and suggesting transmission of a signal from the C- to N- terminal. When analyzing the effect of the Trp 169 mutation in the presence and absence of Ca^{2+} for the reorientation of the EF hands (right panel) , a much smaller reorientation is observed for EFH1 in the mutant when compared to the wild type, whereas for EFH 2, 3 and 4, reorientation was similar for the mutant and wild type. This suggests that the replacement of the Trp disrupts the transmission of the signal from the C- to N- terminal causing the EFH1 reorientation previously seen in the WT not to be produced for the mutant.

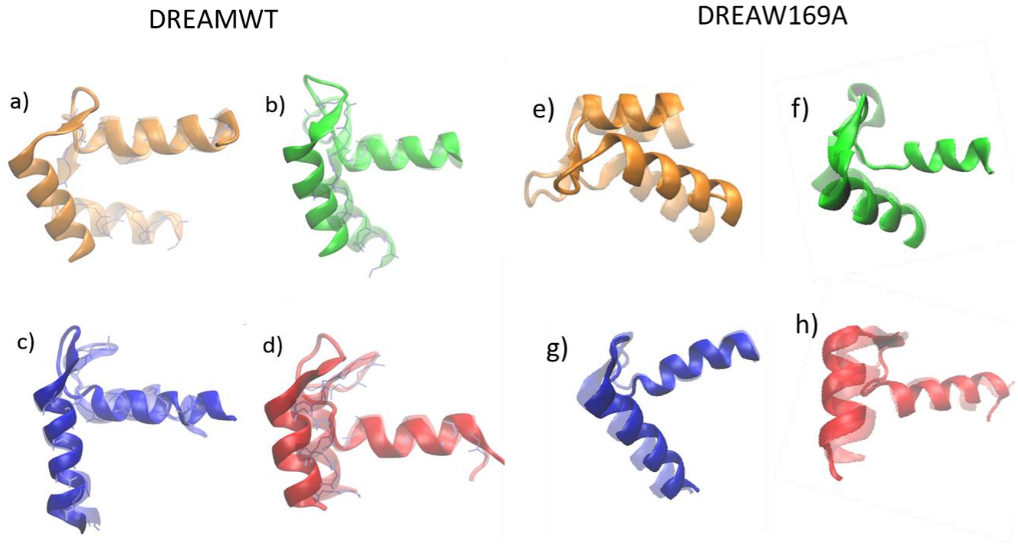

Figure 5.9: Reorientation of the EF-hands of DREAM in the presence of Ca^{2+} (shown in solid colors) and in the absence of Ca^{2+} simulation (shown in diffuse color). Alignments were done using the first 12 amino acids of the entering helix, EFH1 shown in orange, EFH2 shown in green, EFH3 shown in blue and EFH4 shown in red.

5.2.6 Analysis of the presence of salt bridges

The presence of the salt bridges stabilizing the protein structure was analyzed for DREAMW169A and compared to the salt bridges found in DREAMWT in the presence and absence of calcium for cMD and GaMD simulations. Interestingly, the structure stabilizing salt bridge between Glu165 and Lys 87, which is present in the Ca^{2+}DREAMWT and apo DREAMWT structures and connects the N- and C- terminal, was disrupted in the DREAMW169A simulations in the presence and absence of Ca^{2+}. As seen in Figure 5.10, the distance between Lys87 and Glu165 for the mutant exceeds the

12 Å during the simulation as opposed to the WT in which the salt bridge is formed around 20 ns and remains stable throughout the simulation

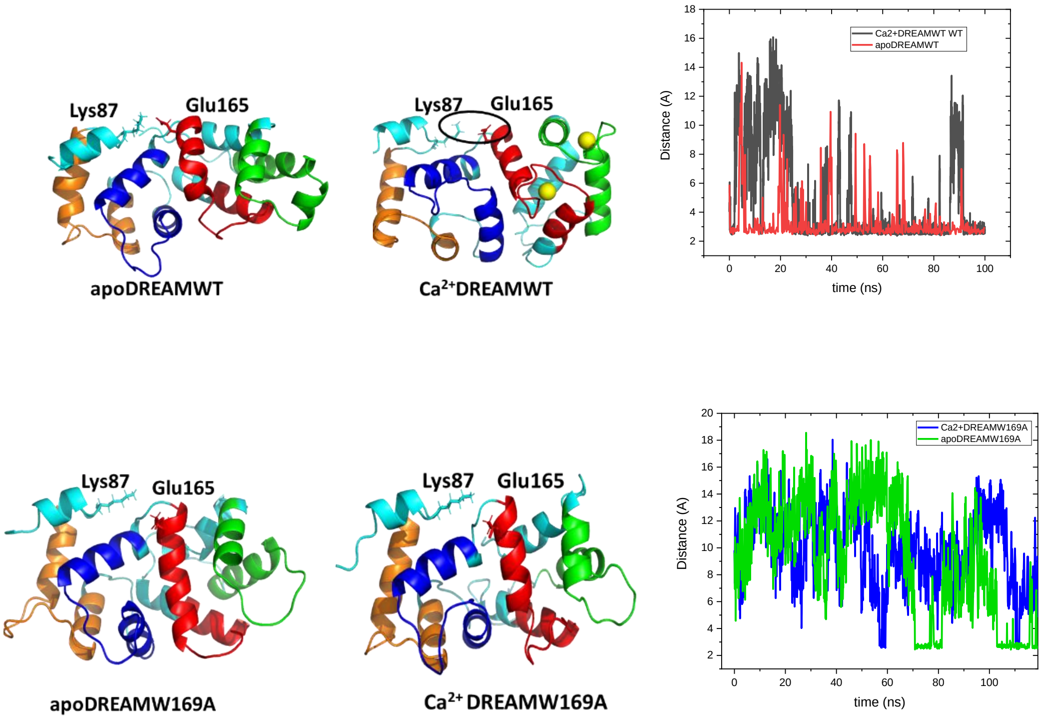

Figure 5.10: Salt bridge between Lys87 and Glu165 present in apoDREAMWT(top left panel) and Ca^{2+}DREAMWT(top middle panel) and amino acids from the disrupted salt bridge for apoDREAMW169A (bottom left panel) and Ca^{2+}DREAMW169A (bottom middle panel) . Distance against simulation time for Ca^{2+}DREAMWT (black) and apo DEAM WT(red) showing the formation of the Lys87-Glu165 salt bridge(top right panel) and Ca^{2+}DREANW169A (blue) and apoDREAMW169A(green) showing the absence of the salt bridge in the mutant(bottom right panel) .

As seen in Figure 5.10 the side chain of the Glu165 is oriented towards the center of the hydrophobic cavity of the protein in the W169A mutant when compared to the WT version m preventing the salt bridge to form. When looking at the sidechains that are located withing 5 A of the Trp169 and Ala169 (Figure 5.11) , it is observed that the Glu 165 side chain is occupying part of the hydrophobic cavity in the case of the mutant. This observed repositioning of the Glu165 indicates this is the reason why the salt bridge was not formed when the Trp was mutated to Ala causing the lack of the formation of the structure stabilizing salt bridge.

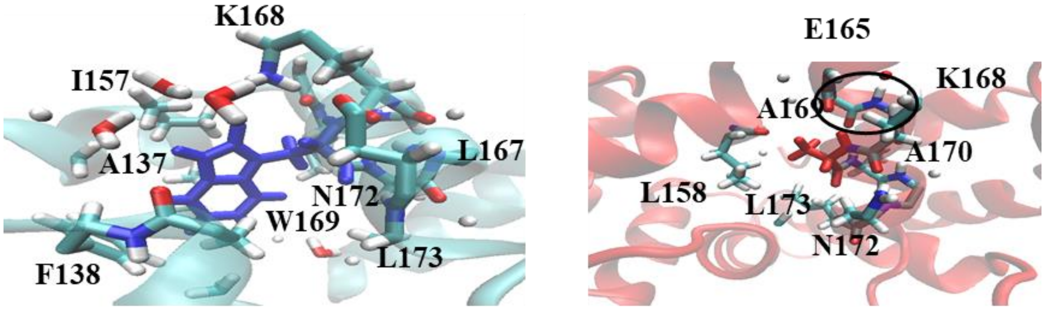

Figure 5.11: Contact residues found within 5 Å of the Trp169 side chain for Ca^{2+}DREAMWT located in the hydrophobic cavity connecting N- and C- terminals(left panel). Contact residues found within 5 Å of the Ala169 side chain for Ca^{2+}DREAMW169A showing the presence of the Glu165 residue in the hydrophobic cavity, hence not forming the structure stabilizing salt bridge with Lys87(bottom left panel).

Furthermore, salt bridges connecting Glu92-Arg 160 (connects EFH 1 and 2) and Lys166-Glu253 (connects EFH3 and Helix 10) were maintained for both the wild type and the mutants in the presence and absence of Ca^{2+}, suggesting that Trp replacement did not affect the interactions for this structure stabilizing salt bridges.

5.2.7 Analysis of the presence of dynamic communities of amino acids

In addition, the dynamic cross correlation maps of the alpha carbons between amino acids during specific simulation time were analyzed for the DREAMWT and for DREAMW169A in the presence and absence of Ca^{2+} using cMD and GaMD approaches. The cross-correlation analysis allows for monitoring the movement of the residues and identifying communities of amino acids with highly correlated dynamic movements. More negative correlation areas are observed in the apoDREAMW169AcMD when compared to the apoDREAMWT simulation, however the GaMD simulation show similar correlations as the apoDREAMWT, and it may be due to the fact the GaMD approach allows to see changes that would occur after longer periods of simulation . (Figure 5.12)

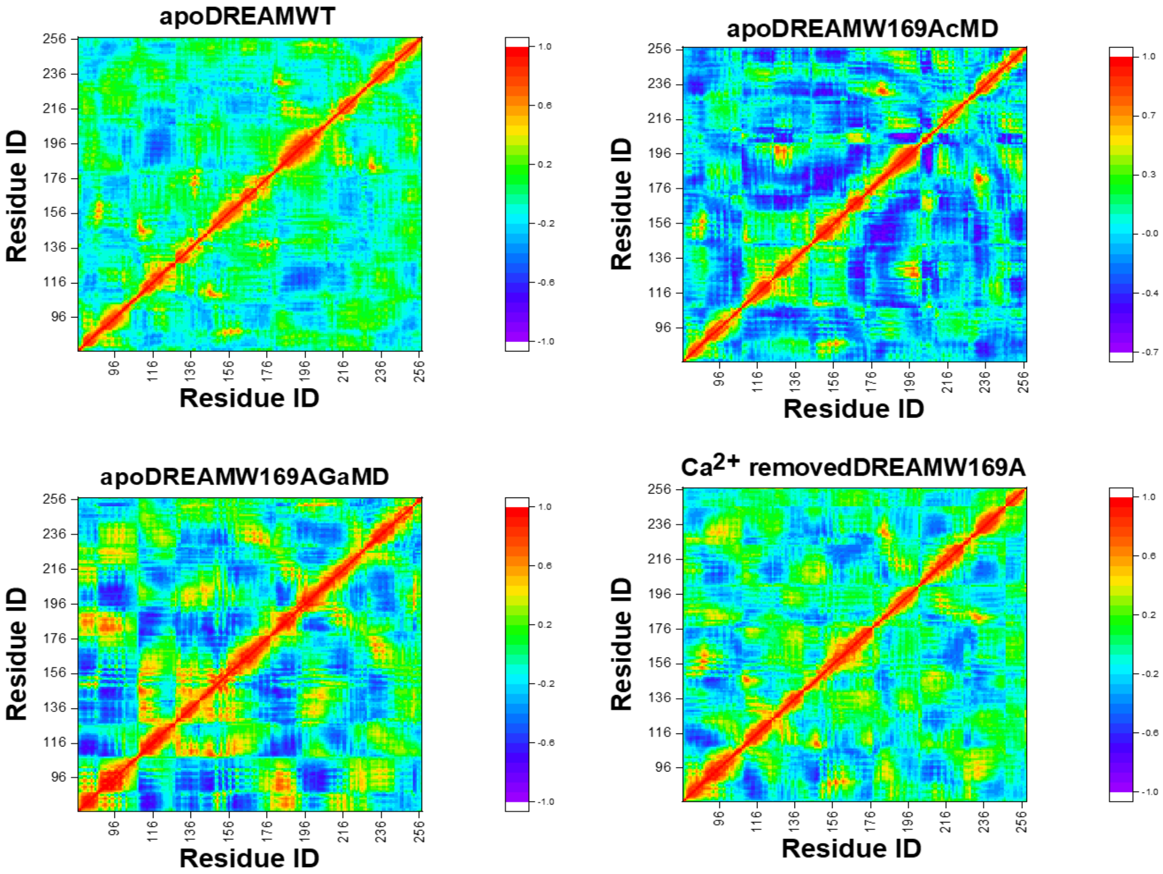

Figure 5.12: Dynamic cross correlation analysis for DREAMWT(top left panel), DREAMW169AcMD (top right panel) , DREAMW169AGaMD (bottom left panel) and Ca^{2+}removed structure DREAMW169A GaMD (bottom left panel) in the absence of Ca^{2+}.

In the case of Ca^{2+}DREAMW169A cMD, a strong negative correlation is observed for the area corresponding to amino acids 96 -1161 and 196-216 corresponding to EFH 1 and the loop between EFH 3 and 4 respectively , as opposed to the Ca^{2+}DREAMWT, indicating a different dynamic of the amino acids for the mutant and the wild type simulations. In addition, for the Ca^{2+}DREAMW169A GaMD, these negative correlations are not as pronounce but a greater negative correlation are still observed for these areas of the protein.(Figure 5.13)

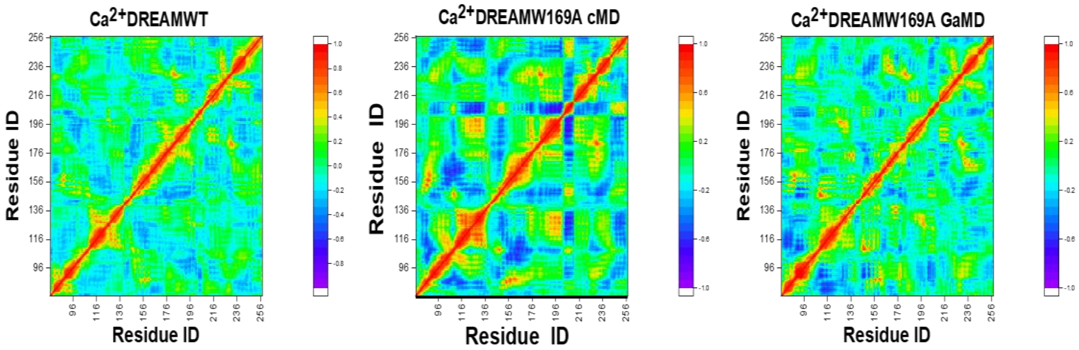

Figure 5.13: Dynamic cross correlation analysis for DREAMWT (right panel), DREAMW169AcMD (middle panel) , DREAMW169AGaMD (left panel) in the presence of Ca^{2+}.

The communities identified by the dynamic cross- correlation maps provide information on how connected the residues are in the protein structure. The communities for the structure of DREAMWT in the presence and absence of Ca^{2+} were previously obtained in our group (Gonzalez, 2014). The apoDREAMWT showed networks of stronger and more dynamic connectivity between communities from the N- and C- terminals when compared to the Ca^{2+} DREAMWT, which shows a decrease in these connections separating the N- and C- terminals into two different areas with few connections among residues.

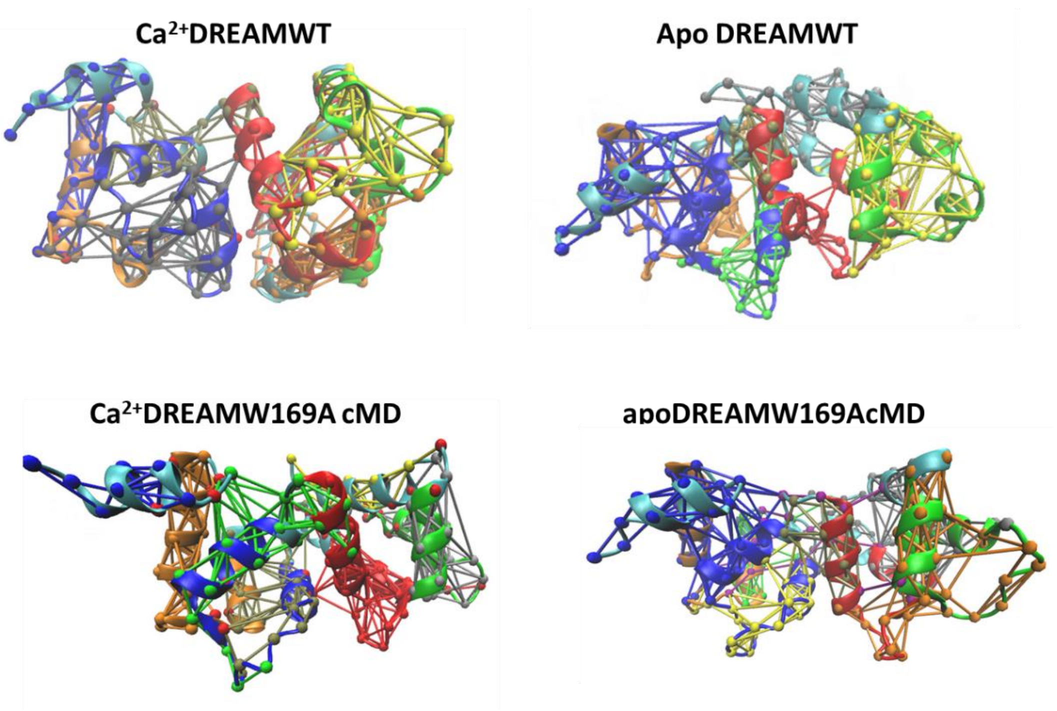

Figure 5.14: Colored communities identified in the structures for DREAMWT(top panel) and DREAMW169A (bottom panel) in the presence and absence of Ca^{2+} .

For the Ca^{2+}DREAMWT community analysis (Figure 5.14) ,one main greenish community in the N- terminal connects EFH1 and 2 with a few connections to EFH 3 and separate group of communities shown in yellow and orange interconnect EFH 3 and 4 in the C-terminal. The community analysis of the apoDREAMWT (Figure 5.14) data shows increased connectivity among the N- and C- terminals , namely the dark blue community connects EFH 1, 2 and 3, while the orange community connects EFH1 and 3 and a grey community in the C- terminal connects helix 10 with EFH3. These observations suggest that the binding of Ca^{2+} decreases the dynamic intercommunication of residues in the protein leading to a more disconnected N- and C- terminals.

When analyzing the apoDREAMW169A mutant (Figure 5.15), a similar connectivity as the apoDREAMWT was observed. The dark blue community connects EFH1, 2 and a critical node corresponding to Arg160 located in the cleft between N- and C- terminal interactions, while the yellow community connects EFH 1 and 3 as well the critical node Tyr 130 and Leu 173.

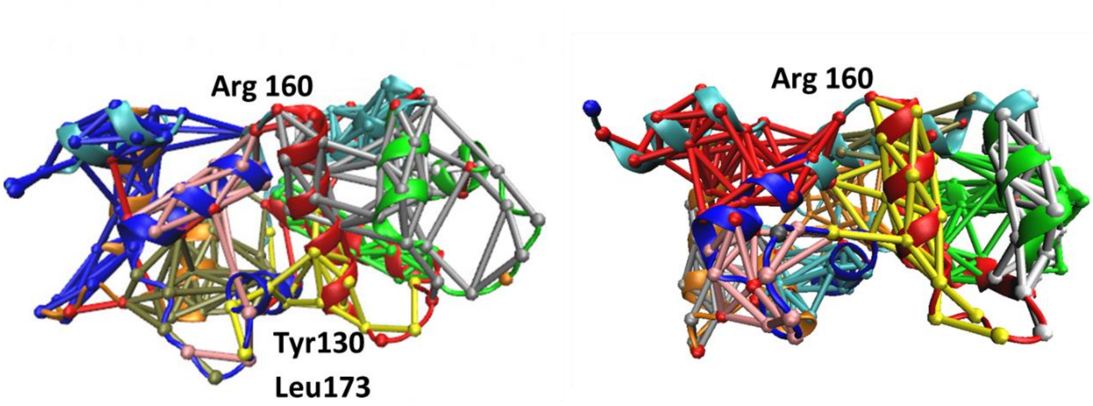

Figure 5.15: Colored communities for apoDREAMW169A. Dark blue community showing the contacts between EFH1, 2 and critical node Arg 160 and yellow community showing the connections among EFH 1 and 3 and the critical node Tyr 130 and Leu 173 (left). Colored communities for Ca^{2+}removed DREAMW169A. Red community connecting EFH1 and 2 and the critical node Arg 160 and yellow community connecting EFH 2, 3, the loop between EFH3, and 4.

For the Ca^{2+} removed DREAMW169A (Figure 5.15), a similar connectivity to the apo DREAMWT was observed as well. The red community connects EFH1 and 2 and the critical node Arg 160 previously observed in the apoDREAW169A, while a yellow community connecting EFH 2 and 3 and the loop between EFH3 and 4 is observed showing the interconnections between N- and C- terminals.

Interestingly, for the Ca^{2+}DREAW169A in both cMD and GaMD simulations, more dynamic networks and higher number of communities are observed when compared to the Ca^{2+}DREAMWT simulation.

For the Ca^{2+}DREAMW169A cMD (Fig 5.16) , two main interconnecting communities are observed. The green community is connecting EFH 1, 2 and 3, while the greenish community also connects EFH1, 2 and 3 and the critical node Phe133.

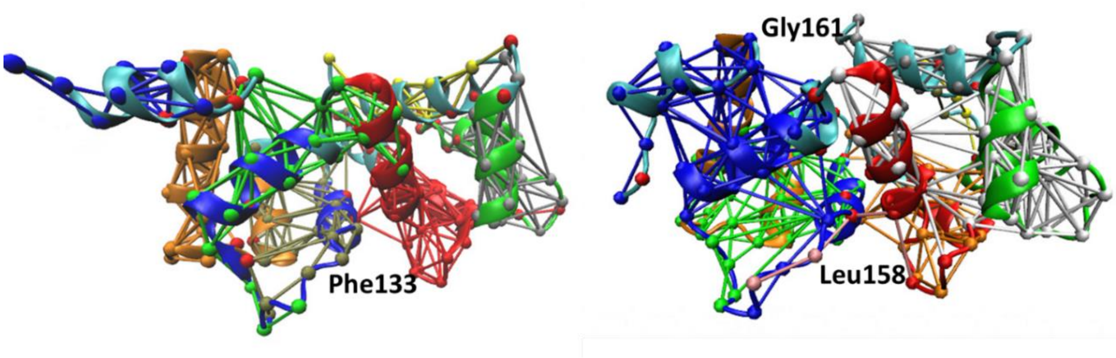

Figure 5.16: Colored communities for Ca^{2+}DREAMW169A cMD showing a higher connectivity among N- and C- terminal. Greenish community connecting EFH1, 2 and 3 and critical node Phe 133. Green community connecting EFH 1, 2 and 3. (left). Colored communities for Ca^{2+}DREAMW169A GaMD showing a higher connectivity among N- and C- terminal. Blue and communities connecting EFH1 and 2 and the critical nodes Gly161 and Leu 158, grey connecting EFH 3 and 4 and the critical node Gly 161 (right).

For the Ca^{2+}DREAMW169A GaMD (Fig 5.16), blue and green communities show networks connecting EFH1 and 2 and the critical nodes Gly161 and Leu 158, while the grey community connects EFH 3 and 4 and the critical node Gly 161 located among the N- and C- terminal.

The changes observed for the mutant, when compared to the WT, suggest that the Trp residue has a role in the signal transduction upon Ca^{2+}binding . This causes the Ca^{2+}bound mutant to show a network of communities that resemble the apo form for the WT , as evidenced by a more dynamic network connecting the N -and C- terminal seen in the Ca^{2+}DREAMW169A

5.2.8 Role of Trp169 mutation in dimerization

The experimental data shows that Ca^{2+} binding to apoDREAM promotes DREAM dimerization. The structure of the DREAM dimer is unknown, although Lusin *et al.* (Lusin et al., 2008). proposed that hydrophobic interactions between three Leu residues (Leu 155, Leu 158, and Leu 159) and Leu251 from the other monomer stabilize the dimeric structure. In addition, we have previously proposed that the dimeric form may also be stabilized through salt bridges residues Arg 200 and Arg 207 located in the loop connecting EFH 3 and EFH 4 and Glu 103 in the other monomer (Figure 5.17)

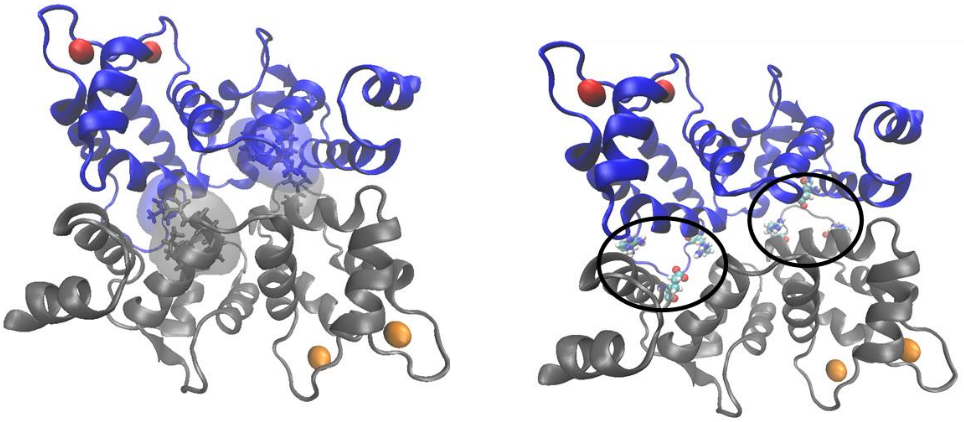

Figure 5.17: Model structure of DREAM dimer based on the NMR structure of DREM monomer (PDB entry 2JUL). Left panel shows hydrophobic interactions between Leu 155, 159 and 251 and right panel show a salt bridge between Arg 200, Arg 207 (in blue) and Glu 103 (in red) (Gonzalez, et al) .

In order to determine the role of the Trp residue in the dimeric interactions in DREAM, a mutant dimer structure was obtained through aligning the DREAMW169A monomers to the DREAMWT monomers in the model structure of the previously obtained DREAMWT dimer (Gonzalez 2014) and a 400 ns MD simulation was performed. The monomers interactions started to destabilize around 50 ns resulting in their complete separation around 80 ns. (Figure 5.18)

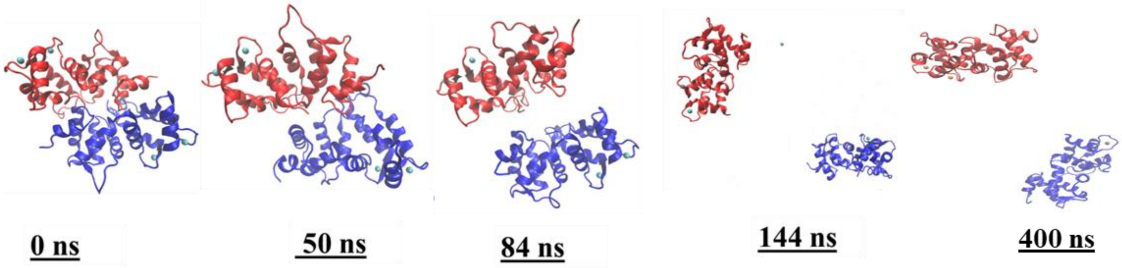

Figure 5.18: DREAMW169 dimer structure at 0, 50 , 84 ,114 and 400 ns simulation time. Each subunit is colored in red and blue, Ca^{2+} ions represented as cyan spheres.

When analyzing the residues involved in the stabilization of the dimeric interactions for DREAMWT such as the inter subunit salt bridge and the Leu motif, different conformations are observed for the mutant. For instance, in the case of the inter-subunit salt bridge among Glu 103, Arg 200 and Arg 207 for the DREAMW169A, the residues are further apart decreasing the possibility of formation of the salt bridge. In the case of the Leu motifs , the residues are reoriented opposite directions interacting with each other resulting in the absence of the hydrophobic cluster.(Figure 5.19)

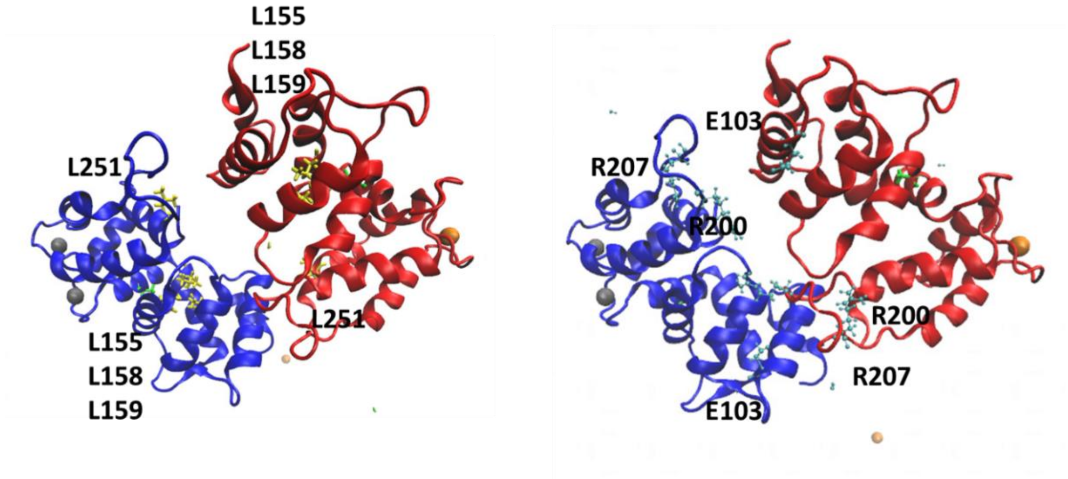

Figure 5.19: DREAMW169A dimer at 40ns cMD simulation. Leu 156, Leu 158 Leu 159 and Leu 251 residues (left). Salt bridge forming residues Glu 103, Arg 200 and Arg 207 (right) .

The dynamic cross correlation analysis for DREAMW169A dimer shows a decrease in positive and negative correlations when compared to the DREAMWT dimer. The residues in each subunit in the case of the WT either had a strong negative or positive correlation as evidenced in Figure 5.20 by highly predominant blue and red colors. However, in the DREAMW169A dimer, the correlation in the dynamics of the subunits is lost for residues comprising the N- and C- terminal , suggesting a more dynamic, less stable structure (Figure 5.20).

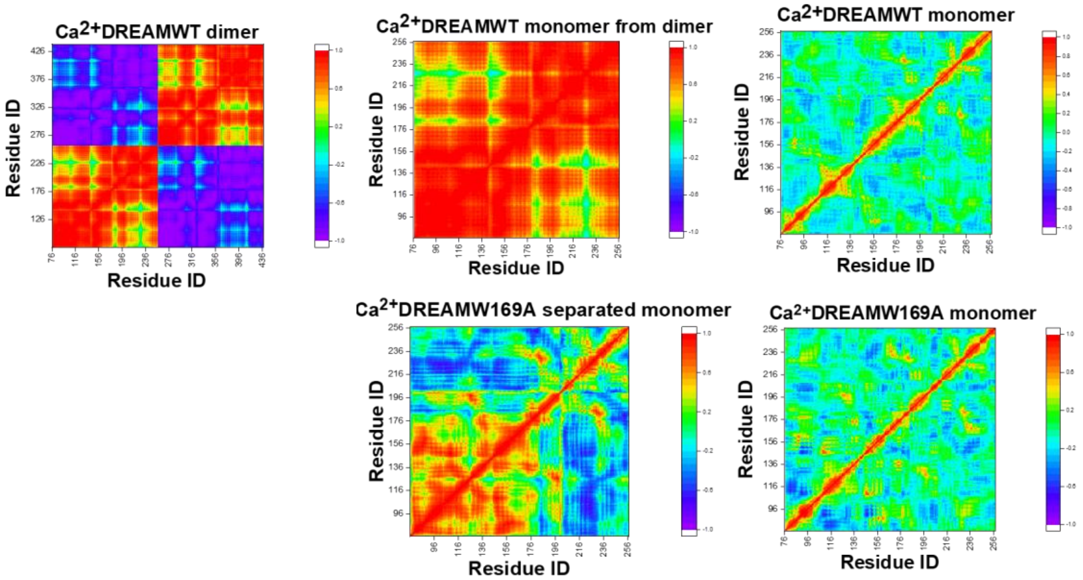

Figure 5.20: Dynamic cross correlation analysis for DREAMWT dimer (top left) and DREAMW169A dimer (right) in the presence of Ca^{2+} (top). Both monomers shown on top, monomer corresponding to subunit A shown at the bottom panel

In addition, an analysis of the solvent accessible surface area (SASA) was performed for the previously identified amino acids involved in the interactions that stabilize the DREAMWT dimer and compared to the accessible area of the DREAMW169A dimer (Fig 5.21). For amino acids Glu 103 and Arg 207, a decrease in the solvent accessible area of 100 $Å^2$ was observed for the mutant when compared to the WT, indicating that these residues were less exposed in the case of the mutant, hence disrupting the formation of the stabilizing inter-subunit salt bridge. For the Leu residues, in the case of Leu 158 and Leu 159, the solvent accessible area increased , while for the residues Leu 155 and Leu 251, a decrease of around 200 $Å^2$ was observed suggesting that these residues are more buried in the mutant and not contributing to the stabilizing effect previously seen in the WT.

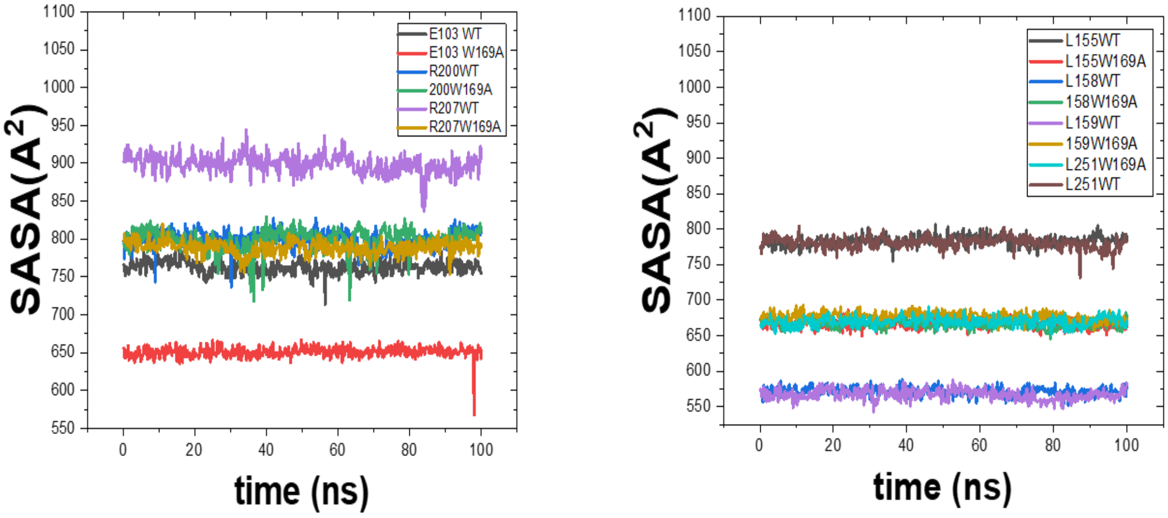

Figure 5.21: Comparison among Ca^{2+}DREAMWT and Ca^{2+}DREAMW169A for the solvent accessible surface area against simulation time for amino acids in the stabilizing salt bridge(left) for the Leu motifs (right) .

The differences observed between the DREAMWT dimer and the DREAMW169A dimer indicate that the substitution of the Trp 169 for Ala leads to a disruption in the signal transmitted through the previously identified hydrophobic network connecting the N- and C- terminal. This was evidenced by a decrease in the connections among communities connecting both subunits when compared to the WT dimer and the loss of the communities connecting the two monomers. In addition, a decrease in the solvent accessible surface area for the amino acids Arg 200, Arg 207 and Glu 103 and a decrease in the Leu motifs suggest that the stabilizing interactions between both monomers are diminished .

5.3 Discussion

The role of the Trp 169 residue located in the cleft among the N and C terminal in DREAM , and it is part of the hydrophobic networks of amino acids that are involved in the transmission of the interdomain allosteric signal, was investigated . The Trp169 was mutated to Ala in order to determines its impact in the interdomain communication . Molecular dynamic simulations were performed for the DREAMW169A mutant in the presence and absence of Ca^{2+} using classical and gaussian accelerated MD approaches. The structures in the presence and absence of Ca^{2+} were run for several hundreds of ns and the trajectories were analyzed and compared with the previous information obtained from the DREAMWT simulations in the absence and presence of Ca^{2+}. The loss of flexibility of the N- terminus in the presence of Ca^{2+} for DREAMW169A when compared to Ca^{2+}DREAMWT is evidenced by lower RMSF values for the loop connecting EFH1 and 2 , this suggest a disconnection in the transmission of the interdomain signal since for the WT the loop becomes more dynamic , in fact the binding of Ca^{2+} has been seen to modify the affinity of DREAM for intracellular partners such Site2 of the Kv4.3 channel and DNA. The previously identified important structure stabilizing salt bridge among Lys 87 located in the α1 and the Glu 165 located in the EFH 3 was not present in the DREAMW169A as evidence by the distance among these residues exceeding the 12 A , this suggests a destabilization in the overall structure of the mutant. The change in dynamics for the community networks analysis suggests the substitution of the Trp residue led to more connected interdomain contacts similar to the ones observed in the apoDREAMWT. For the Ca^{2+}DREAMWT community networks , it was previously observed that the dynamic communities were more individually located and did not show abundant connections between the N and C terminals, whereas Ca^{2+}DREAW169A showed greater interdomain connections indicating a more dynamic structure similar to the apoDREAMWT indicating the mutation lead to a change in the connections in the hydrophobic network. In addition, the MD studies performed for the mutated DREAMW169A dimer showed a loss of interactions among the monomers since the dimer separated into monomers at 80 ns in the simulation. This may be due to the fact that the solvent accessible area for the dimer stabilizing residues Arg 200, Arg 207, and Glu 103 and the Leu motif , Leu155,158 159 and 251 changed providing less availability for Leu residues to interact and different positioning for the residues involved in the dimer stabilizing salt bridge, did not contribute to the stability of the dimer . These results suggest the role of the Trp 169A residue in the overall stability of the protein and its participation in the interdomain communication while transmitting the allosteric signal in DREAM protein.

6. INTERACTIONS OF DREAM WITH DIVALENT ION ZINC

6.1 Introduction

Essential metals such as Zn^{2+}, Mg^{2+} and Ca^{2+} play extremely important roles in biological processes since they directly interact with proteins and are involve in several processes as co factors and regulators (Permyakov & Kretsinger, 2011) . Zinc is an essential metal, it is present in nearly all organs and tissues, and it is involved in several biological processes such as functioning of the immune system, regulation of apoptosis and the homeostasis of metal ions (Laity et al., 2001) (Plum et al., 2010). It is necessary for the normal development and functioning of the brain since it participates in neuronal growth and it has been found to be present in the hippocampus , and it presence is directly related to cognitive development in infants (Deshpande et al., 2013) (Vallee & Falchuk, 1993) (Plum et al., 2010). In addition, Zn^{2+} participates in cellular growth, wound recovery , reproduction and digestive system and endocrine processes. (Deshpande et al., 2013)

The recommended Zn^{2+} intake is 1.4 mg and 1.0 mg a day for men and women respectively (*Trace elements in human nutrition and health*1996), however, many factors such as the iron intake can interfere with its absorption (Deshpande et al., 2013) The physiological free Zn^{2+} concentration has been determined to be within nm-pM range, whereas intracellularly it can be found in concentrations around the 100 pM (Plum et al., 2010). Due the Zn^{2+} versatility in such variety of processes , regulating its concentration is essential for maintaining the proper functioning of theses physiological processes. (Plum et al., 2010)

It is commonly known nowadays that Zn^{2+} deficiency can affect human health since it produces immune system dysfunctions, infertility , skin lesions, growth retardation, reproductive disorders and it has been linked to carcinogenesis (Deshpande et al., 2013; Kido et al., 2022) (Plum et al., 2010). There are neurological consequences to Zn^{2+} deficiency such as mental lethargy, cognitive disorders , decrease in nerve conduction, and mental disorders (Deshpande et al., 2013; Plum et al., 2010). These effects are more likely to be seeing in children and adolescent woman since their Zn^{2+} requirement is greater than the rest of the population , or in patients with absorption pathologies such as renal diseases, Crohn's disease, or diabetes. (Deshpande et al., 2013)

On the other hand, the excess of Zn^{2+}also produces serious negative health effects such alteration in the lymphocyte function, increased risk of prostate cancer, gastrointestinal disorders, altered cholesterols levels and copper and iron deficiency (Deshpande et al., 2013; Hooper, 1980; Plum et al., 2010). Furthermore, Zn^{2+} neurotoxicity is associated with lethargy, headaches ,focal neuronal deficits and during ischemic conditions facilitates apoptosis in neurons (Inoue et al., 2010; Plum et al., 2010)

Zn^{2+} is able to interact with nearly 300 enzymes in the body and it is involved their metabolic activity (Deshpande et al., 2013)(Vallee & Falchuk, 1993) (Plum et al., 2010) .The discovery of Zn^{2+} fingers determined the importance of Zn^{2+} for protein structure, protein organization and protein interactions with other proteins and molecules such as DNA, RNA, and lipids (Maret, 2012). Zn^{2+} fingers were discovered by determining potential Zn^{2+-}binding ligands with specific motifs including Cys2His2 in the sequences where Zn^{2+} would bind (Laity et al., 2001; Maret & Li, 2009; Maret, 2012)

This characteristic motif was used to find Zn^{2+} proteins by searching databases for protein sequences and resulted in determining there are about 3000 Zn^{2+} binding proteins in humans alone. (Maret & Li, 2009; Maret, 2012)

It has been seen that the nitrogen from His, oxygens from Glu/Asp, and sulfur from Cys serve as donors for Zn^{2+} coordination, and while different coordination geometry have been observed, the most commonly found is a coordination of 4 with a tetrahedral geometry (Maret, 2012).

Previous studies have shown that Zn^{2+} is able to bind to Ca^{2+} sensor proteins such as S100 within the nm to mM range (Schaub & Heizmann, 2008) and calmodulin within the µM range (Baudier et al., 1983) (Permyakov & Kretsinger, 2011; Warren et al., 2007). The Zn^{2+} binding sites in proteins usually involve His Glu Asp and Cys residues. Previously published studies have determined that Zn^{2+} binds to two members of the neuronal calcium sensor family, such NCS1 and recoverin with affinities of 0.25 μM (Tsvetkov et al., 2018) and 7.0 μM (Permyakov, S. E. et al., 2003) respectively.

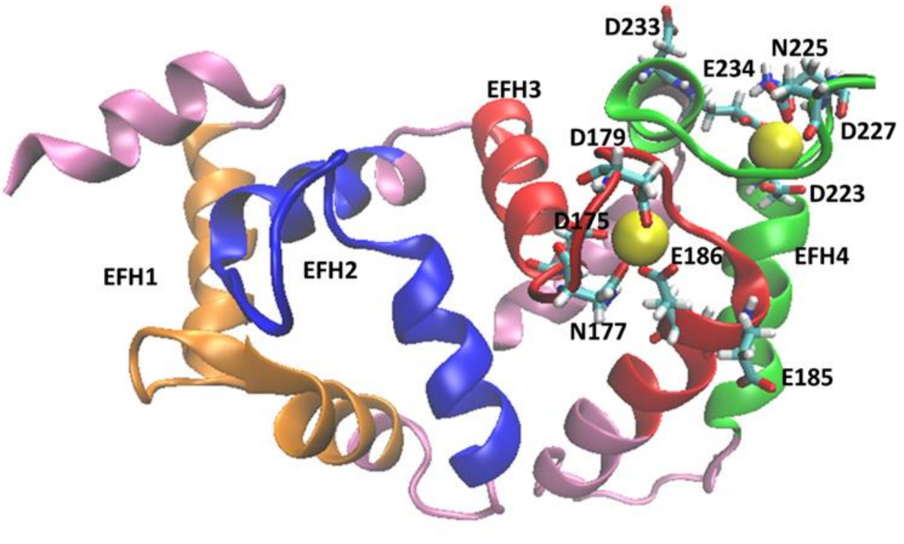

Figure 6.1: Ca^{2+}DREAM structure (PDB ID 2 JUL) showing EFH 1-4 in orange, blue, red and green, respectively . Amino acids involved in the binding of Ca^{2+} to EFH 3 and 4 are labeled and the Ca^{2+} ions are shown as yellow spheres. (Lusin et al., 2008)

DREAM protein has the ability to interact with several metals with relatively high affinity. It binds to Ca^{2+} at EFH 3 and 4 with a K_d of 1-10 µM and to Mg^{2+} at EFH2 with a K_d of 100-200 µM. However, only the Ca^{2+} DREAM structure has been previously determined through NMR studies by Lusin et al (Lusin et al., 2008) , PDB ID 2JUL. Ca^{2+} is coordinated through oxygen atoms from the side chains of residues Asp175, Asn177, Asp179, Glu 186 and Glu185 in EFH 3, and residues Asp223, Asn225,Glu 233 and Glu 234 at EFH4 (Lusin et al., 2008) (Figure 6.1) . Furthermore, DREAM has also been determined to bind to other metals such as Pb^{2+}, Cd^{2+} and Li^{+} , with relatively high affinity as evidenced by the K_d of 20 ± 2 nM for Pb^{2+} , 90±10 nM for Cd^{2+} and 34± 4 µM for Li^{+} (Azam et al., 2019; Azam & Miksovska, 2019b; Azam et al., 2020b) . Considering the fact that Zn^{2+} binds to other members of the NCS family such as recoverin and NCS1 and a high structural homology and sequence homology between the NCS family members (Figure 6.2 and 6.3), I proposed that DREAM can also serve as an intracellular target for $Zn^{2+.}$ Therefore, characterizing the Zn^{2+} binding properties of DREAM and how Zn^{2+} association affects its structure and interactions with effector protein, is crucial to understand the molecular mechanism of Zn^{2+} neurotoxicity and the role of neuronal calcium sensors in Zn^{2+} neuropathology. With this in mind, I have conducted fluorescence studies, circular dichroism studies and molecular dynamics analysis in order to elucidate Zn^{2+} binding to DREAM and its impact on protein structure.

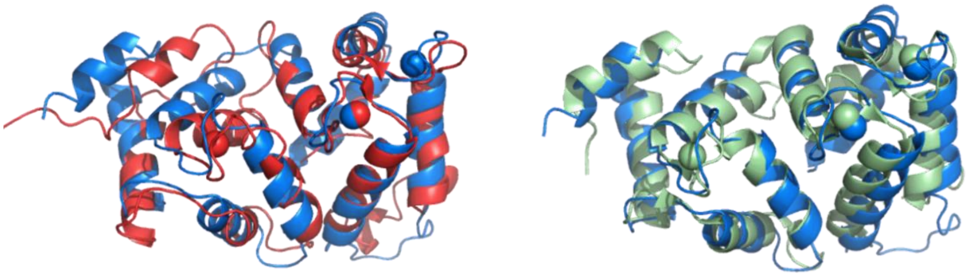

Figure 6.2: Structure alignment of DREAM (*PDB ID 2JUL*) shown in blue and recoverin (*PDB ID 1jsa*) shown in red (left panel) , and DREAM shown in blue and NCS1(PDB 4GUK) shown in green (right panel) demonstrating a high structural similarity between members of NCS family.

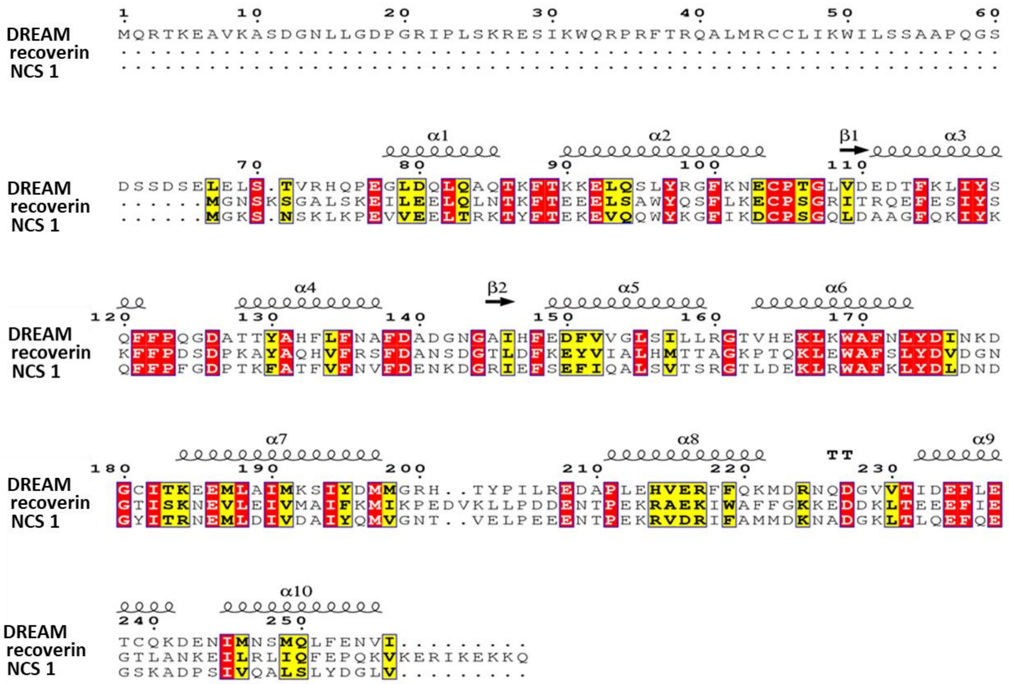

```
           1        10        20        30        40        50        60
DREAM      MQRTKEAVKASDGNLLGDPGRIPLSKRESIKWQRPRFTRQALMRCCLIKWILSSAAPQGS
recoverin  ............................................................
NCS 1      ............................................................

                 70        80        90       100       110
DREAM      DSSDSELELS.TVRHQPEGLDQLQAQTKFTKKELQSLYRGFKNECPTGLVDEDTFKLIYS
recoverin  ......MGNSKSGALSKEILEELQLNTKFTEEELSAWYQSFLKECPSGRITRQEFESIYS
NCS 1      ......MGKS.NSKLKPEVVEELTRKTYFTEKEVQQWYKGFIKDCPSGQLDAAGFQKIYK

          120       130       140       150       160       170
DREAM      QFFPQGDATTYAHFLFNAFDADGNGAIHFEDFVVGLSILLRGTVHEKLKWAFNLYDINKD
recoverin  KFFPDSDPKAYAQHVFRSFDANSDGTLDFKEYVIALHMTTAGKPTQKLEWAFSLYDVDGN
NCS 1      QFFPFGDPTKFATFVFNVFDENKDGRIEFSEFIQALSVTSRGTLDEKLRWAFKLYDLDND

          180       190       200         210       220       230
DREAM      GCITKEEMLAIMKSIYDMMGRH..TYPILREDAPLEHVERFFQKMDRNQDGVVTIDEFLE
recoverin  GTISKNEVLEIVMAIFKMIKPEDVKLLPDDENTPEKRAEKIWAFFGKKEDDKLTEEEFIE
NCS 1      GYITRNEMLDIVDAIYQMVGNT..VELPEEENTPEKRVDRIFAMMDKNADGKLTLQEFQE

           240       250
DREAM      TCQKDENIMNSMQLFENVI.........
recoverin  GTLANKEILRLIQFEPQKVKERIKEKKQ
NCS 1      GSKADPSIVQALSLYDGLV.........
```

Figure 6.3: Sequence alignment among and DREAM, recoverin and NCS1 using UniPROT with identical residues highlighted in red and similar residues highlighted in yellow. The position of the α-helices corresponds to the DREAM structure (PDB entry 2JUL).

6.2 Results

6.2.1 Impact of Zn^{2+} in the tertiary structure of DREAM

The intrinsic fluorescence emission of the singe Trp 169 residue was monitored in order to determine the impact of the binding of Zn^{2+} in the tertiary structure of the protein . apoDREAMWT exhibits the emission spectrum with λ_{max} at 330 nm. Addition of Zn^{2+} leads to a quenching of the Trp emission and the emission intensity of apoDREAMWT and Mg^{2+} DREAMWT decreases by ~ 20 % , whereas the emission intensity of Ca^{2+}DREAM and Ca^{2+} Mg^{2+} DREAM by ~ 10% (Figure 6.4). These results indicate the Zn^{2+} binding to DREAM triggers changes in the Trp169 environment.

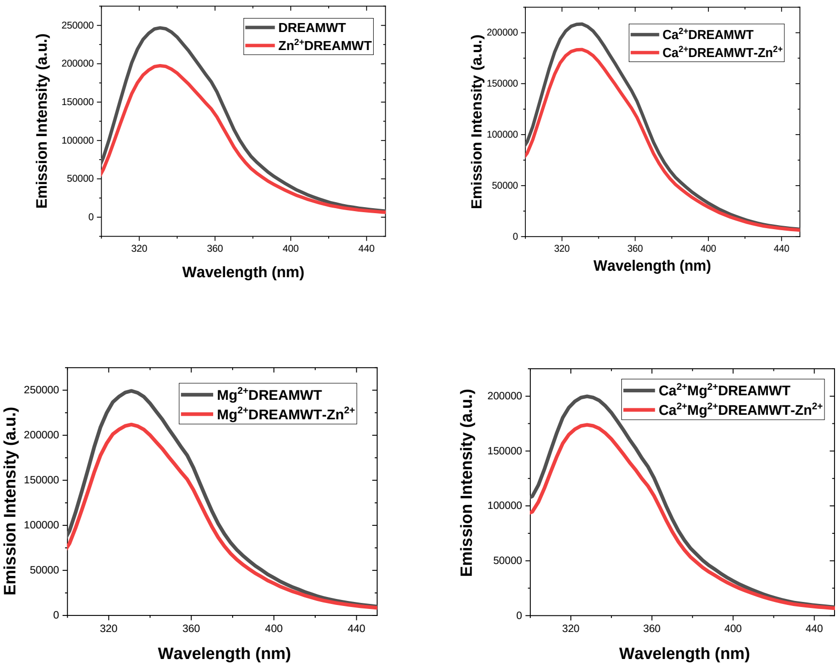

Figure 6.4: Trp169 emission intensity for Zn^{2+} addition (red traces) to apoDREAMWT (top left panel) , Ca^{2+}DREAMWT (top right panel) , Mg^{2+}DREAMWT(bottom left panel) and $Ca^{2+}Mg^{2+}$DREAMWT (bottom right panel). The emission spectra were recorded using λ_{exc} = 280 nm.

The change in the Trp emission can be used to determine the equilibrium constants for Zn^{2+} association to DREAM. The titration curves for Zn^{2+} binding to apoDREAM and Ca^{2+}DREAM are shown in Figure 6.5. The equilibrium dissociation constants were determined using a single site binding model (Equation 2.5) and are listed in Table 6.1 Dissociation constant for Zn^{2+} binding to the apoDREAMWT and Ca^{2+}DREAMWTwas determined to be 6.1 ± 0.9 μM and 12.6±1.02 μM, respectively, suggesting a slightly enhanced affinity of Zn^{2+} for DREAMWT in the absence of Ca^{2+}. The measured values are similar to the values reported for Zn^{2+} association to recoverin, $K_d = 7$ μM (Permyakov et al., 2003) and to NCS 1 $K_d = 4$ μM (Tsvetkov et al., 2018)

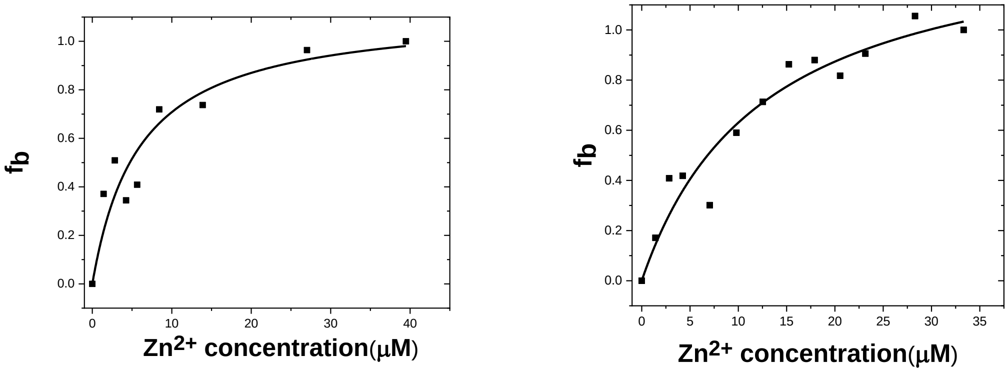

Figure 6.5: Titration curve for Zn^{2+} binding to apoDREAMWT (left) and Ca^{2+}DREAMWT. The solid line corresponds to the fit of the experimental data using Equation 2.5.

Table 6.1: Equilibrium dissociation constant for Zn^{2+} association to DREAMWT in the presence and absence of Ca^{2+}.

	K_d (μM)
DREAMWT	6.1 ± 0.9
Ca^{2+} DREAMWT	12.6±1.0

In addition, the binding of Zn^{2+} to the DREAM-C variant was investigated . DREAM-C is composed of amino acids located in the C terminal fragment of the protein 160 to 256, corresponding to EFH 3 and 4 , and α helix 10 including the (Figure 6.6) . The titration curves for the binding of Zn^{2+} to DREAM-C , Ca^{2+}DREAM-C, Mg^{2+}DREAM-C and Ca^{2+} Mg^{2+}DREAM-C are shown in Figure 6.7. The equilibrium dissociation constants are listed in Table 6.2 and were determined using a single site binding model (Equation 2.5) for Zn^{2+} binding to DREAM-C , Ca^{2+}DREAM-C and Mg^{2+}DREAM-C ; and the Hills equation (Equation 2.7) was used for Ca^{2+} Mg^{2+}DREAM-C.

The dissociation constant for Zn^{2+} binding to DREAM-C and Mg^{2+}DREAM-C were 12.59± 3.8 μM and 15.66±3.9 μM respectively , while the K_d for Ca^{2+}DREAM-C and Ca^{2+} Mg^{2+}DREAM-C were determined to be 5.92±0.9 μM and 7.58±0.7μM, respectively, suggesting a slightly enhanced affinity of Zn^{2+} for DREAM-C in the presence of Ca^{2+}.

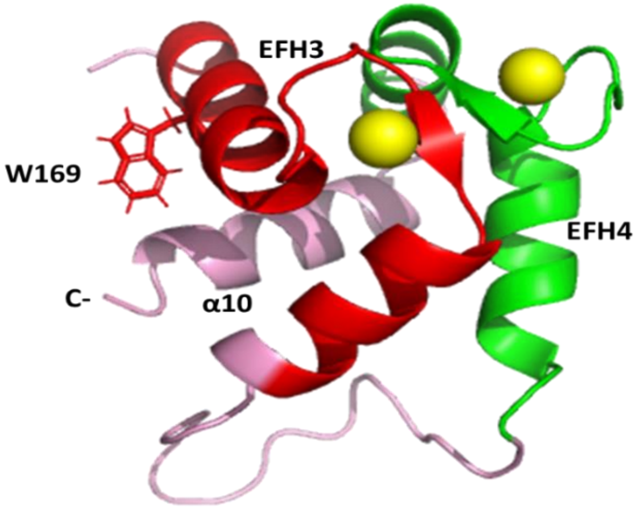

Figure 6.6: Structure of the Ca^{2+} bound DREAM-C (160 -256) (*PDB ID* 2E6W) . EFH 3 and 4 shown in red and green respectively,α10 shown in pink , Ca^{2+} ions shown as yellow spheres .

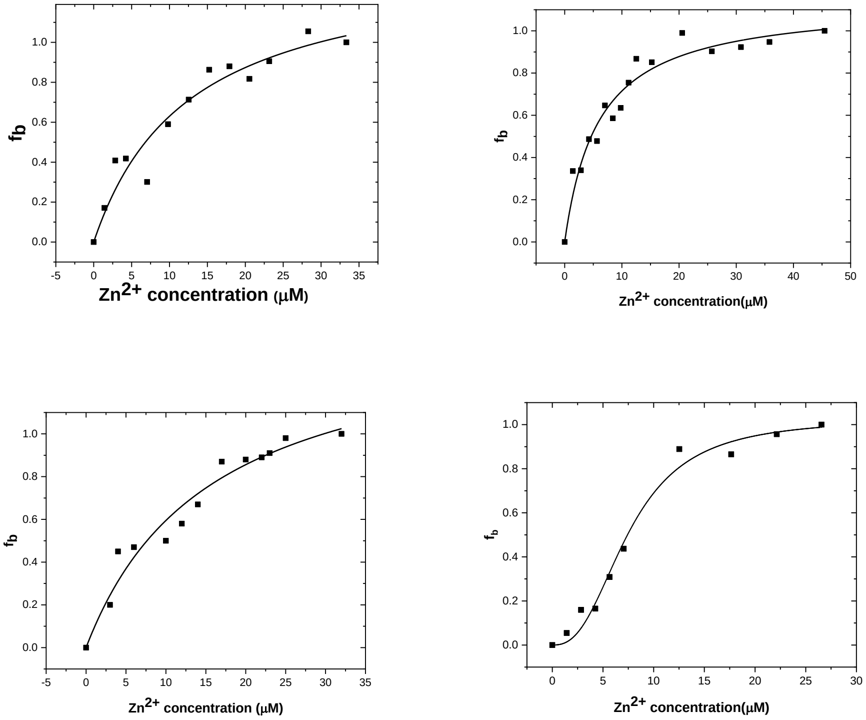

Figure 6.7: Titration curve for Zn^{2+} binding to DREAM-C (top left panel) and Ca^{2+}DREAM-C(top right panel) Mg^{2+}DREAM-C(bottom right panel) and $Ca^{2+}Mg^{2+}$ (bottom left panel) . The solid line corresponds to the fit of the experimental data using equation 5.7 for the titration in the presence of $Ca^{2+}Mg^{2+}$, and equation 2.5 for the rest of the titrations.

Table 6.2: Equilibrium dissociation constant for Zn^{2+} association to DREAM-C in the presence and absence of Ca^{2+} and Mg^{2+}.

	K_d (μM)	n
DREAM-C	12.59± 3.8	
Mg^{2+}DREAM-C	15.66±3.9	
Ca^{2+} DREAM-C	5.92±0.9	
$Ca^{2+}Mg^{2+}$DREAM-C	7.58±0.7	2.57±0.5

6.2.2 Impact of Zn^{2+} on DREAM interactions with the hydrophobic probe, 1,8-ANS

The impact of Zn^{2+} on DREAM interactions with the hydrophobic probe, 1,8-ANS was also monitored. It was shown previously, the 1,8-ANS hydrophobic probe binds to hydrophobic sides on DREAM surface and its affinity for DREAM in enhanced in the presence of $Ca^{2+.}$ Here I tested, if the association of Zn^{2+} promotes increases the exposure of hydrophobic patches on DREAM surface. The fluorescence emission of the 1,8-ANS:DREAMWT complex was measured in the presence and/or absence of Ca^{2+}, Mg^{2+} and/or Zn^{2+} . Upon Zn^{2+} addition to apoDREAMWT or Mg^{2+}poDREAMWT the emission of 1,8-ANS increases by roughly 30 % , whereas the Zn^{2+} addition to Ca^{2+} DREAM or $Ca^{2+}Mg^{2+}$DREAM resulted in an increase in the 1,8-ANS emission intensity of around 50% suggesting a greater impact of Zn^{2+} binding on accessibility of the hydrophobic cavities in the presence of Ca^{2+}.

Furthermore, the equilibrium dissociation constants for Zn^{2+} binding to 1,8 ANS:DREAMWT in the presence and absence of Ca^{2+} were determined by measuring the changes in 1,8 -ANS :DREAM complex emission intensity upon increasing concentration of Zn^{2+}. The K_d values were obtained by fitting the experimental data using Hill equation (Equation 2.7).Interestingly, Zn^{2+} association to 1,8-ANS:DREAMWT complex is cooperative with Hill coefficient of ~ 2 suggesting that the presence of the hydrophobic probe impact the mechanism of Zn^{2+} binding to its binding sites but the presence of the hydrophobic probe does not modulate the DREAM affinity for Zn^{2+} as the equilibrium dissociation constants determined in the absence and presence of 1,8-ANS are nearly identical (Table 6.2) .

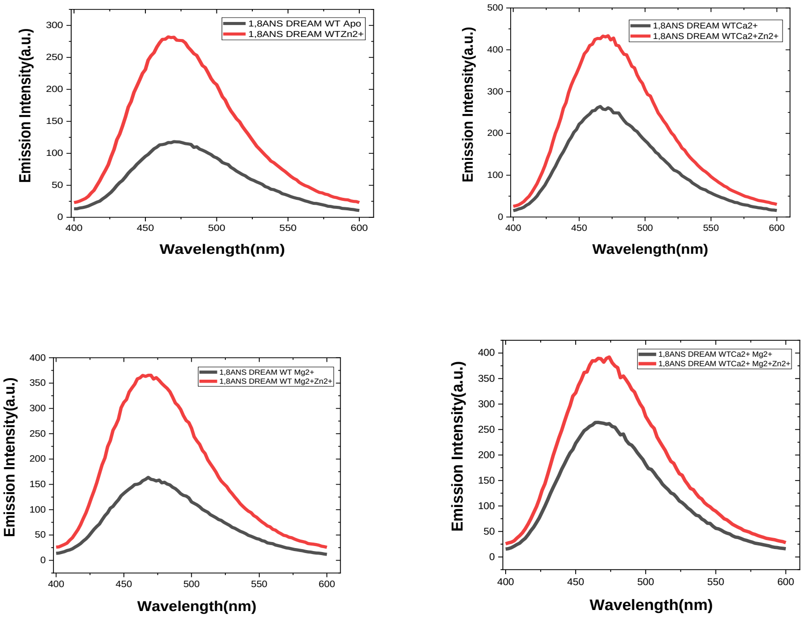

Figure 6.8: Emission spectra of 1,8-ANS:DREAMWT in the absence and/or presence of Zn^{2+} Ca^{2+} and/or Mg^{2+}.

However, analogously to the results determined in Trp 169 emission study, the affinity of 1,8-ANS:apoDREAM for Zn^{2+} is roughly two times stronger than affinity of 1,8-ANS:Ca^{2+}DREAM. (Table 6.2) suggesting a higher affinity apo DREAM for Zn^{2+} in the absence of $Ca^{2+.}$

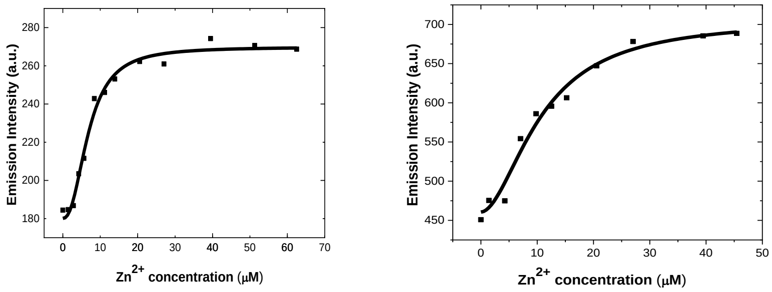

Figure 6.9: Titration curves for DREAMWT-1,8 ANS complex upon Zn^{2+} addition in the absence(left panel) and presence of Ca^{2+} (right panel).Fits shown as a line , traces were fit with Equation 2.7.

Table 6.2: Dissociation constant for 1,8 ANS - DREAMWT association with Zn^{2+} in the presence and absence of Ca^{2+}.

	K_d (μM)	n
Apo DREAMWT	6.9 ± 0.6	2.3 ± 0.4
Ca^{2+} DREAMWT	10.8 ± 1.5	1.8 ± 0.5

6.2.3 Impact of Zn^{2+} on the secondary structure of DREAM

The impact of the Zn^{2+} addition on the secondary structure of apo and Ca^{2+}DREAMWT were monitored by measuring the CD spectra of DREAM in the absence and presence of divalent metals. In the presence of Ca^{2+} and Mg^{2+} , the Zn^{2+} addition did not impact the secondary structure of DREAM as shown in Figure 6.8. However, for apoDREAMWT, a small decrease in the CD signal at 220 nm was observed upon Zn^{2+} addition , suggesting that the Zn^{2+} binding contributes to a stabilization of the secondary structure of the protein.

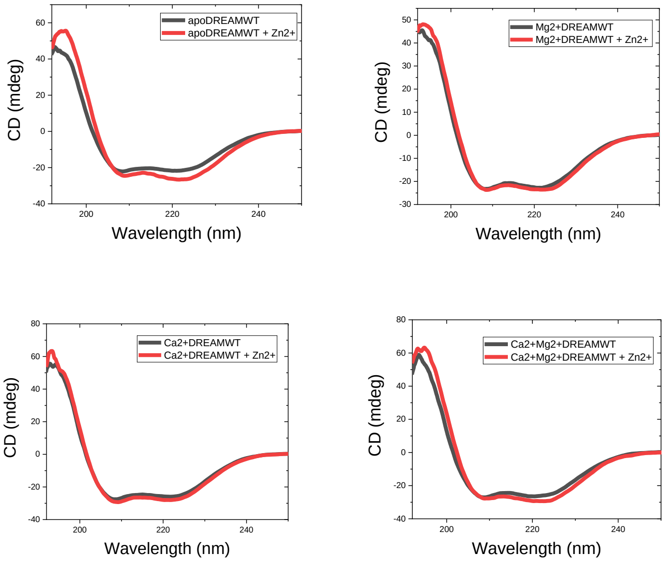

Figure 6.10: Far-UV CD spectra of DREAMWT in the presence or absence of divalent metals

6.2.4 Trp lifetimes measurements for DREAMWT in the presence of Zn^{2+}

Characterization of Trp lifetime in protein provide insight into dynamics of Trp environment as the Trp emission lifetime is sensitive to small changes in its environment. I have characterized Trp fluorescence lifetime to monitor the impact of Zn^{2+} binding on the interface between the N- and C- terminal domain where Trp169 sidechain is situate. The Trp emission decay measurements were carried out in the frequency domain and the plots of the phase shift and modulation ratio as a function of frequency of the excitation light are shown in Figure 6.11 as a for DREAMWT in the apo form and , Ca^{2+} and Zn^{2+} bound form. The emission decay data were analyzed using three exponential decay model and the recovered parameters are listed in Table 6.3 . All three constructs studied, apoDREAM, Ca^{2+}DREAM, Zn^{2+}DREAM exhibits trimodal emission decay characterized by $\tau_{1,}$ τ_2 and τ_3 lifetimes. The presence of the multiple lifetimes of a single Trp residue in proteins is relatively common and was associated with the presence of several conformers of Trp sidechain and/or conformational heterogeneity of protein structure. In the presence of Ca^{2+} the values τ_2 and τ_3 decrease with respect to apoDREAM, Addition of Zn^{2+}, leads to the further decrease in τ_1 and τ_3 values pointing towards more efficient Trp emission quenching factors in the presence of Zn^{2+}in agreement with steady state emission data. Furthermore , the anisotropy decay of the Trp residue for DREAMWT in the presence and absence of Ca^{2+} and Zn^{2+} were measured. The values obtained are listed in Table 6.3 , in the presence and absence of Ca^{2+} the time resolved anisotropy is 21.9± 3.0 and 10.5± 0.9 ns ,respectively . These values are in agreement with the previously calculated theoretical value for the monomeric form of the protein of 12ns (Gonzalez & Miksovska, 2014). In the presence of Zn^{2+} the time resolved anisotropy was 13.8± 2.0 ns, suggesting the Zn^{2+} bound to DREAM favours the monomer formation since this value is closer to the theoretical value previously obtained for the monomer.

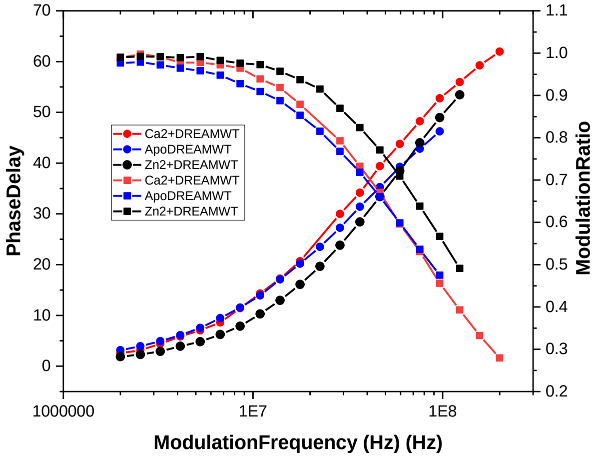

Figure 6.11: Frequency domain Trp intensity decay for apoDREAMWT(blue) and Ca^{2+}DREAMWT (red) and Zn^{2+}DREAMWT(black) . The closed circles represent the phase delay shift, and the closed squares represent the modulation ratio change. The emission decay data were fit to three exponentials decay.

Table 6.3: Fluorescence decay parameters for DREAMWT in the absence and presence of Ca^{2+} and Zn^{2+}. Values were obtained using a three exponential decay model.

	τ_1 (ns)	τ_2 (ns)	τ_3 (ns)	α_1	α_2	$\alpha 3$	f_1	f_2	f_3	$<\tau>$(ns)	χ^2
Ca^{2+}WT	0.565± 0.05	2.72± 0.2	6.6± 0.5	47	44	9	0.13± 0.01	0.539± 0.04	0.328± 0.05	3.70	2.67
apoWT	0.524± 0.03	3.51± 0.3	7.7± 1.0	70	28	2	0.21± 0.009	0.538± 0.07	0.189± 0.07	3.46	1.1
Zn^{2+}WT	0.422± 0.1	2.22± 0.2	5.03± 0.7	43	50	7	0.109± 0.02	0.666± 0.07	0.221± 0.08	2.64	2.81

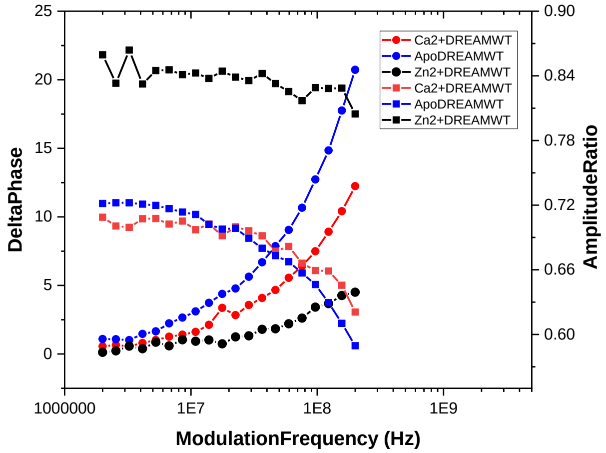

Figure 6.12: Time resolved anisotropy for apoDREAMWT(blue) and Ca^{2+}DREAMWT (red) and Zn^{2+}DREAMWT(black) . The closed circles represent the amplitude ratio , and the closed squares represent the delta phase shift.

Table 6.4: Time-resolved anisotropy decay values for DREAMWT and in the presence and absence of Ca^{2+} and Zn^{2+}

	Φ_1 (ns)	Φ_2 (ns)	r_1 (ns)	r_2(ns)	<τ>(ns)	χ^2
Ca^{2+}DREAMWT	0.114± 0.06	21.9± 3.0	0.546± 0.2	0.11± 0.003	3.78	0.287
ApoDREAMWT	0.156± 0.02	10.5± 0.9	0.961± 0.07	0.106± 0.004	3.46	2.85
Zn^{2+}DREAMWT	0.11	13.8± 2.0	0.2± 0.008	0.0537± 0.001	2.64	3.44

6.2.5 Site 1 , Site 2 and PSHL9 peptides interactions with DREAMWT in the presence of Zn^{2+}

As mentioned in the introduction, DREAM is a multi-functional intracellular protein that interacts with several targets including K_v channels, DNA and presenilin. To determine the impact on Zn^{2+} association to DREAM on its interactions with intracellular partner we have monitored Zn^{2+}DREAM binding to FITC labeled peptides that mimics DREAM binding sites in Kv channel and in presenilin. Namely DREAM binds to two sites in the T1 domain of Kv channels, site 1 that is composed by residues 2-22 (FITC-AAGVAAWLPFARAAAIGWMPV) and site 2 that is composed by residues 70-90 (FITC-LLGSTEKEFFFNEDTKEYFFD). In addition, the results from our group have shown previously, that helix 9 from presenilin (PS1HL9), residues 445--467 (FYFATDYLVQPFMDQLAFHQFYI) represent the binding interface for DREAM (Pham & Miksovska, 2016). Thus, by measuring the steady-state anisotropy of FITC labeled peptides as a function of increasing concentration of Zn^{2+}DREAM, we have determined the binding affinity for above mentioned peptides and are summarized on Table 6.2.

The individual titration curves are shown in Figure 6.13 for interactions of DREAM with site 1. Overall , the presence of Zn^{2+} increases the affinity of DREAM for site 1 with respect to apoDREAM approximately 10 to 14 times but the affinity of Zn^{2+}DREAM is comparable to that determined for Ca^{2+}DREAM. Interestingly, unlike Ca^{2+}DREAM, the interaction of Zn^{2+}DREAM with site 1 is cooperative, with the Hill coefficient value of 2.

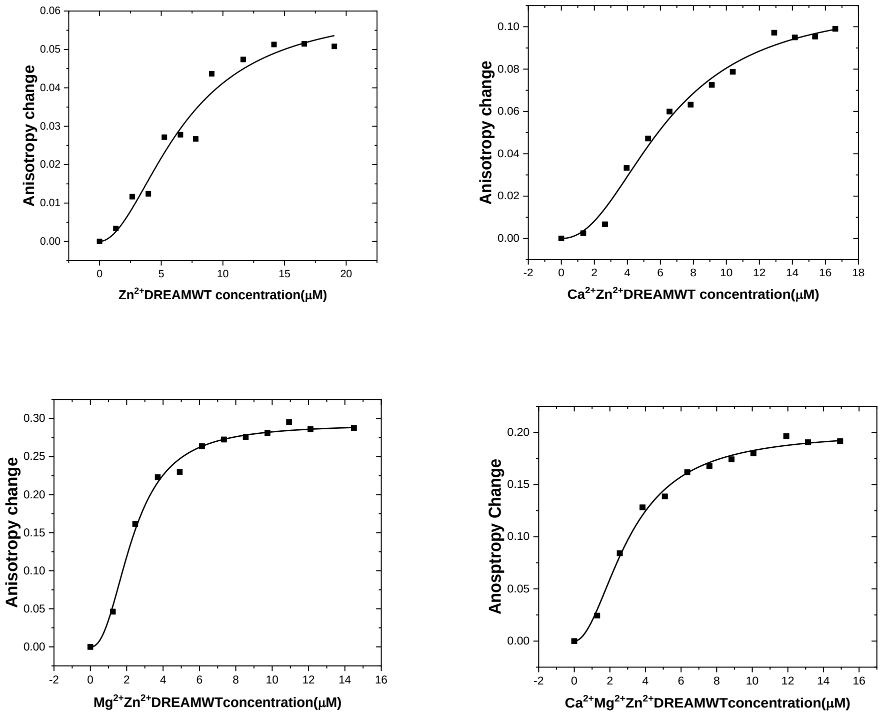

Figure 6.13 Titration of 0.5 μM Site1 Kv4.3(2–22) peptide with Zn^{2+}DREAMWT (top left panel) $Ca^{2+}Zn^{2+}$DREAMWT (top right panel), $Mg^{2+}Zn^{2+}$DREAMWT (bottom left panel) and $Ca^{2+}Mg^{2+}Zn^{2+}$ DREAMWT (bottom right panel). The solid curves correspond to the fit of the experimental data using Equation 2.7.

The titration curves for DREAM association to site 2 are presented in Figure 6.14. Association of Zn^{2+}DREAM and $Zn^{2+}Mg^{2+}$DREAM to site 2 is non-cooperative whereas the binding of $Ca^{2+}Zn^{2+}$DREAM and $Ca^{2+}Zn^{2+}Mg^{2+}$DREAM is cooperative with the Hill coefficient value of -2. The equilibrium dissociation constant for DREAM binding to site 2 in the presence of Zn^{2+} are comparable to those reported previously for Ca^{2+}DREAM and are significantly higher that the value reported for apoDREAM (Pham & Miksovska, 2016).

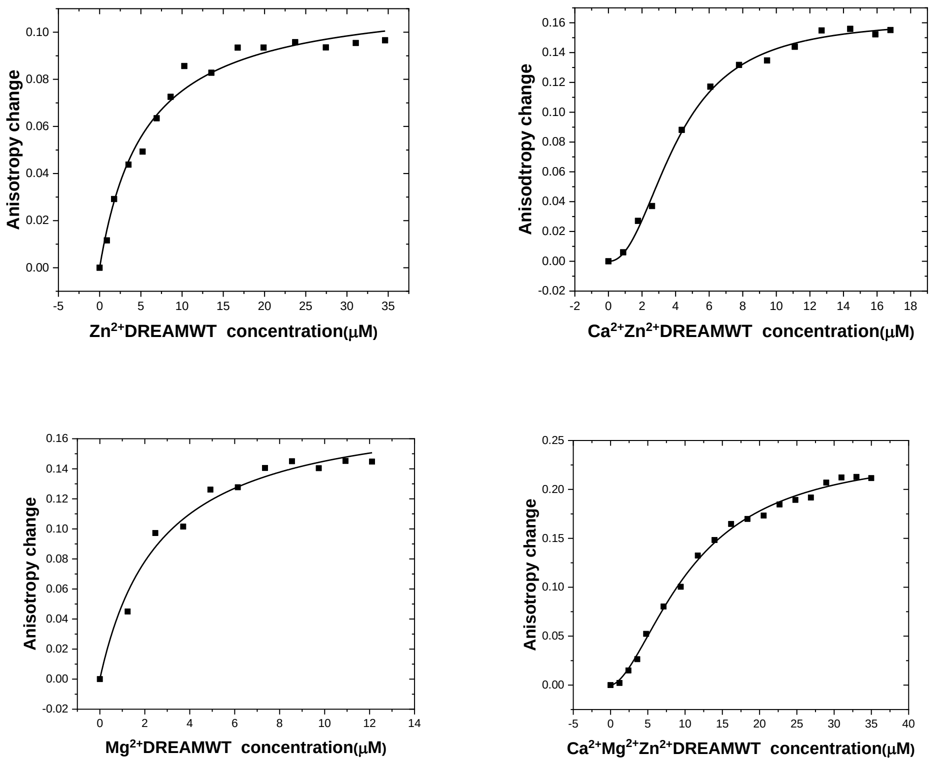

Figure 6.14 Titration of 0.5 μM Site2 Kv4.3(70–90) with Zn^{2+}DREAMWT(top left panel) $Ca^{2+}Zn^{2+}$DREAMWT(top right panel), $Mg^{2+}Zn^{2+}$DREAMWT(bottom left panel) and $Ca^{2+}Mg^{2+}Zn^{2+}$ DREAMWT (bottom right panel). Fits shown as a line, traces were fit with Equation 2.5 and 2.7.

Analogously, the Zn^{2+} DREAM binds to PS1HL9 with the equilibrium dissociation constant that is comparable to that for Ca^{2+} and the titration curves measured in the presence of Ca^{2+} and/or Mg^{2+} shows a cooperative-interactions(Figure 6.15).

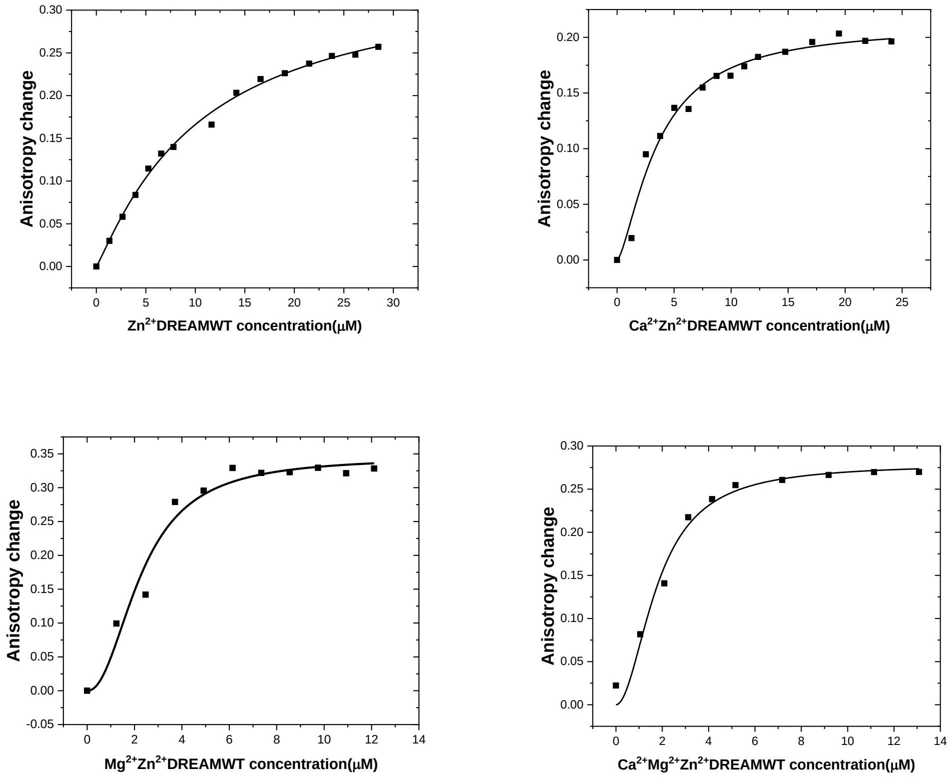

Figure 6.15 Titration of 0.5 μM PS1HL9 presenilin-1 helix 9 with Zn^{2+}DREAMWT(top left panel) $Ca^{2+}Zn^{2+}$DREAMWT(top right panel), $Mg^{2+}Zn^{2+}$DREAMWT(bottom left panel) and $Ca^{2+}Mg^{2+}Zn^{2+}$ DREAMWT (bottom right panel) . Fits shown as a line , traces were fit with Equation 2

Table 6.4 Equilibrium dissociation constants for Site-1 $K_{v4.3}$ (2-22) , Site-2 $K_{v4.3}$ (70-90) and PS1HL9 binding to DREAMWT in the presence/absence of divalent metals.

	Site 1		Site 2		HL9	
	Kd(μM)	n	Kd(μM)	n	Kd(μM)	n
apoDREAMWT*	70±3	NA	~500	NA	183±12	NA
Ca^{2+}DREAMWT*	2.7±0.1	NA	10±1	NA	0.6±0.1	NA

Zn^{2+}DREAMWT	6.83±1.3	1.91±0.5	5.5±0.6	NA	10.6±1.0	1.12±0.1
$Ca^{2+}Zn^{2+}$DREAMWT	6.4±0.5	2.17±0.3	4.11±0.2	2.21±0.2	3.62±0.3	1.47±0.02
$Mg^{2+}Zn^{2+}$DREAMWT	2.4±0.1	2.31±0.2	2.71±0.5		2.29±0.2	2.17±0.5
$Ca^{2+}Mg^{2+}Zn^{2+}$DREAMW	3.1±0.2	1.96±0.2	10.88±0.5	1.71±0.1	1.800.1	1.97±0.3

*Data for apoDREAMWT and Ca^{2+}DREAMWT were reported by Gonzalez et al (Gonzalez 2014)

6.2.6 Molecular dynamics simulation of Zn^{2+} association to DREAMWT

Ligand prediction web tool was utilized to determine potential Zn^{2+} binding to sites in DREAM. In addition, molecular dynamic (MD) simulations were performed for the DREAMWT binding to Zn^{2+} in the presence and absence of Ca^{2+}in order to gain a better understanding of the experimental results. The Metal Ion-Binding Site Prediction and Docking Server web page (MIB) (Lin et al., 2016) was employed for Zn^{2+} binding site detection. The MIB site uses the fragment transformation method, which consist of comparing the query protein to a metal ion residue template data base using a function that includes both structural and sequence conservation criteria and stablished a threshold score , ultimately it assigns a score for each amino acid predicting the ones above the threshold are possible metal binding sites.

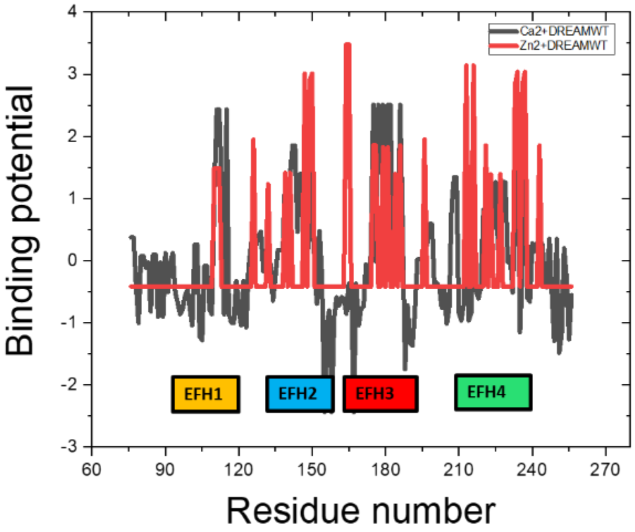

Figure 6.16: Plot of the predicted binding potential value for each residue in DREAM for the interactions with Ca^{2+} and $Zn^{2+.}$ Values were obtained from the MIB website (Lin et al., 2016).

The Metal Ion binding site predicted the Zn^{2+} to have the highest probability to bind to residues located within and in the vicinity of EFH 2, 3 and 4 . Namely in EFH2, Zn^{2+} is coordinated by oxygen atoms from Asp150 and His 147 with Asp 150 coordinating Mg^{2+} in Mg^{2+}DREAM. In EFH 4, Zn^{2+} binds to oxygen atoms from Glu 234 and Glu 237 sidechains, with Glu 234 sidechain coordinating Ca^{2+} in Ca^{2+}DREAM. Additional two binding sites are formed by Glu 165 and His 164 that are situated in the E-helix of EFH3 and by Glu 213 and Glu 216 that are located in the E-helix of EFH4. (Figure 6.17)

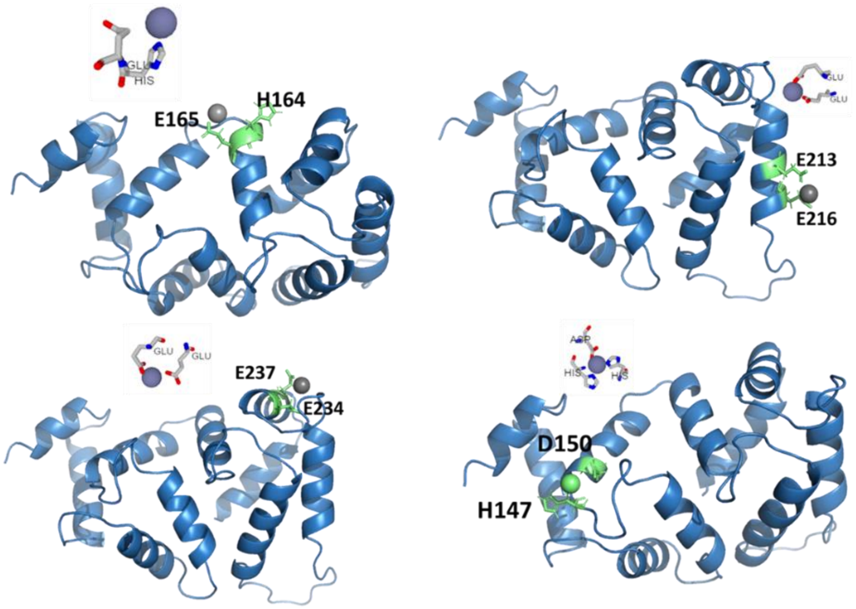

Figure 6.17: Top four docking positions of Zn2+ on DREAMWT identified using the web tool Metal Ion binding prediction server (Lin et al., 2016) .

We have also used cMD simulation to identify Zn^{2+} binding sites in apoDREAM and Ca^{2+}DREAM. for the Zn^{2+-}DREAMWT structure in the presence and absence of Ca^{2+} was performed to obtain more detailed information on the binding of Zn^{2+} to DREAM. To identify Zn2+ binding sited in the Ca^{2+}DREAM structure, 20 Zn atoms were randomly placed in the water box in the vicinity of the protein. In case of apoDREAM, Ca2+ ions were removed from the original structure and two Zn^{2+} ions were placed in the interface between the N- and C- terminal domain. The simulation of the structures of Zn^{2+}DREAM in the absence and presence of Ca^{2+} were carry out for 600 ns and 300 ns, respectively. Both structures reached a stable conformation at around 50 ns of simulation time as evidenced by the RMSD plot in Figure 6.15. Furthermore, the plot of RMSF for individual carbon alfa suggests that similar pattern of Cα fluctuations in Zn^{2+}DREAM and

Zn^{2+}Ca^{2+}DREAM (Figure 6.16). Interestingly, r when compared to the Ca^{2+} DREAM, the presence of Zn2+ is associated with a loss of dynamics for residues forming the loop situated between EFH1 and EFH2 and to lesser extent for the loop connecting EFH 2 and EFH3.

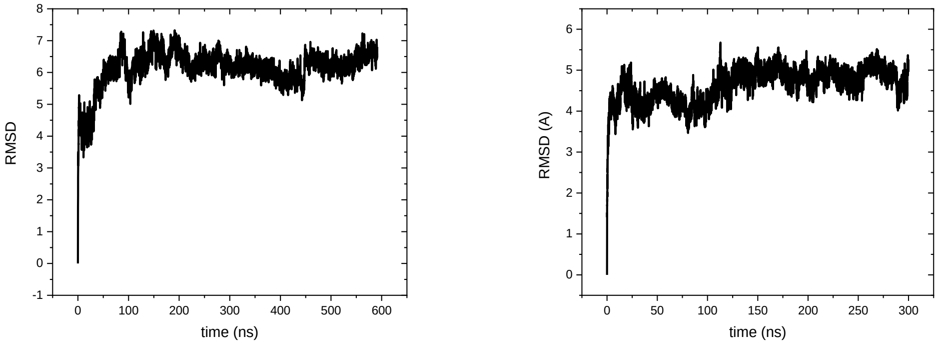

Figure 6.15: RMSD as a function of simulation time for Zn^{2+} DREAM in the absence (left panel) and presence (right panel) of Ca^{2+}.

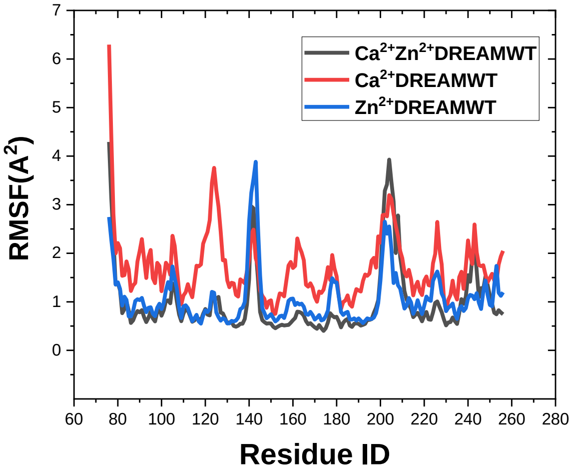

Figure 6.16: RMSF of the Cα for the performed Zn^{2+}DREAM simulations in the presence (black trace) and absence of Ca$^{2+(}$blue trace) , compared to Ca^{2+}DREAMWT(red trace) RMSF values.

.

The simulation of Zn^{2+} binding to apoDREAM and Ca^{2+}DREAM resulted in the identification of a single binding site located in the loop of EFH2. The residues located within Å from Zn^{2+} atom throughout the simulation were identified and are shown in Figure 6.21. The frequency at which they were in close contact with the Zn^{2+} atom was calculated in order to elucidate which residues are most likely to be involved in the binding of Zn^{2+} and the histograms for each residue in apoDREAM and Ca^{2+}DREAM structure are presented in Figure 6.19 and 6.20, respectively.

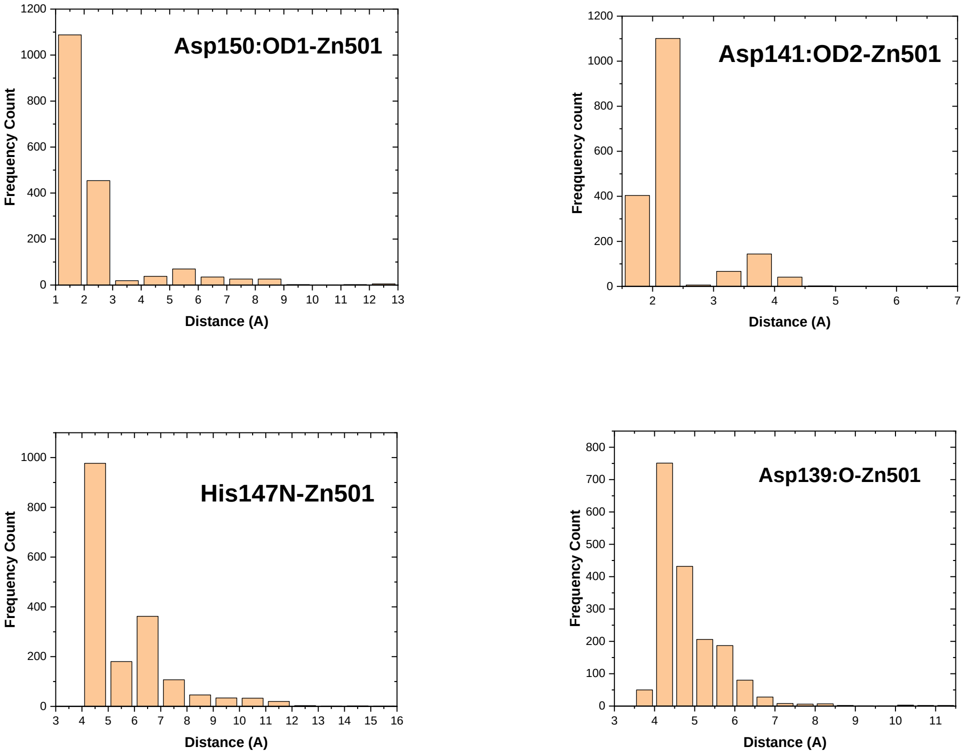

Figure 6.19: Frequency counts as function of distance for the Zn^{2+}DREAMWT simulation. The amino acids shown are likely to bind to Zn^{2+} atom number 501 and presented a high frequency of distance lower than 5Å .

Interestingly , different amino acids were identified for the Zn^{2+} bound to DREAM in the presence and absence of Ca^{2+}. For the Zn^{2+} simulation in the absence of Ca^{2+}, the identified amino acids that were most of the simulation within 5 Å of the Zn^{2+} atom are Asp150, Asn141 ,His147 and Asp139 (Figure 6.19). For the Zn^{2+} DREAM simulation in the presence of Ca^{2+}, the identified amino acids are His147, Asp141 and Asn143. (Figure 6.20)

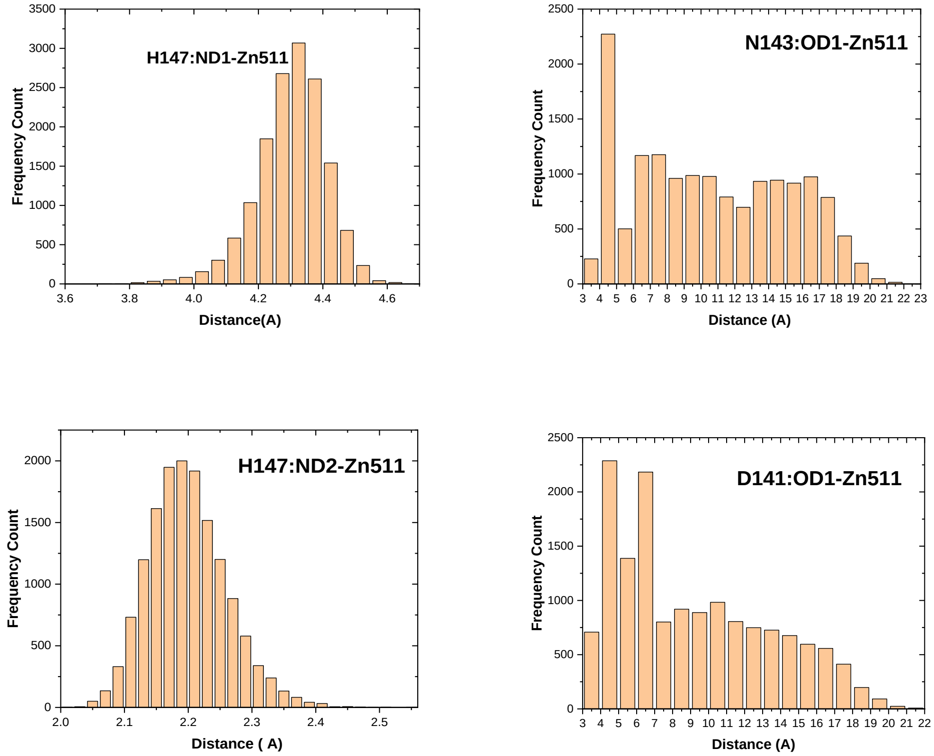

Figure 6.20 : Frequency counts as function of distance for the Zn^{2+}DREAMWT simulation in the presence of Ca^{2+} . The amino acids shown are likely to bind to Zn^{2+} and presented a high frequency of distance lower than 5Å

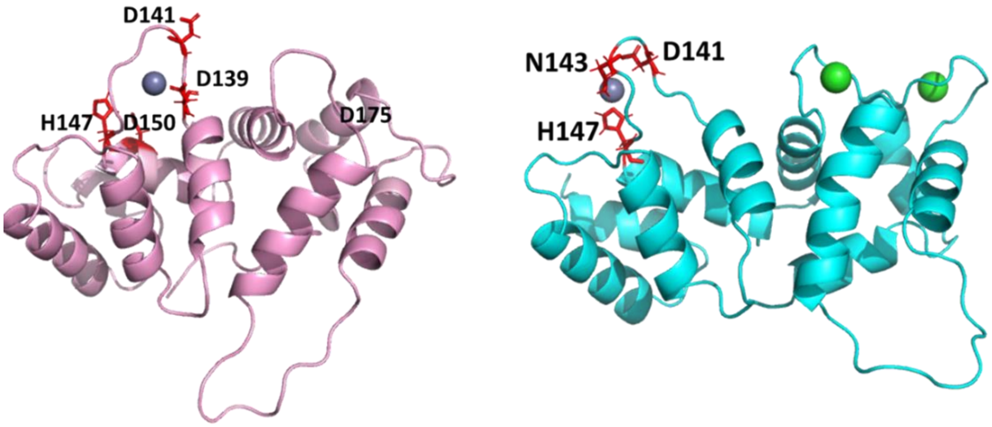

Figure 6.21: Structures taken from the final frames of the simulation of the binding of Zn^{2+} to DREAM in the absence (left panel) and presence (right panel) of $Ca^{2+.}$ Amino acids involved that remained in the vicinity of the Zn^{2+} throughout the simulation are shown as red sticks, Zn^{2+} ions are shown as grey spheres and Ca^{2+} ions are shown as green spheres.

In apoDREAM, Zn^{2+} is bound to the oxygen atoms from side chains of Asp 150 and Asp 141 whereas in the Ca^{2+}DREAM, nitrogen form His 147 and oxygen from Asp 141 seems to coordinate Zn^{2+} atom. The molecular dynamics simulations provided more insight into the process of Zn^{2+} binding to Ca^{2+} and suggest that Zn^{2+} is able to bind to DREAM in the presence and absence of Ca^{2+}.

As the Zn^{2+} association to DREAM results in increased Trp 169 quenching, we have examined the surrounding of Trp 169 in Zn^{2+}DREAM and compare it to its environment in apoDREAM and Ca^{2+}DREAM (Figure 6.17). In the structure of apoDREAM, Trp169 sidechain is oriented towards the C- terminal domain. In the presence of Ca^{2+}, Trp169 sidechain flips and its positing towards the hydrophobic residues in the C- terminal domain. Interestingly, in the structure of Zn^{2+}DREAM, Trp 169 sidechain is in the vicinity of Tyr 174 sidechain. We speculate that the excited state proton transfer between Tyr 174 sidechain and Trp 169 sidechain is responsible for the enhanced Trp 169 emission quenching in the presence of Zn^{2+}.

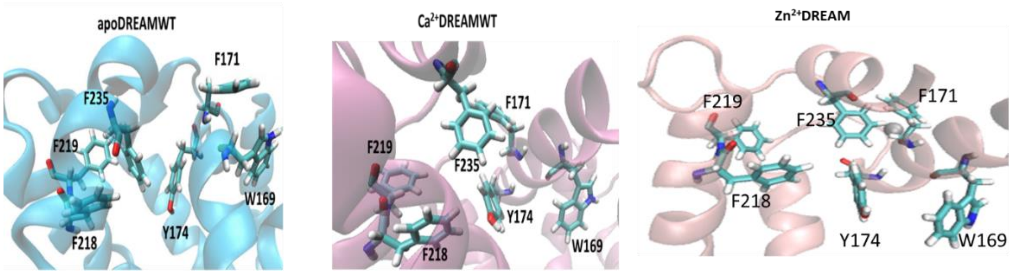

Figure 6.17 : Trp169 residue environment analysis for DREAM WT in the absence (left panel) and presence of Ca^{2+} and the resulting structure of Zn^{2+} bound to DREAMWT (right panel)

I have also investigated the impact of Zn^{2+} binding on the orientation of α-helices in the individual EF hands to determine if the binding of Zn^{2+}produced a structural rearrangement similar to the ones observed upon Ca^{2+} binding. The structures of EF hands from the initial structures were aligned with the EF hands from Zn^{2+} bound structures at the end of the simulation. For the Zn^{2+} bound to Ca^{2+} DREAM, the position of α-helices in EFH 2 and EFH 4was very similar to that observed in Ca^{2+}DREAM, and a shift in orientation of α-helices in the EFH 1 and EFH 3 was observed. More pronounced difference was observed when the structure of comparing the initial and final structures of Zn^{2+} binding to DREAM in absence of Ca^{2+}, in such case a significant shift is observed in the EFH4

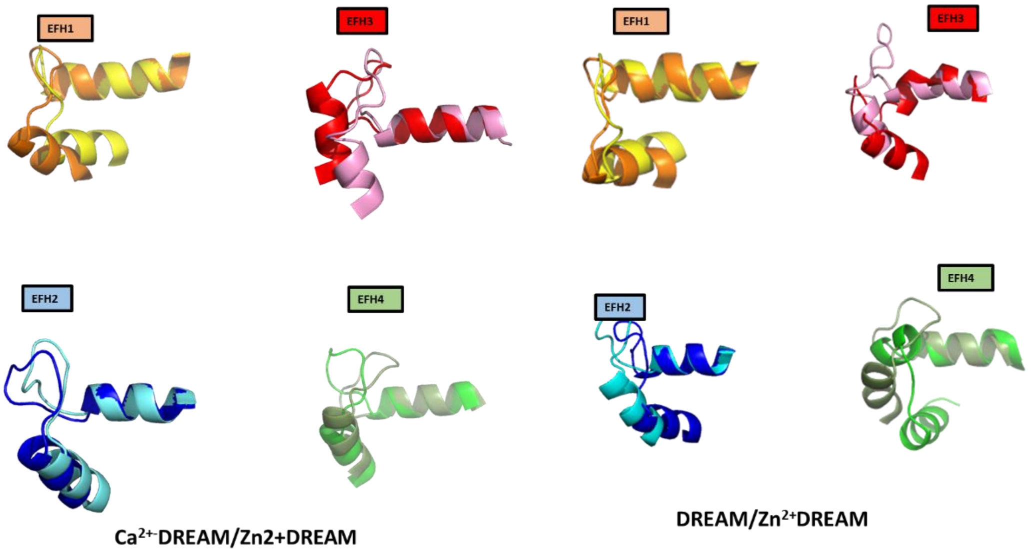

Figure 6.18: Individual alignment of each EF-hand of DREAM for the initial structure and final Zn^{2+} bound structures in the presence(left panel) and absence (right panel) of Ca^{2+}. Alignments were done using the first 12 amino acids of the entering helix, EFH1(orange-0 ns /yellow- 300 ns) , EFH2 (blue/cyanide) EFH3 (red/pink) EFH4 (green/olive)

6.2.6 Discussion

The results presented here are consistent with one or more Zn^{2+} atoms binding to DREAM in both the apo and Ca^{2+} bound form K_d values of 6.1 ±0.9 µM and 12.6 ±1.0 µM, respectively . These values are comparable to the K_d values determined for Zn^{2+} association other NCS members such as recoverin and NCS1 and are comparable to K_d value determined for Ca^{2+} binding to apoDREAM. Zn^{2+} association to DREAM leads to a quenching to the Trp emission and enhances the exposure of the hydrophobic patches in the protein was as evidenced by the increase in intensity of the 1,8 ANS-DREAM complex. These results indicate that Zn^{2+} binding promotes similar structural transition as observed before for Ca^{2+}. The cMD data points towards EFH2 to represent a binding site for Zn^{2+}. This is consistent with the Trp emission data and emission data of 1,8-ANS:DREAM complexes that show the increased Trp quenching and enhanced 1,8-ANS emission for Ca^{2+} DREAM, suggesting that the presence of Ca^{2+} does not prevent Zn^{2+} binding to the protein. However, the presence of a single binding sites in the EFH2 is not consistent with the comparable Zn^{2+}DREAM affinity for site 1, site 2 and PS1H9 peptide to that determined in the presence of Ca^{2+}. We speculate that in the absence of Ca^{2+}, Zn^{2+} atom binds to EFH4 or possibly EFH4 and EFH3, triggering structural changes that are analogous to those determined in the presence of Ca^{2+}. In case of Ca^{2+}DREAM, Zn^{2+} atom binds to EFH2, resulting to additional quenching of Trp 169 emission as shown in Figure 6.4.

We have attempted to identify Zn^{2+} binding site in cMD simulation. The identification of the Zn^{2+} binding site in EFH2 is in agreement with the experimental data. However, cMD simulation data did not indicate Zn^{2+} binding to EFH3 and/or EFH4. It is possible that longer simulation time or addition or higher number of Zn^{2+} atoms in the simulation box may increase the probability to find other Zn^{2+} binding sites on the protein surface.

7. CONCLUSIONS

The kinetics studies performed on the binding of Ca^{2+} to DREAM WT suggest that the binding of Ca^{2+} to the protein can be illustrated as a two-step process. The first step on a millisecond time scale is observed on both cases the DREAMWT and the DREAMNCS1, with τ values of 8ms and 13.25 ms, respectively. However, the second step observed on a longer time scale presented a decrease in signal only for the WT version of the protein .The results for the association of $Ca^{2+}$to DREAMNCS1 and DREAMWT in the presence of NaCl lead to a similar process for the slow kinetics since the decrease in intensity on the 10 s time scale was not observed. Furthermore, the time resolved anisotropy measurements indicated the presence of the monomeric form the ApoDREAMWT and the dimeric form for the Ca^{2+} bound protein based on the values 10.5± 0.9 ns and 21.9± 3 ns, respectively which are in agreement to the theoretically calculated values (Gonzalez & Miksovska, 2014) using Equation 4.5. The MD Simulation of the DREAMNCS1 dimer is in agreement with the experimental data observed since it shows the inability of the two monomers to form the dimer, but it does not show significant difference with the Ca^{2+}DREAMWT monomer supporting the proposed mechanism involving the two steps : the Ca^{2+} association to the monomer and formation of the dimer being stabilized by the Leu residues 155,158, 159 and 251 and the salt bridge comprised of Arg 200 and 207 and Glu 103. These results indicate that the first step corresponds to the association of Ca^{2+} to the monomeric form of the protein and the second step is associated to a conformational relaxation that leads to protein dimerization. Furthermore, the plot of k_{obs} vs ligand concentration for the Ca^{2+} association step, exhibited an inversed hyperbolic form which corresponds to the mechanism of conformational selection. Overall, determining the presence of the conformational selection mechanism is a crucial step to gaining more insight on how Ca^{2+} regulates the processes in which DREAM and other CBP are involved.

The Trp 169 residue was mutated to Ala in order to obtain more information on its role in the allosteric signal transmission between the N- and C- terminal in DREAM protein. Several molecular dynamic simulations were performed for the DREAMW169A mutant in the presence and absence of Ca^{2+}using different MD approaches. The loss of flexibility of the N- terminus in the presence of Ca^{2+} , as evidenced by the lower RMSF values for the loop connecting EFH1 and 2 for the mutated version when compared to the WT; and the previously identified important structure stabilizing salt bridge among Lys 87- Glu 165; along with the change in dynamics for the community networks analysis of the Ca^{2+}DREAW169A when compared to the Ca^{2+}DREAMWT; suggest the substitution of the Trp residue lead to more "apo like" structures and a disruption of the proposed signal transmission among the N- and C- terminals in DREAM . In addition, cMD studies the performed MD for the mutated DREAMW169A dimer showed a destabilization of the dimer as evidenced by its separation into monomers at 80 ns , a disruption of the previously identified salt bridges (Arg 200, Arg 207, and Glu 103) and the Leu motif interactions through a change in solvent accessible area, and a decrease in the dynamic communities among the two subunits. These results suggest the crucial role of the Trp 169A residue in the interdomain communication in DREAM protein

The interactions of Zn^{2+} binding to DREAM were studied and the data obtained suggests that Zn^{2+} binds to DREAM in both the apo and Ca^{2+} bound form, and that the association of Zn^{2+} triggers changes in the protein 's tertiary structure , as evidenced by the decrease in emission observed upon Zn^{2+} addition . The K_d for Zn^{2+} binding to DREAM in the apo and Ca^{2+} bound forms were determined to be 6.06 ±0.9 µM and 12.6 ±1 µM, respectively . These values are within the same range of the previously determined K_d for other NCS members such as recoverin and NCS1 . In addition, the exposure of the hydrophobic patches in the protein was also impacted by the addition of Zn^{2+} as evidenced by the increase in intensity of the 1,8 ANS-DREAM complex. The metal ion predictions and molecular dynamics simulation suggested that the binding of Zn^{2+} occurs around the EFH2 in the presence and absence of Ca^{2+}, which was also evidenced by the experimental data since changes in the Trp emission were observed in both cases. Zn^{2+} is usually coordinated by four ligands (Maret & Li, 2009; Maret, 2012), involving the side chain of Cys, His, Glu, or Asp . The identified residues to be involved in Zn^{2+} coordination are: Asp150, Asn141,His147 and Asp139 , for the Zn^{2+}DREAM binding , and His147, Asp141 and Asn143for the Zn^{2+} DREAM binding in the presence of Ca^{2+}. Residues His147 and Asp150 had previously been identified as high score residues for the binding Zn^{2+}. These results show that Zn^{2+} binds to DREAM with a relatively high affinity and possibly to other members of the NCS family in addition to recoverin and NCS1.

LIST OF REFERENCES

Ames, J. B., & Lim, S. (2012). Molecular structure and target recognition of neuronal calcium sensor proteins. *BBA - General Subjects, 1820*(8), 1205-1213. 10.1016/j.bbagen.2011.10.003

An, W. F., Bowlby, M. R., Betty, M., Cao, J., Ling, H., Mendoza, G., Hinson, J. W., Mattsson, K. I., Strassle, B. W., Trimmer, J. S., & Rhodes, K. J. (2000). Modulation of A-type potassium channels by a family of calcium sensors. *Nature (London), 403*(6769), 553-556. 10.1038/35000592

Azam, S., Bhattarai, N., Riveron, A., Rodriguez, S., Chapagain, P. P., & Miksovska, J. (2020a). EF-hands in Neuronal Calcium Sensor Downstream Regulatory Element Antagonist Modulator Demonstrate Submillimolar Affinity for Li+: A New Prospect for Li+ Therapy. *ACS Chemical Neuroscience, 11*(17), 2543-2548. 10.1021/acschemneuro.0c00399

Azam, S., Bhattarai, N., Riveron, A., Rodriguez, S., Chapagain, P. P., & Miksovska, J. (2020b). EF-hands in Neuronal Calcium Sensor Downstream Regulatory Element Antagonist Modulator Demonstrate Submillimolar Affinity for Li+: A New Prospect for Li+ Therapy. *ACS Chemical Neuroscience, 11*(17), 2543-2548. 10.1021/acschemneuro.0c00399

Azam, S., Louis, G. S., & Miksovska, J. (2019). Cadmium association with DREAM promotes DREAM interactions with intracellular partners in a similar manner to its physiological ligand, calcium. *Metallomics, 11*(6), 1115-1127. 10.1039/c9mt00059c

Azam, S., & Miksovska, J. (2019a). Pb2+ Binds to Downstream Regulatory Element Antagonist Modulator (DREAM) and Modulates Its Interactions with Binding Partners: A Link between Neuronal Calcium Sensors and Pb2+ Neurotoxicity. *ACS Chemical Neuroscience, 10*(3), 1263-1272. 10.1021/acschemneuro.8b00335

Azam, S., & Miksovska, J. (2019b). Pb2+ Binds to Downstream Regulatory Element Antagonist Modulator (DREAM) and Modulates Its Interactions with Binding Partners: A Link between Neuronal Calcium Sensors and Pb2+ Neurotoxicity. *ACS Chemical Neuroscience, 10*(3), 1263-1272. 10.1021/acschemneuro.8b00335

Bähring, R. (2018). Kv channel-interacting proteins as neuronal and non-neuronal calcium sensors. *Channels, 12*(1), 187-200. 10.1080/19336950.2018.1491243

Bandura, J., & Feng, Z. (2019). Current Understanding of the Role of Neuronal Calcium Sensor 1 in Neurological Disorders. *Molecular Neurobiology, 56*(9), 6080-6094. 10.1007/s12035-019-1497-2

Baudier, J., Haglid, K., Haiech, J., & Gérard, D. (1983). Zinc ion binding to human brain calcium binding proteins. Calmodulin and S100b protein. *Biochemical and Biophysical Research Communications, 114*(3), 1138-1146. 10.1016/0006-291X(83)90681-2

Braunewell, K., & Gundelfinger, E. D. (1999). Intracellular neuronal calcium sensor proteins: a family of EF-hand calcium-binding proteins in search of a function. *Cell & Tissue Research, 295*(1), 1-12. 10.1007/s004410051207

Brüschweiler, S., Konrat, R., & Tollinger, M. (2013). Allosteric Communication in the KIX Domain Proceeds through Dynamic Repacking of the Hydrophobic Core. *ACS Chemical Biology, 8*(7), 1600-1610. 10.1021/cb4002188

Burgoyne, R. D., & Weiss, J. L. (2001). The neuronal calcium sensor family of Ca2+-binding proteins (vol 353, pg 1, 2001). *Biochemical Journal, 354*, 727. 10.1042/0264-6021:3540727v

Burgoyne, R. D., & Haynes, L. P. (2012). Understanding the physiological roles of the neuronal calcium sensor proteins. *Molecular Brain, 5*(1), 2. 10.1186/1756-6606-5-2

Carrión, A. M., Link, W. A., Ledo, F., Mellström, B., & Naranjo, J. R. (1999). DREAM is a Ca2+-regulated transcriptional repressor. *Nature, 398*(6722), 80-84. 10.1038/18044

Changeux, J., & Edelstein, S. (2011). Conformational selection or induced-fit? 50 years of debate resolved. *F1000 Biology Reports, 3*, 19. 10.3410/B3-19

Cheng, H. M., & Penninger, J. M. (2004). DREAMing about arthritic pain. *Annals of the Rheumatic Diseases, 63*(suppl 2), ii72-ii75. 10.1136/ard.2004.029942

Choi, E. K., Miller, J. S., Zaidi, N. F., Salih, E., Buxbaum, J. D., & Wasco, W. (2003). Phosphorylation of calsenilin at Ser63 regulates its cleavage by caspase-3. *Molecular and Cellular Neurosciences, 23*(3), 495-506. 10.1016/S1044-7431(03)00072-1

Clarke, D., Sethi, A., Li, S., Kumar, S., Chang, R. F., Chen, J., & Gerstein, M. (2016). Identifying Allosteric Hotspots with Dynamics: Application to Inter- and Intra-species Conservation. *Structure (London), 24*(5), 826-837. 10.1016/j.str.2016.03.008

Craig, T. A., Benson, L. M., Venyaminov, S. Y., Klimtchuk, E. S., Bajzer, Z., Prendergast, F. G., Naylor, S., & Kumar, R. (2002). The metal-binding properties of DREAM: evidence for calcium-mediated changes in DREAM structure. *The Journal of Biological Chemistry, 277*(13), 10955-10966. 10.1074/jbc.M109660200

Cui, Q., & Karplus, M. (2008). Allostery and cooperativity revisited. *Protein Science, 17*(8), 1295-1307. 10.1110/ps.03259908

D. Burgoyne, R. (2004). The neuronal calcium-sensor proteins. *Biochimica Et Biophysica Acta (BBA) - Molecular Cell Research, 1742*(1), 59-68. https://doi.org/10.1016/j.bbamcr.2004.08.008

Dason, J., Romero-Pozuelo, J., Atwood, H., & Ferrús, A. (2012). Multiple Roles for Frequenin/NCS-1 in Synaptic Function and Development. *Molecular Neurobiology, 45*(2), 388-402. 10.1007/s12035-012-8250-4

del Sol, A., Tsai, C., Ma, B., & Nussinov, R. (2009). The Origin of Allosteric Functional Modulation: Multiple Pre-existing Pathways. *Structure (London), 17*(8), 1042-1050. 10.1016/j.str.2009.06.008

Deshpande, J., Joshi, M., & Giri, P. (2013). Zinc: The trace element of major importance in human nutrition and health. *International Journal of Medical Science and Public Health, 2*(1), 1. 10.5455/ijmsph.2013.2.1-6

Fagerberg, L., Hallström, B. M., Oksvold, P., Kampf, C., Djureinovic, D., Odeberg, J., Habuka, M., Tahmasebpoor, S., Danielsson, A., Edlund, K., Asplund, A., Sjöstedt, E., Lundberg, E., Szigyarto, C. A., Skogs, M., Takanen, J. O., Berling, H., Tegel, H., Mulder, J., . . . Uhlén, M. (2014). Analysis of the Human Tissue-specific Expression by Genome-wide Integration of Transcriptomics and Antibody-based Proteomics. *Molecular & Cellular Proteomics, 13*(2), 397-406. 10.1074/mcp.M113.035600

Findeisen, F., Hura, G. L., Minor, D. L., & Pioletti, M. (2006). Three-dimensional structure of the KChIP1-Kv4.3 T1 complex reveals a cross-shaped octamer. *Nature Structural & Molecular Biology, 13*(11), 987-995. 10.1038/nsmb1164

Galletto, R., Jezewska, M. J., & Bujalowski, W. (2005). Kinetics of allosteric conformational transition of a macromolecule prior to ligand binding: analysis of stopped-flow kinetic experiments. *Cell Biochemistry and Biophysics, 42*(2), 121-144. 10.1385/CBB:42:2:121

Gifford, J. L., Walsh, M. P., & Vogel, H. J. (2007). Structures and metal-ion-binding properties of the Ca2+-binding helix–loop–helix EF-hand motifs. *The Biochemical Journal, 405*(2), 199-221. 10.1042/BJ20070255

Glykos, N. M. (2006). Software news and updates carma: A molecular dynamics analysis program. *Journal of Computational Chemistry, 27*(14), 1765-1768. 10.1002/jcc.20482

Gonzalez, W. G. (2014). *Protein-Ligand Interactions and Allosteric Regulation of Activity in DREAM Protein* http://digitalcommons.fiu.edu/etd/2503

Gonzalez, W. G., & Miksovska, J. (2014). Application of ANS fluorescent probes to identify hydrophobic sites on the surface of DREAM. *BBA - Proteins and Proteomics, 1844*(9), 1472-1480. 10.1016/j.bbapap.2014.05.004

Gonzalez, W. G., Pham, K., & Miksovska, J. (2014). Modulation of the Voltage-gated Potassium Channel (Kv4.3) and the Auxiliary Protein (KChIP3) Interactions by the Current Activator NS5806. *The Journal of Biological Chemistry, 289*(46), 32201-32213. 10.1074/jbc.M114.577528

Greener, J. G., & Sternberg, M. J. (2018). Structure-based prediction of protein allostery. *Current Opinion in Structural Biology, 50*, 1-8. 10.1016/j.sbi.2017.10.002

Greenfield, N. J. (2007). Using circular dichroism spectra to estimate protein secondary structure. *Nature Protocols, 1*(6), 2876-2890. 10.1038/nprot.2006.202

Groenendyk, J., Agellon, L. B., & Michalak, M. (2021). Calcium signaling and endoplasmic reticulum stress. *International Review of Cell and Molecular Biology, 363*, 1-20. 10.1016/bs.ircmb.2021.03.003

Hooper, P. L. (1980). Zinc lowers high-density lipoprotein-cholesterol levels. *JAMA : The Journal of the American Medical Association, 244*(17), 1960-1961. 10.1001/jama.244.17.1960

Humphrey, W., Dalke, A., & Schulten, K. (1996). VMD: Visual molecular dynamics. *Journal of Molecular Graphics, 14*(1), 33-38. 10.1016/0263-7855(96)00018-5

Inoue, K., Branigan, D., & Xiong, Z. (2010). Zinc-induced Neurotoxicity Mediated by Transient Receptor Potential Melastatin 7 Channels. *The Journal of Biological Chemistry, 285*(10), 7430-7439. 10.1074/jbc.M109.040485

Jameson, D. M. (2014). *Introduction to Fluorescence*. CRC Press. 10.1201/b16502

Jo, S., Kim, T., Iyer, V. G., & Im, W. (2008). CHARMM-GUI: A web-based graphical user interface for CHARMM. *Journal of Computational Chemistry, 29*(11), 1859-1865. 10.1002/jcc.20945

Kido, T., Suka, M., & Yanagisawa, H. (2022). Effectiveness of interleukin-4 administration or zinc supplementation in improving zinc deficiency–associated thymic atrophy and fatty degeneration and in normalizing T cell maturation process. *Immunology, 165*(4), 445-459. 10.1111/imm.13452

Korson, L., Drost-Hansen, W., & Millero, F. J. (1969). Viscosity of water at various temperatures. *Journal of Physical Chemistry (1952), 73*(1), 34-39. 10.1021/j100721a006

Laity, J. H., Lee, B. M., & Wright, P. E. (2001). *Zinc finger proteins: new insights into structural and functional diversity*. Elsevier Ltd. 10.1016/S0959-440X(00)00167-6

Lakowicz, J. R. (2006). *Principles of Fluorescence Spectroscopy*. Springer. 10.1007/978-0-387-46312-4

Lewit-Bentley, A., & Réty, S. (2000). EF-hand calcium-binding proteins. *Current Opinion in Structural Biology, 10*(6), 637-643. https://doi.org/10.1016/S0959-440X(00)00142-1

Lilliehook, C., Buxbaum, J. D., Wasco, W., Merriam, D. E., Luo, Y., Crowley, A. C., & Choi, E. (1998). Calsenilin: A calcium-binding protein that interacts with the presenilins and regulates the levels of a presenilin fragment. *Nature Medicine, 4*(10), 1177-1181. 10.1038/2673

Lin, Y., Cheng, C., Shih, C., Hwang, J., Yu, C., & Lu, C. (2016). MIB: Metal Ion-Binding Site Prediction and Docking Server. *Journal of Chemical Information and Modeling, 56*(12), 2287-2291. 10.1021/acs.jcim.6b00407

Lock, J. T., Smith, I. F., & Parker, I. (2019). Spatial-temporal patterning of Ca2+ signals by the subcellular distribution of IP3 and IP3 receptors. *Seminars in Cell and Developmental Biology, 94*, 3-10. 10.1016/j.semcdb.2019.01.012

López-Hurtado, A., Burgos, D. F., González, P., Dopazo, X. M., González, V., Rábano, A., Mellström, B., & Naranjo, J. R. (2018). Inhibition of DREAM-ATF6 interaction delays onset of cognition deficit in a mouse model of Huntington’s disease. *Molecular Brain, 11*(1), 1-8. 10.1186/s13041-018-0359-6

Lusin, J. D., Vanarotti, M., Li, C., Valiveti, A., & Ames, J. B. (2008). NMR Structure of DREAM: Implications for Ca2+-Dependent DNA Binding and Protein Dimerization. *Biochemistry, 47*(8), 2252-2264. 10.1021/bi7017267

Maret, W. (2012). New perspectives of zinc coordination environments in proteins. *Journal of Inorganic Biochemistry, 111*, 110-116. 10.1016/j.jinorgbio.2011.11.018

Maret, W., & Li, Y. (2009). Coordination Dynamics of Zinc in Proteins. *Chemical Reviews, 109*(10), 4682-4707. 10.1021/cr800556u

Marino, V., & Dell'Orco, D. (2019). Evolutionary-Conserved Allosteric Properties of Three Neuronal Calcium Sensor Proteins. *Frontiers in Molecular Neuroscience, 12*, 50. 10.3389/fnmol.2019.00050

Masada, N., Schaks, S., Jackson, S. E., Sinz, A., & Cooper, D. M. F. (2012). Distinct Mechanisms of Calmodulin Binding and Regulation of Adenylyl Cyclases 1 and 8. *Biochemistry, 51*(40), 7917-7929. 10.1021/bi300646y

Masanori Osawa, Alexandra Dace, Kit I. Tong, Aswani Valiveti, Mitsuhiko Ikura, & James B. Ames. (2005). Mg2+ and Ca2+ Differentially Regulate DNA Binding and Dimerization of DREAM. *Journal of Biological Chemistry, 280*(18), 18008-18014. 10.1074/jbc.M500338200

Masanori Osawa, Kit I. Tong, Christina Lilliehook, Wilma Wasco, Joseph D. Buxbaum, H.-Y. Mary Cheng, Josef M. Penninger, Mitsuhiko Ikura, & James B. Ames. (2001). Calcium-regulated DNA Binding and Oligomerization of the Neuronal Calcium-sensing Protein, Calsenilin/DREAM/KChIP3. *Journal of Biological Chemistry, 276*(44), 41005-41013. 10.1074/jbc.M105842200

Miao, Y., Feher, V. A., & McCammon, J. A. (2015a). Gaussian Accelerated Molecular Dynamics: Unconstrained Enhanced Sampling and Free Energy Calculation. *Journal of Chemical Theory and Computation, 11*(8), 3584-3595. 10.1021/acs.jctc.5b00436

Miao, Y., Feher, V. A., & McCammon, J. A. (2015b). Gaussian Accelerated Molecular Dynamics: Unconstrained Enhanced Sampling and Free Energy Calculation. *Journal of Chemical Theory and Computation, 11*(8), 3584-3595. 10.1021/acs.jctc.5b00436

Milo, R., & Phillips, R. (2015). *Cell Biology by the Numbers*. CRC Press LLC.

Naranjo, R., González, P., Lopez-Hurtado, A., Dopazo, X. M., Mellström, B., & Naranjo, J. R. (2018). Inhibition of the Neuronal Calcium Sensor DREAM Modulates Presenilin-2 Endoproteolysis. *Frontiers in Molecular Neuroscience, 11*, 449. 10.3389/fnmol.2018.00449

Ooi, L., & Wood, I. C. (2008). Regulation of gene expression in the nervous system. *The Biochemical Journal, 414*(3), 327-341. 10.1042/BJ20080963

Padamsey, Z., Foster, W. J., & Emptage, N. J. (2019). Intracellular Ca 2+ Release and Synaptic Plasticity: A Tale of Many Stores. *The Neuroscientist (Baltimore, Md.), 25*(3), 208. https://www.ncbi.nlm.nih.gov/pubmed/30014771

Page, M. J., & Di Cera, E. (2008). Serine peptidases: Classification, structure and function. *Cellular and Molecular Life Sciences : CMLS, 65*(7-8), 1220-1236. 10.1007/s00018-008-7565-9

Permyakov, E. A., & Kretsinger, R. H. (2011). *Calcium Binding Proteins* (1st ed.). John Wiley & Sons.

Permyakov, S. E., Cherskaya, A. M., Wasserman, L. A., Khokhlova, T. I., Senin, I. I., Zargarov, A. A., Zinchenko, D. V., Zernii, E. Y., Lipkin, V. M., Philippov, P. P., Uversky, V. N., & Permyakov, E. A. (2003). Recoverin Is a Zinc-Binding Protein. *Journal of Proteome Research, 2*(1), 51-57. 10.1021/pr025553i

Pham, K., & Miksovska, J. (2016). Molecular insight of DREAM and presenilin 1 C-terminal fragment interactions. *FEBS Letters, 590*(8), 1114-1122. 10.1002/1873-3468.12156

Philippov, P., & Koch, K. (2007). *Neuronal Calcium sensor proteins* . Nova Science. 10.1038/nrn2093

Phillips, J. C., Braun, R., Wang, W., Gumbart, J., Tajkhorshid, E., Villa, E., Chipot, C., Skeel, R. D., Kalé, L., & Schulten, K. (2005). Scalable molecular dynamics with NAMD. *Journal of Computational Chemistry, 26*(16), 1781-1802. 10.1002/jcc.20289

Phillips, J. C., Hardy, D. J., Maia, J. D. C., Stone, J. E., Ribeiro, J. V., Bernardi, R. C., Buch, R., Fiorin, G., Hénin, J., Jiang, W., McGreevy, R., Melo, M. C. R., Radak, B. K., Skeel, R. D., Singharoy, A., Wang, Y., Roux, B., Aksimentiev, A., Luthey-Schulten, Z., . . . Tajkhorshid, E. (2020). Scalable molecular dynamics on CPU and GPU architectures with NAMD. *The Journal of Chemical Physics, 153*(4), 44130-044130. 10.1063/5.0014475

Ping Liang, Huayi Wang, Hao Chen, Yuanyuan Cui, Lichuan Gu, Jijie Chai, & KeWei Wang. (2009). Structural Insights into KChIP4a Modulation of Kv4.3 Inactivation. *Journal of Biological Chemistry, 284*(8), 4960-4967. 10.1074/jbc.M807704200

Plum, L. M., Rink, L., & Haase, H. (2010). The Essential Toxin: Impact of Zinc on Human Health. *International Journal of Environmental Research and Public Health, 7*(4), 1342-1365. 10.3390/ijerph7041342

Pozzi, N., Vogt, A. D., Gohara, D. W., & Di Cera, E. (2012). Conformational selection in trypsin-like proteases. *Current Opinion in Structural Biology, 22*(4), 421-431. 10.1016/j.sbi.2012.05.006

Pruunsild, P., & Timmusk, T. (2005). Structure, alternative splicing, and expression of the human and mouse KCNIP gene family. *Genomics (San Diego, Calif.), 86*(5), 581-593. 10.1016/j.ygeno.2005.07.001

Ramirez, D., Gonzalez, W., Fissore, R. A., & Carvacho, I. (2017). Conotoxins as Tools to Understand the Physiological Function of Voltage-Gated Calcium (Ca-V) Channels. *Marine Drugs, 15*(10), 313. 10.3390/md15100313

Schaub, M. C., & Heizmann, C. W. (2008). Calcium, troponin, calmodulin, S100 proteins: From myocardial basics to new therapeutic strategies. *Biochemical and Biophysical Research Communications, 369*(1), 247-264. 10.1016/j.bbrc.2007.10.082

She, M., Dong, W. J., Umeda, P. K., & Cheung, H. C. (1997). Time-resolved fluorescence study of the single tryptophans of engineered skeletal muscle troponin C. *Biophysical Journal, 73*(2), 1042-1055. 10.1016/S0006-3495(97)78137-2

Sibarov, D. A., & Antonov, S. M. (2018). Calcium-Dependent Desensitization of NMDA Receptors. *Biochemistry (Moscow), 83*(10), 1173-1183. 10.1134/S0006297918100036

Srivastava, S. S., Mishra, A., Krishnan, B., & Sharma, Y. (2014). Ca2+-binding Motif of βγ-Crystallins*. *Journal of Biological Chemistry, 289*(16), 10958-10966. https://doi.org/10.1074/jbc.O113.539569

Stryer, L. (1965). The interaction of a naphthalene dye with apomyoglobin and apohemoglobin. A fluorescent probe of non-polar binding sites. *Journal of Molecular Biology, 13*(2), 482. 10.1016/S0022-2836(65)80111-5

Sukumaran, P., Nascimento Da Conceicao, V., Sun, Y., Ahamad, N., Saraiva, L. R., Selvaraj, S., & Singh, B. B. (2021). Calcium Signaling Regulates Autophagy and Apoptosis. *Cells (Basel, Switzerland), 10*(8), 2125. 10.3390/cells10082125

Tang, S., & Yang, J. J.Magnesium Binding Sites in Proteins. *Encyclopedia of Metalloproteins* (pp. 1243-1250). Springer New York. 10.1007/978-1-4614-1533-6_257

Trace elements in human nutrition and health (1996).

Tsvetkov, P. O., Roman, A. Y., Baksheeva, V. E., Nazipova, A. A., Shevelyova, M. P., Vladimirov, V. I., Buyanova, M. F., Zinchenko, D. V., Zamyatnin, A. A., Devred, F., Golovin, A. V., Permyakov, S. E., & Zernii, E. Y. (2018). *Functional Status of Neuronal Calcium Sensor-1 Is Modulated by Zinc Binding*. Frontiers Media SA. 10.3389/fnmol.2018.00459

Vallee, B. L., & Falchuk, K. H. (1993). The biochemical basis of zinc physiology. *Physiological Reviews, 73*(1), 79-118. 10.1152/physrev.1993.73.1.79

Vogt, A. D., & Di Cera, E. (2012). Conformational Selection or Induced Fit? A Critical Appraisal of the Kinetic Mechanism. *Biochemistry (Easton), 51*(30), 5894-5902. 10.1021/bi3006913

Wang, W., Agellon, L. B., & Michalak, M. (2019). Organellar Calcium Handling in the Cellular Reticular Network. *Cold Spring Harbor Perspectives in Biology, 11*(12), a038265. 10.1101/cshperspect.a038265

Warren, J. T., Guo, Q., & Tang, W. (2007). A 1.3Å Structure of Zinc-bound N-terminal Domain of Calmodulin Elucidates Potential Early Ion-binding Step. *Journal of Molecular Biology, 374*(2), 517-527. 10.1016/j.jmb.2007.09.048

Wei, Y., Thyparambil, A. A., & Latour, R. A. (2014). Protein Helical Structure Determination Using CD Spectroscopy for Solutions with Strong Background

Absorbance from 190-230 nm. *Biochimica Et Biophysica Acta, 1844*(12), 2331-2337. 10.1016/j.bbapap.2014.10.001

Yan, Y., Hao, Q., Wang, K., Shen, Y., Wang, H., Huang, Y., Chai, J., Chen, Y., Yang, Q., Liu, Q., & Chen, L. (2007). Structural basis for modulation of Kv4 K + channels by auxiliary KChIP subunits. *Nature Neuroscience, 10*(1), 32-39. 10.1038/nn1822

Yu, L., Sun, C., Mendoza, R., Wang, J., Matayoshi, E. D., Hebert, E., Pereda-Lopez, A., Hajduk, P. J., & Olejniczak, E. T. (2007). Solution structure and calcium-binding properties of EF-hands 3 and 4 of calsenilin. *Protein Science, 16*(11), 2502-2509. 10.1110/ps.072928007

Zhang, J., Li, J., Craig, T. A., Kumar, R., & Gross, M. L. (2017). Hydrogen–Deuterium Exchange Mass Spectrometry Reveals Calcium Binding Properties and Allosteric Regulation of Downstream Regulatory Element Antagonist Modulator (DREAM). *Biochemistry, 56*(28), 3523-3530. 10.1021/acs.biochem.7b00100

VITA

MARIA D. SANTIAGO ESTEVEZ

2012-2014	B.S., Chemistry Florida International University Miami, Florida
2017-2019	M.S., Chemistry Florida International University Miami, Florida NSF Bridge to the Doctorate Fellow
2019-2022	PhD., Chemistry Florida International University Miami, Florida McKnight Fellow

PUBLICATIONS AND PRESENTATIONS

Neuronal Calcium Sensor Dream Interactions with Insulinotropic Agent Repaglinide Santiago, Maria D. et al. Biophysical Journal, Volume 116, Issue 3, 471a

The Molecular Mechanism of Ca^{2+} Triggered DREAM Dimerization Santiago, Maria D. et al. Biophysical Journal, Volume 118, Issue 3, 356a

Role of the Trp169 Residue in Neuronal Calcium Sensor Dream. Santiago, Maria D et al. Biophysical Journal, Volume 120, Issue 3, 296a

SoFLACS Sciences Symposium. February 26th, 2017.*Interaction of neuronal calcium sensor DREAM with Zinc*.

CURFIU. March29th, 2017.*Interaction of neuronal calcium sensor DREAM with Zinc*

FAME. May 4th -6th, 2017. *Interaction of neuronal calcium sensor DREAM with Zinc*

Biophysical Society 62nd annual meeting. February 17th -21st, 2018. *Interactions of Neuronal Calcium Sensor DREAM with Zinc*

94th FAME. May 3rd-5th, 2018. *Role of F235A residue in neuronal calcium sensor DREAM.*

LSAMP PI/PD and BD Meeting. February 19th -21st, 2019. *Neuronal Calcium Sensor DREAM interactions with insulinotropic agent Repaglinide*

Biophysical Society 63rd annual meeting. March 2nd -6th, 2019. *Neuronal Calcium Sensor DREAM interactions with insulinotropic agent Repaglinide*

ACS National Meeting and Exposition. March 31st -April 4th, 2019. *Neuronal Calcium Sensor DREAM interactions with insulinotropic agent Repaglinide*

Annual BSI Research Symposium. April 12th, 2019. *Neuronal Calcium Sensor DREAM interactions with insulinotropic agent Repaglinide*

SoFLACS Chemical Sciences Symposium. April 12th -13th, 2019. *Neuronal Calcium Sensor DREAM interactions with insulinotropic agent Repaglinide*

FAME. May 9th -11th, 2019.*Characterization of the* Ca^{2+} *triggered oligomerization states in DREAM protein*

Biophysical Society 64th annual meeting. February 15th -19th, 2020. *The molecular mechanism of* Ca^{2+} *triggered DREAM dimerization.*

Annual BSI Research Symposium. July 30th, 2020. *Role of Trp169 in the interdomain communication in DREAM.*

Biophysical Society 65th virtual annual meeting, February 22nd – 26th, 2021. *Role of the TRP169 residue in neuronal calcium sensor DREAM.*

Annual BSI Research Symposium. April 30th ,2021 *Neuronal calcium sensor DREAM interactions with* Zn^{2+}

Biophysical Society 66th annual meeting. February 19th -23rd. *Mechanism of dream oligomerization kinetic study*.

Emerging Researchers National (ERN) Conference in STEM. February 22-24, 2018. *Interactions of Neuronal Calcium Sensor DREAM with Zinc*.